

WL-TR-96-4113



MATERIALS DEVELOPMENT RESEARCH

Madan G. Mendiratta, Ph.D.
Tai-Il Mah, Ph.D.
P. R. Subramanian, Ph.D.
Bhaskar Majumdar, Ph.D.
Christopher Woodward, Ph.D.

Peter M. Hazzledine, Ph.D.
Young-Won Kim, Ph.D.
S. Krishnamurthy, Ph.D.
T. A. Parthasarathy, Ph.D.

UES, Inc.
4401 Dayton-Xenia Road
Dayton, OH 45432-1894

November 1996

Final Report: 28 March 1992 to 30 September 1996

Approved for public release; distribution unlimited.

DTIC QUALITY INSPECTED 8

MATERIALS DIRECTORATE
WRIGHT LABORATORY
AIR FORCE MATERIEL COMMAND
WRIGHT-PATTERSON AFB, OH 45433-7734

19970717 198

NOTICE


WHEN GOVERNMENT DRAWINGS, SPECIFICATIONS, OR OTHER DATA ARE USED FOR ANY PURPOSE OTHER THAN IN CONNECTION WITH A DEFINITELY GOVERNMENT-RELATED PROCUREMENT, THE UNITED STATES GOVERNMENT INCURS NO RESPONSIBILITY OR ANY OBLIGATION WHATSOEVER. THE FACT THAT THE GOVERNMENT MAY HAVE FORMULATED OR IN ANY WAY SUPPLIED THE SAID DRAWINGS, SPECIFICATIONS, OR OTHER DATA, IS NOT TO BE REGARDED BY IMPLICATION OR OTHERWISE IN ANY MANNER CONSTRUED, AS LICENSING THE HOLDER OR ANY OTHER PERSON OR CORPORATION, OR AS CONVEYING ANY RIGHTS OR PERMISSION TO MANUFACTURE, USE, OR SELL ANY PATENTED INVENTION THAT MAY IN ANY WAY BE RELATED THERETO.

THIS REPORT IS RELEASABLE TO THE NATIONAL TECHNICAL INFORMATION SERVICE (NTIS). AT NTIS, IT WILL BE AVAILABLE TO THE GENERAL PUBLIC, INCLUDING FOREIGN NATIONS.

THIS TECHNICAL REPORT HAS BEEN REVIEWED AND IS APPROVED FOR PUBLICATION.



WAYNE S. MYERS, Project Engineer
Metals Development & Materials
Processing Branch
Metals, Ceramics & NDE Division



KATHERINE A. STEVENS, Actg Chief
Metals Development & Materials
Processing Branch
Metals, Ceramics & NDE Division



WALTER M. GRIFFITH, Asst. Chief
Metals, Ceramics & NDE Division
Materials Directorate

IF YOUR ADDRESS HAS CHANGED, IF YOU WISH TO BE REMOVED FROM OUR MAILING LIST, OR IF THE ADDRESSEE IS NO LONGER EMPLOYED BY YOUR ORGANIZATION, PLEASE NOTIFY, WL/MLLM, WRIGHT-PATTERSON AFB OH 45433-7817 TO HELP US MAINTAIN A CURRENT MAILING LIST.

COPIES OF THIS REPORT SHOULD NOT BE RETURNED UNLESS RETURN IS REQUIRED BY SECURITY CONSIDERATIONS, CONTRACTUAL OBLIGATIONS, OR NOTICE ON A SPECIFIC DOCUMENT.

REPORT DOCUMENTATION PAGE			Form Approved OMB No. 0704-0188	
Public reporting burden for this collection of information is estimated to average 1 hour per response, including the time for reviewing instructions, searching existing data sources, gathering and maintaining the data needed, and completing and reviewing the collection of information. Send comments regarding this burden estimate or any other aspect of this collection of information, including suggestions for reducing this burden, to Washington Headquarters Services, Directorate for Information Operations and Reports, 1215 Jefferson Davis Highway, Suite 1204, Arlington, VA 22202-4302, and to the Office of Management and Budget, Paperwork Reduction Project (0704-0188), Washington, DC 20503.				
1. AGENCY USE ONLY (Leave blank)	2. REPORT DATE November 1996	3. REPORT TYPE AND DATES COVERED Final Report, 28 March 1992 - 30 September 1996		
4. TITLE AND SUBTITLE Materials Development Research		5. FUNDING NUMBERS C - F33615-91-C-5663 PE - 62102F PR - 2306 TA - P8 WU - 03		
6. AUTHOR(S) Madan G. Mendiratta, Tai-Il Mah, P. R. Subramanian, Bhaskar Majumdar, Christopher Woodward, Peter M. Hazzledine, S. Krishnamurthy, T. A. Parthasarathy, Young-Won Kim				
7. PERFORMING ORGANIZATION NAME(S) AND ADDRESS(ES) UES, Inc. 4401 Dayton-Xenia Road Dayton, OH 45432		8. PERFORMING ORGANIZATION REPORT NUMBER		
9. SPONSORING/MONITORING AGENCY NAME(S) AND ADDRESS(ES) Materials Directorate Wright Laboratory Air Force Materiel Command Wright-Patterson AFB, OH 45433-7734; POC: John Farraro, WL/MLLM (937)255-1370		10. SPONSORING/MONITORING AGENCY REPORT NUMBER WL-TR-96-4113		
11. SUPPLEMENTARY NOTES				
12a. DISTRIBUTION AVAILABILITY STATEMENT Approved for public release: distribution is unlimited		12b. DISTRIBUTION CODE A		
13. ABSTRACT (Maximum 200 words) Research has been carried out in three materials areas: Advanced Metallics two systems -- Gamma-TiAl alloys and NbTi/silicide composites are being developed as high temperature structural materials. The research includes chemistry/processing/microstructure/property relations to provide a specific balance of mechanical properties. A physical vapor deposition system has been built to produce nanolayered and nanocrystalline materials. Quantitative models have been developed to describe the yield strength of gamma-TiAl alloys, metallic multi-layers and nanocrystalline Al alloys. Theoretical work has been carried out, using a variety of analytical and computational tools, to predict fundamental aspects of plasticity and fracture on length scales connected to electronic, atomistic and continuum levels. Advanced Metallic Composites research has involved SiC fiber/Ti matrix composites with focus on interface and matrix chemistry/microstructures to provide optimum mechanical properties. The interfaces were studied by testing composites containing only a few fibers while the matrix development involved chemistry and heat treatment optimization. Ceramic Matrix Composites work included studies on experimental mechanics, fiber coatings and oxide-oxide composites. Models were developed to study the effect of matrix roughness on fiber push-out/pull-out. Various fiber/matrix interface control concepts to weaken interfaces by oxidation resistant means were explored. Fugitive interface concept was successfully demonstrated on oxide-oxide composites.				
14. SUBJECT TERMS Refractory Metals, Niobium Silicide Intermetallics, Physical Vapor Deposition, Metallic Multi-Layers, Nanocrystalline Aluminum Alloys, Core Structure and Mobility of Dislocations, Planar Fault Energies, Green's Function, Point Defects, Gamma TiAl Alloys, Titanium Matrix Composites, Oxide-Oxide Composites, Interface Coatings			15. NUMBER OF PAGES 170	
			16. PRICE CODE	
17. SECURITY CLASSIFICATION OF REPORT Unclassified	18. SECURITY CLASSIFICATION OF THIS PAGE Unclassified	19. SECURITY CLASSIFICATION OF ABSTRACT Unclassified	20. LIMITATION OF ABSTRACT SAR	

TABLE OF CONTENTS

<u>SECTION</u>	<u>PAGE</u>
1.0 INTRODUCTION	1
2.0 TASK I. ADVANCED METALLICS	2
2.1 ADVANCED INTERMETALLICS	2
2.1.1 SUMMARY OF MAJOR FINDINGS	5
2.1.1.1 Model Nb/Nb ₅ Si ₃ Composites	5
2.1.1.2 Synthesis and Fracture Resistance Behavior of Nb/Nb ₅ Si ₃ Powder Metallurgy Composites	5
2.1.1.3 Unconstrained and Constrained Tensile Flow and Fracture Behavior of an Nb-1.24% Si Alloy	8
2.1.1.4 Evaluation of Cr ₂ Nb/(Cr) and Cr ₂ Nb/(Nb) Composites as High Temperature Structural Materials	9
2.1.1.5 Creep of Nb-Si Alloys	10
2.1.1.6 Mo-Cr-Si Beta + 3:1 Silicide Alloys	17
2.1.1.7 Nb-Ti-Hf(Cr)-Al-Si Alloys	19
2.2 NANOLAYERED MATERIALS	22
2.2.1 SUMMARY OF MAJOR FINDINGS	22
2.2.1.1 Fabrication of Vapor Deposition System	22
2.2.1.2 Film Deposition	23

DTIC QUALITY INSPECTED 8

TABLE OF CONTENTS (Continued)

<u>SECTION</u>	<u>PAGE</u>
2.3	TiAl TECHNOLOGY DEVELOPMENT 25
2.3.1	SUMMARY OF MAJOR FINDINGS 25
2.3.1.1	Phase Relations and Microstructural Evolution 25
2.3.1.2	Microstructure-Property Relationships 28
2.4	DESIGNING MICROSTRUCTURES 43
2.4.1	SUMMARY OF MAJOR FINDINGS 43
2.4.1.1	Microstructure Optimization 43
2.4.1.2	Process Development 44
2.4.1.3	Microstructure Design 45
2.4.1.4	TMTL Microstructures 46
2.4.1.5	RFL Microstructures 47
2.4.1.6	TMPL Microstructures 49
2.5	THEORETICAL STUDIES AND COMPUTATIONAL MATERIALS SCIENCE 52
2.5.1	SUMMARY OF MAJOR FINDINGS 52
2.5.1.1	Dependence of Strength on the Scale of the Microstructure 52
2.5.1.2	Influence of Alloy Chemistry on Yield Stress 57
2.5.1.3	Core Structure of Mobility of $a\langle 101 \rangle$ Super Dislocations in $L1_0$ TiAl 58
2.5.1.4	Simulations of $1/2\langle 110 \rangle$ Dislocation in γ -TiAl 59
2.5.1.5	Nanostructured Layers 59
2.5.1.6	Coherent (111)TiAl:TiAl Interfaces 62

TABLE OF CONTENTS (Continued)

<u>SECTION</u>	<u>PAGE</u>
2.5.1.7 Interaction of $a/2\langle 110 \rangle$ Ordinary Dislocations with γ - γ Interfaces	62
2.5.1.8 Green's Function Flexible Boundary Conditions	63
2.6 SUMMARY OF CURRENT WORK NOT REPORTED	64
2.6.1 COHERENCE STRESSES IN MULTI-LAYERS	67
2.6.2 HALL-PETCH STRENGTHENING AND STROH THEORY FOR TWINNING	68
2.6.3 YIELD STRESS OF FULLY-LAMELLAR TiAl	69
2.6.4 STABILITY OF NANOCRYSTALLINE GRAIN STRUCTURES	70
2.6.5 DIRECT VERSUS INDIRECT HARDENING OF NANOCRYSTALLINE MATERIALS	70
2.6.6 COBLE CREEP IN NANOCRYSTALLINE MATERIALS	71
2.6.7 CROSS SLIP OF $a/2[110]$ SCREW DISLOCATIONS IN FCC Ni	73
2.6.8 SOLID SOLUTION EFFECTS IN B2 NiAl	73
2.6.9 PREDICTING POINT DEFECT PROPERTIES AND POINT DEFECT-DISLOCATION INTERACTIONS IN INTERMETALLIC ALLOYS	75
2.6.10 POINT DEFECT PROPERTIES IN INTER-METALLIC ALLOYS	75

TABLE OF CONTENTS (Continued)

<u>SECTION</u>	<u>PAGE</u>
2.6.11 FIRST PRINCIPLES DETERMINATION OF CRITICAL PARAMETERS FOR MATERIALS PROPERTIES	77
2.6.12 DEVELOPMENT OF A PHASE TRANSFORMATIONS INITIATIVE	82
2.7 PUBLICATIONS	83
2.8 PRESENTATIONS	92
2.9 INVENTION DISCLOSURES/PATENTS	98
2.10 BOOKS	99
2.11 EDIT CONFERENCE PROCEEDINGS	99
2.12 AWARDS	99
2.13 REFERENCES	100

TABLE OF CONTENTS (Continued)

<u>SECTION</u>	<u>PAGE</u>
3.0 TASK II. METAL MATRIX COMPOSITES	101
3.1 SUMMARY OF MAJOR FINDINGS	103
3.1.1 INTERFACE BEHAVIOR AND EFFECTS ON MMC RESPONSE	103
3.1.1.1 The Push-Out Test	104
3.1.1.2 The Single-Fiber Fragmentation Test	105
3.1.1.3 The Slice Compression Test	106
3.1.1.4 Damage Assessment in MMCs Using Ultrasonic NDE	107
3.1.1.5 Normal Strength Characterization of the Interface	107
3.1.1.6 Failure Mechanisms During Transverse Loading and Development of the Torsion Test for Tangential Shear Strength Determination	108
3.1.1.7 Interface Effects on Load Sharing Behavior Under Longitudinal Tension	109
3.1.1.8 Interface Effects on Fatigue Crack Growth	111
3.1.1.9 Interface Development for the Sapphire/Gamma- TiAl System Using Ductile and Barrier Metallic Layers	113
3.1.2 ORTHORHOMBIC TITANIUM ALUMINIDE MATRIX BEHAVIOR AND DEVELOPMENT	114
3.1.2.1 Effect of Matrix Texture on MMC Processing and Mechanical Properties	115

TABLE OF CONTENTS (Continued)

<u>SECTION</u>		<u>PAGE</u>
	3.1.2.2 Optimization of Ti-22Al-23Nb Matrix using Heat Treatments	116
	3.1.2.3 Role of Carbon Diffusion During Processing of TMCs	117
	3.1.2.4 Analysis of SCS-6 Fibers by Fourier Transform Infrared (FTIR) Spectroscopy	117
	3.1.2.5 Oxidation Resistance and Protection from Environmental Embrittlement	118
	3.1.2.6 Structure-Property Relationship in Orthorhombic Alloys	119
	3.1.2.7 Phase Evolution and Structure-Property Relations in Ti-25Al-25Nb	120
	3.1.3 COMPOSITE PERFORMANCE	121
	3.1.3.1 Tensile Behavior of SCS-6/Ti-24.5Al-17Nb and SCS-6/Ti-24.5Al-17Nb-1Mo Composites, and Issues of Fiber Strength Utilization	121
	3.1.3.2 ADDA Software for Local Strain Measurements in Composites	123
	3.1.3.3 Fracture and Deformation Mechanisms in Discontinuously Reinforced Aluminum (DRAs)	123
3.4	SUMMARY OF CURRENT WORK NOT REPORTED	124
3.5	PUBLICATIONS	125

TABLE OF CONTENTS (Continued)

<u>SECTION</u>		<u>PAGE</u>
3.6	PRESENTATIONS	130
3.7	LIST OF BOOK CHAPTERS	131
3.8	REFERENCES	131
4.0	TASK III. CERAMIC COMPOSITES	137
4.1	SUMMARY OF MAJOR FINDINGS	138
4.1.1	EXPERIMENTAL MECHANICS	138
4.1.1.1	Roughness Effects During Fiber Push-Out Tests	138
4.1.1.2	Roughness Effects During Progressive Debonding	138
4.1.1.3	Anticipated Effects of Roughness on Behavior of CMCs	139
4.1.2	CMC INTERFACES AND COATINGS	139
4.1.2.1	Fugitive Coatings	139
4.1.2.2	Oxidation of Carbon	140
4.1.2.3	Ductile/Fugitive Interface Coating	141
4.1.2.4	Segregant Induced Weakening	141
4.1.3	FIBER COATINGS	142
4.1.3.1	Cleavable Oxide Interphase for Oxide-Oxide Composites	142
4.1.3.2	Electrostatic Enhanced Sol-Gel Coating of Fibers and Cloths	143

TABLE OF CONTENTS (Continued)

<u>SECTION</u>	<u>PAGE</u>
4.1.3.3 TEM Specimen Preparation of Coated Ceramic Fibers	144
4.1.3.4 Hexaluminate Coatings on Commercially Available Polycrystalline Fiber Tows	145
4.1.3.5 Monazite Fiber Coatings	146
4.1.4 NEAR-TERM OXIDE-OXIDE COMPOSITES	148
4.1.4.1 Nextel™ 550, 720/Carbon/MAS, CAS	148
4.1.4.2 Nextel™ Fabric (550 and 720)Carbon/Mullite	148
4.1.4.3 The Mean Tensile Strength and the Weibull Modulus of Ceramic Filaments	150
4.1.4.4 The Effect of Thermal Exposure on the Strengths of Nextel™ 550 and 720 Filaments	150
4.1.4.5 ARPA-Salt Water Effect on BN/Nicalon™	151
4.1.5 YTTRIUM ALUMINATES	152
4.1.5.1 Fracture Toughness of YAG Single Crystal	152
4.1.5.2 $Y_4Al_2O_9$ - Y_2O_3 Eutectic	152
4.1.5.3 Oxide/Intermetallic Composites	152
4.1.5.4 High Temperature Environmental Stability of Yttrium Aluminates	153
4.1.5.5 YAG Powder Synthesis	153
4.1.5.6 Residual Stress Measurement	153

TABLE OF CONTENTS (Continued)

<u>SECTION</u>	<u>PAGE</u>
4.1.6 MISCELLANEOUS	155
4.1.6.1 SiC-Whisker Reinforced Mullite/Zirconia	155
4.1.6.2 Yttria-Stabilized Cubic Zirconia	155
4.1.6.3 Freeze Forming of Ceramics	156
4.2 SUMMARY OF CURRENT WORK NOT REPORTED	158
4.2.1 FIBER COATINGS	158
4.2.1.1 Stability of Hexaluminates with SiC in Air	158
4.2.1.2 Microcomposites of Sapphire-Hibonite-Alumina	159
4.2.1.3 Porous Oxide Coating	159
4.2.2 NEAR-TERM OXIDE-OXIDE COMPOSITES	160
4.2.2.1 Nextel™ 550, 720/Carbon/MAS, CAS	160
4.2.2.2 Nextel™ Fabric (550 and 720)/Carbon/Mullite	161
4.2.3 YTTRIUM ALUMINATES	161
4.2.3.1 Effect of Yttria Doping on Creep of Alumina	161
4.3 PUBLICATIONS	164
4.4 PATENT	169
4.5 DISCLOSURE AND RECORD OF INVENTION	169

TABLE OF CONTENTS (Continued)

<u>SECTION</u>		<u>PAGE</u>
5.0	TASK V. SUPPORT AND MAINTENANCE	170

LIST OF ILLUSTRATIONS

<u>FIGURE</u>		<u>PAGE</u>
2-1	Tensile Creep Data for Nb-10Si Alloys from Individual Tests.	11
2-2	Normalized Creep Plot for Nb-10Si as a Function of Stress.	11
2-3	Comparison of Tensile Creep Data for Nb-10Si Obtained from Individual Creep Tests Vs. Stress Increment Tests.	12
2-4	Comparison of Creep behavior of Nb-10Si at 1200°C with Creep Data for the Constituent Phases.	13
2-5	Comparison of Tensile vs. Compressive Creep Behavior of Nb-10Si.	15
2-6	Comparison of Compressive Creep Behavior of Extruded Nb-10Si and Nb-16.5Si vs. Directionally Solidified (DS) Nb-16Si.	16
2-7	TiAl Phase Diagram Based upon DTA Data and the Phase/Composition Analysis.	26
2-8	Lamellar Spacing as Function of Cooling Rate in Ti-42.5 at.% Al and Ti-47 at.% Al, Showing the Hall-Petch Type Relationships.	27
2-9	RT Hall-Petch Relationship Between Yield Stress and Grain Size in TiAl Alloys Having Duplex or Near-Gamma and Fully-Lamellar Microstructures.	30

LIST OF ILLUSTRATIONS (Continued)

<u>FIGURE</u>		<u>PAGE</u>
2-10	An Analysis of the Hall-Petch Relationship in Fig. 2-9 by Combining the Grain Size Effect and the Deformation Anisotropy of the Lamellar Structure.	31
2-11	(a) R-Curve Behavior of Duplex and FI Materials at RT and (b) Strain Fields Measured Near the Crack Tips at the Onset of the Crack Propagation in TiAl Alloys.	34
2-12	Tensile Ductility and Fracture Toughness Against Grain Size for Duplex, Nearly-Lamellar and Fully-Lamellar Materials in TiAl Alloys.	34
2-13	General Yielding vs. Crack-Tip Local Yielding: (a) Measured Tensile Curves on Bulk Tensile Specimens; (b) Stress-Strain Curves in the Near-Tip Plastic Zones Estimated from the Plasticity Near the Crack Tip at the Onset of Crack Propagation for Duplex and Fully-Lamellar CT Specimens.	36
2-14	Relation Between Fracture Toughness, Grain Size and Lamellar Spacing in Fully-Lamellar Materials of Various Gamma Alloys.	37
2-15	Stress Exponent (n) Values for Duplex and Refined Fully-Lamellar Materials at 676°C and 800°C.	39
2-16	Larsen-Miller Plots of Time to 0.5% Creep Strain for Alloy K5 in Duplex and RFL Microstructural Forms, as Compared to those for Two Casting Alloys.	39

LIST OF ILLUSTRATIONS (Continued)

<u>FIGURE</u>	<u>PAGE</u>
2-17(a) SN Curves for Load-Controlled HCF of Alloy K5 in Duplex and RFL Microstructural Conditions in Air at 600°C, 800°C and 870°C Measured on Smooth Hour-Glass Fatigue Specimens.	41
2-17(b) SN Curves with the Maximum Stress Normalized to Yield Stress.	42
2-18 TMT Lamellar Grain Size as a Function of Boron Content in Forged Ti-47Al-xB and Ti-46.5Al-2Cr-3Nb-0.2W-xB after Alpha Treatment for One Hour.	47
2-19 Variations of Microstructural Type and Grain Size with Annealing Temperature (with respect to $T_a = 1320^\circ\text{C}$) in Alloy K5 which has a Modified ($\alpha + \beta$) Phase Field.	48
2-20 RT Flow Curves of Wrought TiAl Alloys in Various Fully-Lamellar Forms.	50
2-21 Schematic Alpha Forging Process, Cross-Sectional View of an α -Forged Plate, and the TMPAL Microstructure Consisting of Aligned Grains/Lamellae to the Material Flow Direction.	51
2-22 Yield Stress vs. Forging Speed and Temperature Measured in Radial (L) and Transverse (T) Directions in Alpha-Forged Pancakes.	52

LIST OF ILLUSTRATIONS (Continued)

<u>FIGURE</u>		<u>PAGE</u>
2-23	Weight Gain Data for Coated Nb-Ti-Cr-Al-Si Alloys after Cycle Oxidation Testing at 1200 and 1400°C.	67
2-24	Density of Thermal Point Defects in B32 LiAl.	78
2-25	Density of Thermal Point Defects in TiAl.	79
2-26	Density of Thermal Point Defects in TiAl-Nb.	80
2-27	Density of Thermal Point Defects in TiAl-Si.	81
4-1	The Creep Data Obtained on Undoped and Yttria-Doped Alumina are Shown Compared After Normalizing the Data for Grain Size	161

LIST OF TABLES

<u>TABLE</u>		<u>PAGE</u>
2-1	Nb-Ti-Hf(Cr)-Al-Si Alloy Compositions and EPMA Data.	20
2-2	Oxidation Data for Selected Nb-Ti-Hf(Cr)-Al-Si Alloys after Static Air Exposure at 1200°C/24 h.	21
2-3	First- and Second-Generation Gamma TiAl Alloys.	28
2-4	Effect of Alloying Modifications to the GE Alloy on Microstructures and Phase Equilibria.	66
2-5	Size Misfit in B2 NiAl.	76
2-6	Size Misfit in γ TiAl.	76
2-7	Size Misfit in B32 LiAl.	76

FOREWORD

This report was prepared by the Materials and Process Division of UES, Inc., Dayton, Ohio under Air Force Contract F33615-91-C-5663, Mr. John Kleek and Captain John Farraro of the Materials Development Branch were the Government Project engineers. The research reported herein covered the period 28 March 92 to 30 September 96.

SECTION 1.0

INTRODUCTION

The structural integrity of many Air Force systems depends critically on optimal performance of traditional materials and continued exploration/development of new material technologies. Two major requirements have driven new material technologies: (1) reduced weight of engineering components of aircraft and (2) increased operating temperature of engines. Success in meeting these requirements will lead to improved performance efficiency and fuel cost savings. Material systems based on intermetallics, advanced metallic composites, and ceramic composites have great promise in fulfilling these requirements. Additionally, the traditional or mature materials, including alloys of Be, Al, Mg, Ti, Ni and refractory metals, require continued engineering improvements and research to optimize their performance and to avoid costly in-service failures. While engineering developments based upon educated empirical approaches and accumulated experience must continue, the fundamental scientific understanding of material behavior at interlinked electronic, atomistic, and continuum levels is needed to provide a solid foundation for further advancements.

For the past 4-1/2 years UES has carried out experimental and theoretical research on three different classes of materials. These include advanced metalics, advanced metallic composites, and ceramic composites. This is the final report on progress made on various topics within the three broad categories of material types. The report contains a summary of major findings, a description of current work not reported earlier, and a list of publications/presentations/patents/book chapters.

SECTION 2.0

TASK I. ADVANCED METALLICS

2.1 ADVANCED INTERMETALLICS

Metallic systems based on niobium were extensively explored in the 1950's and 1960's as candidate materials for applications in aerospace structures, nuclear systems, rockets, and orbital maneuvering engines for spacecraft. While attractive in terms of strength, density, and melting temperatures, a major barrier to the use of niobium alloys for high-temperature applications is their catastrophic behavior under oxidizing environments. Efforts to improve the environmental resistance through modifications in alloy chemistry have produced marginal improvements, but it has been accompanied by degradation in other properties, including a significant loss of high-temperature capability. Recent work at General Electric has identified a series of Nb-Ti beta alloys that have significantly greater oxidation resistance than commercial Nb alloys. With a balance of alloying additions, a 200-400°C enhancement in temperature capability can be realized over commercial Nb alloys for an equivalent oxygen penetration. However, these alloys exhibit inadequate creep resistance at temperatures above 1100°C.

Ordered intermetallic compounds based on refractory metals may have the potential of meeting the high-temperature requirements of advanced turbine engines, with properties such as high melting temperatures, high stiffness, low densities, and good high-temperature strength/creep resistance. Under U.S. Air Force sponsored efforts, a number of refractory-metal aluminide and silicide compounds have been identified for potential applications in the 1000-1600°C temperature range. However, ordered intermetallics in monolithic form have limited prospects of providing the required balance of mechanical properties, as they suffer from inadequate damage tolerance and extremely low fracture toughness at low temperatures. The application of a composite engineering approach may overcome these limitations of the monolithic intermetallics. This concept has led to alloy development efforts oriented toward two-phase/multiphase

systems incorporating Nb-base alloys and the ordered intermetallic compounds (aluminides and silicides), wherein the goal is to achieve a balance of properties for structural use. The baseline alloys for this category were selected from among the ductile Nb-Ti base alloys developed by General Electric. These alloys have Nb:Ti ratios close to 1:1, and have additions of Al, Hf, and/or Cr for environmental resistance. While these alloying modifications resulted in improvements in oxidation resistance by factors of 100-1000, the alloys were deficient in high-temperature strength and creep resistance. Our alloying path, therefore, was directed toward addressing these deficiencies in the beta alloys. This involved the selection of one or more of these beta compositions and selectively alloying with Al or Si to create a multiphase, multicomponent system composed of a refractory solid solution and one or more aluminide or silicide intermetallics existing in equilibrium. Such an alloy system offers a potential advantage over the beta alloys in that the introduction of the intermetallic phases can result in reasonable high-temperature properties, while the ductile constituent can impart good low-temperature toughness. This alloying approach led to the identification of two further alloy classes, one with beta plus aluminide intermetallic, and the other with beta plus one or more silicide intermetallics.

The beta plus aluminide class of alloys may be the best understood by examining the Nb-Ti-Al system, where the regions of interest are the phase fields between the beta/ordered beta, the A15 Nb₃Al-base, and sigma Nb₂Al-base single-phase regions. By alloying the complex beta alloys with Al, it is possible to obtain two-phase or three-phase microstructures composed of beta, A15, and or sigma intermetallics. The continuous matrix in these alloys is the beta phase, with blocky precipitates of sigma (Nb,Ti,Hf)₂Al or (Nb,Ti,Cr)₂Al phases. These alloys lie within the single-phase beta region at temperatures above 1500-1600°C. Upon aging at lower temperatures, the sigma phase precipitates along grain boundaries and within the grains of the matrix beta phase. Depending on the Ti concentration, the beta phase itself may undergo ordering or further decompositions, as has been observed in the Nb-Ti-Al systems. Work on the beta+aluminide system was discontinued at Wright Laboratory, although the phase stability and

precipitation kinetics in the Nb-Ti-Al-Hf (or Cr) systems are still under investigation at the University of Cincinnati under the direction of Prof. V. Vasudevan.

Within the beta plus silicide class of alloy system, the Nb-Ti-Al beta alloys (modified with Hf or Cr) have been alloyed with Si to obtain multiphase alloys of beta plus one or more refractory silicides. This alloy class has shown promise as a potential high-temperature structural system, and has been extensively investigated in this laboratory. In a parallel vein, other refractory two-phase beta+silicide systems, such as Mo-Cr-Si, were explored because of potential for inherent oxidation resistance.

Within each of these categories, alloy development was oriented toward obtaining a reasonable combination of low-temperature damage tolerance, high-temperature strength/creep resistance, and environmental tolerance. The principal activities included defining alloy compositions and identification of phase equilibria and transformation paths that lead to specific microstructures for a balance of properties. The alloy systems were generally amenable to conventional processing techniques, such as arc-melting and ingot metallurgy. Discussed are the research efforts with attention focused on microstructures and key properties, such as strength, toughness, creep behavior, and oxidation resistance.

Two-phase Nb/Nb₅Si₃ alloys represent a model material system that has been extensively investigated. Studies have demonstrated that substantial improvements in low-temperature toughness can be obtained via ductile-phase toughening, while at the same time, maintaining reasonable high-temperature strength. As part of the effort to demonstrate the balance of structural properties achievable in these systems, the creep response of Nb/Nb₅Si₃ alloys was investigated. Results from the creep studies of two-phase Nb/Nb₅Si₃ as well as monolithic Nb₅Si₃ are also presented in this report.

2.1.1 SUMMARY OF MAJOR FINDINGS

2.1.1.1 Model Nb/Nb₅Si₃ Composites

Most of the published research on the Nb/Nb₅Si₃ composites before the present contractual period pertained to the Nb-10 at.% Si alloy [1-2]. The present work was undertaken to determine the strength and toughness of a wrought alloy with near eutectic composition, Nb-16.5 at.% Si, at temperatures from 25-1500°C. The increased Si content is known to decrease the volume fraction of the primary Nb particles and increase the overall volume fraction of the Nb₅Si₃ intermetallic phase. In the as hot extruded (1800°C, 3.5:1 ratio) and heat treated condition (1500°C/100 h), the volume fractions of primary Nb, eutectoid Nb and Nb₅Si₃ were determined to be 0.25 ± 0.08 , 0.345 ± 0.09 , and 0.405 ± 0.09 , respectively. Average sizes (diameter and length) ranged from 4 and 8 μm for the small Nb particles and 20 and 50 μm for the large Nb particles. The composite exhibited strength values of 671 MPa at room temperature, 625 MPa at 1200°C, 309 MPa at 1400°C, and 261 MPa at 1500°C. The average room-temperature fracture toughness was 12.8 MPa $\sqrt{\text{m}}$. The toughness increased somewhat with temperature, with a value of 17 MPa $\sqrt{\text{m}}$ at 1400°C. The fractographic observations indicated that the large primary Nb particles fractured in a cleavage-like mode at room-temperature and in a ductile fashion at 1200 and 1400°C. The small eutectoid Nb particles exhibited complete ductile rupture at all temperatures.

2.1.1.2 Synthesis and Fracture Resistance Behavior of Nb/Nb₅Si₃ Powder Metallurgy Composites

Research was carried out on this topic by Leslie S. Apgar in partial fulfillment of Ph.D. degree from University of Dayton. Madan G. Mendiratta, UES, Inc. was the co-thesis advisor. Following is a summary/conclusions of this research.

The synthesis and fracture resistance behavior of ductile particulate toughened (DPT) Nb/Nb₅Si₃ powder metallurgy (P/M) composites containing either angular or spherical shaped Nb particles of varying sizes (15 to 780 μm), oxygen levels and volume fractions (0.15 and 0.30) have been investigated. The effect of both oxygen and silicon content on the Nb particulate deformation behavior in the composites was assessed by studying the tensile deformation and fracture behavior in monolithic pure Nb and Nb-0.4 at.% Si P/M material with varying oxygen levels. The main conclusions from this study are as follows:

1) Relatively uniform, dense (>99.95%), crack-free, and interfacial-reaction-free composites were produced by mixing elemental (angular or spherical) Nb powder with Nb₅Si₃ powder. Consolidation was achieved using a combination of vacuum hot pressing (VHP) between 1550°C and 1650°C at a pressure of 34 MPa for three hours, followed by hot isostatic pressing (HIP) at 1600°C with a pressure of 205 MPa for six hours for composites containing 30 and 15 vol.% of spherical or angular shaped Nb particles ranging in sizes up to 125 μm .

2) For pure monolithic Nb a transition from ductile to brittle behavior occurs between 425 to 1800 ppm of oxygen. The addition of small amounts of Si (0.4 at.%) substantially reduces the tensile plasticity when the oxygen levels are above 240 ppm. At low oxygen levels (240 ppm) silicon additions appear to have no affect on the tensile or fracture behavior of monolithic Nb. The Nb (with Si in solid solution) particulate yield strength in the composite was calculated to be on the order of 720 MPa for 125 μm angular shaped Nb particles and increases with decreasing Nb particle size and Nb volume fraction and increasing Nb particulate oxygen levels.

3) Increase in crack-extension resistance with stable-crack advance -- a rising resistance curve (\mathcal{R} -curve) behavior -- was observed only in composites containing 30 vol.% of angular Nb particles ranging in size from 40 μm up to 125 μm . Determination of \mathcal{R} -curves for the composites indicated a maximum steady-state toughness increase of 520% over that for the

Nb₅Si₃ matrix for 125 μm angular Nb particles and decreased with decreasing Nb particle size. The initiation toughness appeared to be independent of Nb particle size and Nb particle oxygen content. Experimentally determined toughness values for these composites (30 vol.% angular Nb, with size ranging from 40-125 μm) was in agreement with predicted maximum toughness values using a crack-bridging-spring model.

4) Rising \mathcal{R} -curve behavior in composites containing 30 vol.% angular Nb particles ranging in size from 40-125 μm , was due to the presence of Nb particles bridging the crack wake. The bridging lengths and crack opening displacements (COD) at Nb particle failure, $2u^*$, increase with increasing Nb particle size, decreasing Nb oxygen level, and decreasing Nb yield strength. Longer bridge lengths and higher COD resulted in increasing the maximum toughening values. The bridge length consisted of approximately 45% intact Nb particles and 55% fractured Nb particles in the crack-wake, and the fracture mode of the bridging particles consisted of either cleavage, knife-edge, or ductile-dimple type fracture; indicating that the individual Nb particle bridges exhibited a range of different deformation and fracture behaviors. In addition, the measured volume fraction of the Nb particles in the bridge length corresponded only to 19%, compared to the actual 30% volume fraction of Nb particles in the composite, and was independent of particles size. The reduction in the observed volume fraction of angular Nb particles participating in the bridging process was due to the crack-tip deflection around Nb particles as a result of residual thermal stresses. The increase in crack extension resistance appears to be directly related to the strong but somewhat ductile Nb bridges as opposed to weak and highly ductile Nb bridges.

5) A change from unstable-crack extension (flat \mathcal{R} -curve) behavior to a stable-crack advance (rising \mathcal{R} -curve) behavior occurred with a change of the shape of the Nb particle from spherical to angular or with an increase in the angular Nb volume fraction from 0.15-0.30. Composites containing 30 vol.% spherical 125 μm Nb particles did not produce crack bridging, due to ease in crack deflection around the spherical particles. Crack deflection, rather than crack

bridging was responsible for a small increase in fracture toughness, 120% for 30 vol.% spherical Nb particles and only 67% for 15 vol.% spherical Nb particles, over the matrix toughness. For composites containing 15 vol.% Nb, the fracture toughness was independent of both particle size and shape. Crack deflection was the direct consequence of residual thermal stresses in the composite due to high temperatures used in composite processing. The crack deflection path followed the contours of the spherical particles as a result of both particle geometry and residual stress field geometry, preventing crack-tip Nb particle interaction which would, subsequently, have resulted in the formation of Nb particle bridges.

6) This work demonstrated that by proper selection of size, shape, and volume fraction of tough Nb particles, it is possible to obtain a substantial increase in fracture resistance in the Nb/Nb₅Si₃ composites.

2.1.1.3 Unconstrained and Constrained Tensile Flow and Fracture Behavior of an Nb-1.24% Si Alloy

Studies on various Nb/Nb₅Si₃ composites [1-3] indicate that the room temperature mechanical properties -- specifically toughness -- are principally governed by the constrained deformation and fracture behavior of the Nb phase. In these composites, a variety of fracture modes and micromechanisms associated with the "ductile" Nb phase have been observed, which complicate the interpretation of the composite behavior within the recent theories involving bridging of cracks by ductile phases. The degree of constraint imposed by the high-modulus, elastic, brittle intermetallic matrix, determines the elevation of the stress experienced by the ductile phase as well as the shape of the load-deflection curve for the ductile phase. The area under this curve is a measure of the toughening increment over that of the brittle matrix. However, the fracture processes, especially cleavage fracture, can limit the plasticity of the reinforcement. The constrained deformation and fracture processes are functions of a number of complicated interacting factors, including the volume fraction of the phases in a composite, changes in local state of stress due to morphological aspects of the phases, cleavage fracture

strength of the phases, and the magnitude of local crack opening displacements relative to the size of the ductile phase.

This study was undertaken to isolate the deformation and fracture behavior of the ductile Nb phase in order to understand the more complicated mechanical behavior of the Nb/Nb₅Si₃ composites. Tensile tests have been carried out on smooth and notched specimens as a function of strain rate and temperature. The notched specimens were used to induce constrained plastic flow, and finite-element analysis (FEA) has been carried out to determine the state of stress and strain at the notch root radius. Important results of this investigation are that, at room temperature, while the smooth tensile specimens exhibited a totally ductile flow and fracture behavior, for a wide range of strain rates, the notched specimens exhibited cleavage-like fracture, corresponding to a critical combination of notch-root strain and high-axial tensile stress component. At room temperature, the maximum principal stress component at which the cleavage crack propagated was determined to be 930 MPa at an effective strain of ~ 0.05 ; this should be contrasted with the true fracture stress of ~ 760 MPa, at a strain of 0.5, for the unnotched tensile specimen exhibiting totally ductile fracture. From these results it was inferred that in the wrought Nb-10 at.% Si composite, the observed high degree of toughening ($K_Q \approx 25$ - 30 MPa $\sqrt{\text{m}}$) and the totally ductile fracture of the Nb phase, are due to occurrence of crack-tip plastic zone processes such as blunting and microcracking of the intermetallic matrix which reduce constraint on the Nb phase.

2.1.1.4 Evaluation of Cr₂Nb/(Cr) and Cr₂Nb/(Nb) Composites as High Temperature Structural Materials

The microstructural stability and mechanical properties, including strength, ductility, toughness, and creep and oxidation resistance of near eutectic Cr₂Nb/(Cr), Cr₂Nb/(Nb) and Ti- and Al-modified Cr₂Nb/(Nb) composites have been investigated. All composites exhibited excellent microstructural stability up to 1500°C. The Cr₂Nb/(Cr) composite exhibited high

strength levels of 400 MPa and 230 MPa at 1200 and 1400°C, respectively. However, from room temperature to 1000°C, its toughness values were very low (≤ 6 MPa $\sqrt{\text{m}}$). This low toughness was attributed to insufficient toughening provided by the Cr phase. The $\text{Cr}_2\text{Nb}/(\text{Nb})$ and the Ti- and Al-modified $\text{Cr}_2\text{Nb}/(\text{Nb})$ composites exhibited reasonable levels of toughness, high-temperature strength, and oxidation resistance with a possibility of further enhancement of toughness through composition control. However, as compared to the creep of composites based on intermetallic silicides toughened with (NbTi) beta phases, the creep resistance of the present $\text{Cr}_2\text{Nb}/(\text{Nb})$ based composites was found to be significantly lower. Therefore, it was concluded that both the $\text{Cr}_2\text{Nb}/(\text{Cr})$ and $\text{Cr}_2\text{Nb}/(\text{Nb})$ systems do not warrant further investigations for development as high temperature structural materials, especially when compared to considerable progress made on the silicide/(NbTi)-based composites.

2.1.1.5 Creep of Nb-Si Alloys

Individual creep tests were conducted on Nb-10Si alloys in tension at 1100, 1200, and 1350°C and at stress levels between 10-40 ksi (69-276 MPa). Figure 2-1 shows the creep data plotted as creep rate vs. stress. In the temperature and stress ranges investigated, the creep data obeyed the power law, with stress exponents ranging from 2.6-2.8. Figure 2-2 shows a normalized creep plot as a function of stress, where the creep rate has been normalized with respect to temperature. The data in the temperature range from 1100-1300°C could be fitted to a straight line, giving an average stress exponent of 2.7 and an apparent activation energy of 216 kJ/mol. This activation energy is close to the activation energy obtained for creep in Nb_5Si_3 monolith, which in turn, was equivalent to the activation energy for bulk diffusion of Nb in Nb_5Si_3 .

In addition to the individual creep tests, incremental stress change tests were conducted in tension on extruded Nb-10Si alloys at 1100, 1200, and 1300°C and at stress levels of 626 ksi (41-179 MPa). Figure 2-3 compares the tensile creep data for Nb-10Si obtained from creep tests

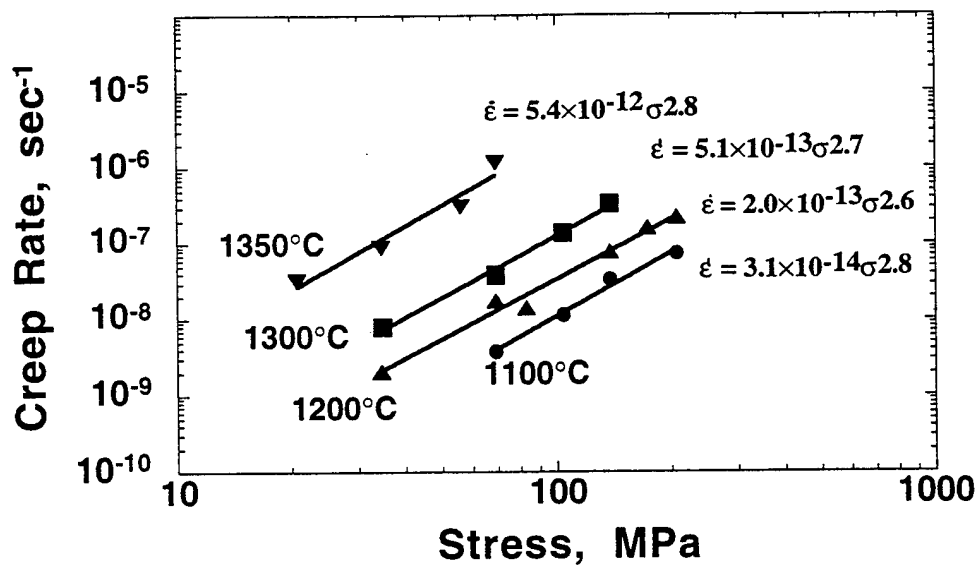


Figure 2-1. Tensile Creep Data for Nb-10Si Alloys from Individual Tests.

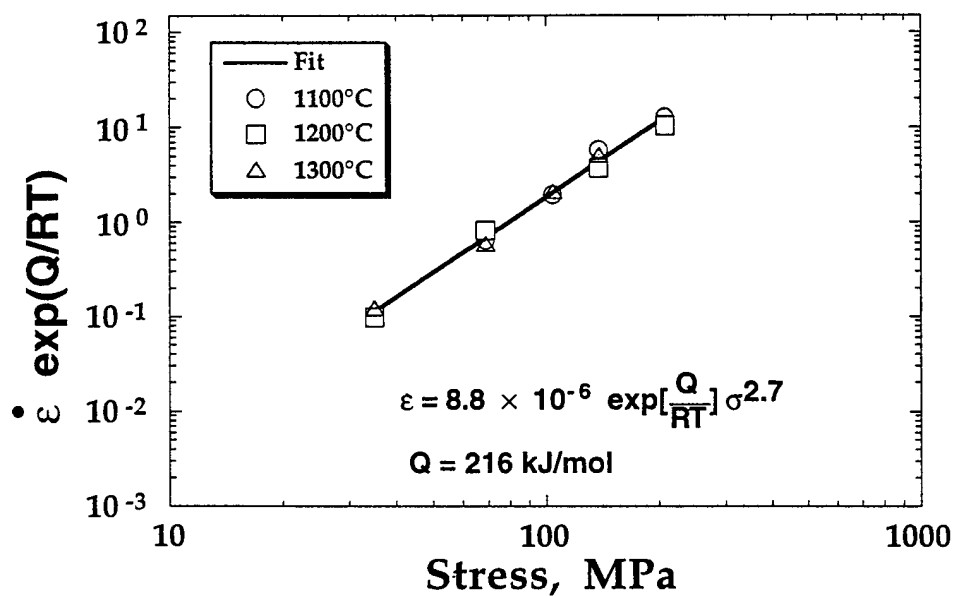


Figure 2-2. Normalized Creep Plot for Nb-10Si as a Function of Stress.

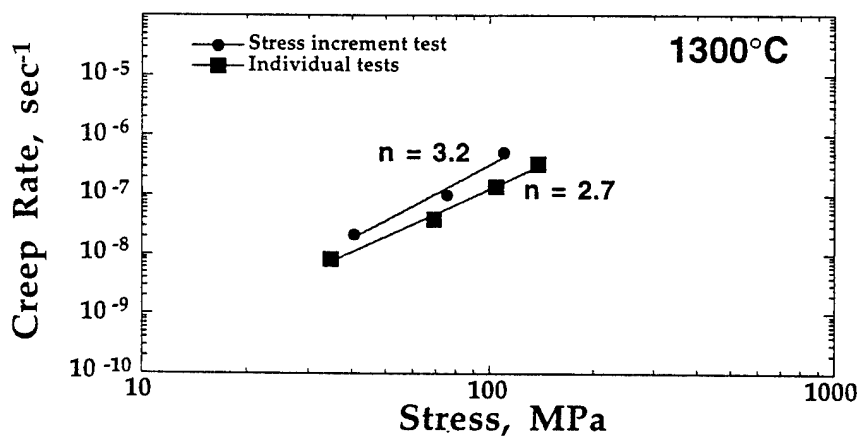
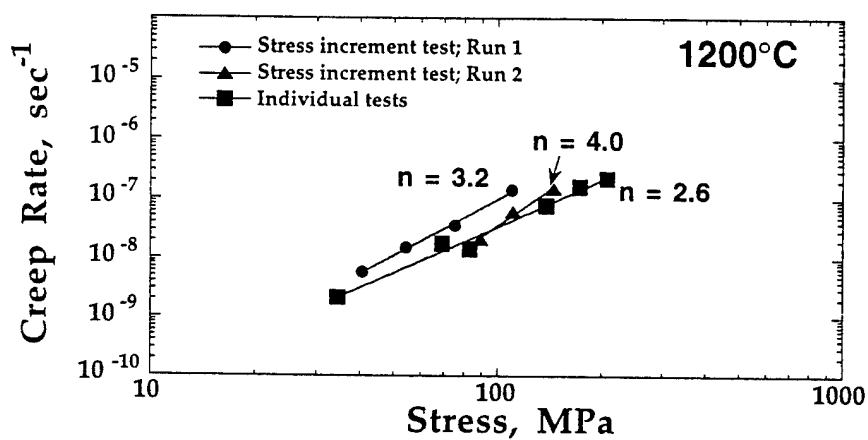
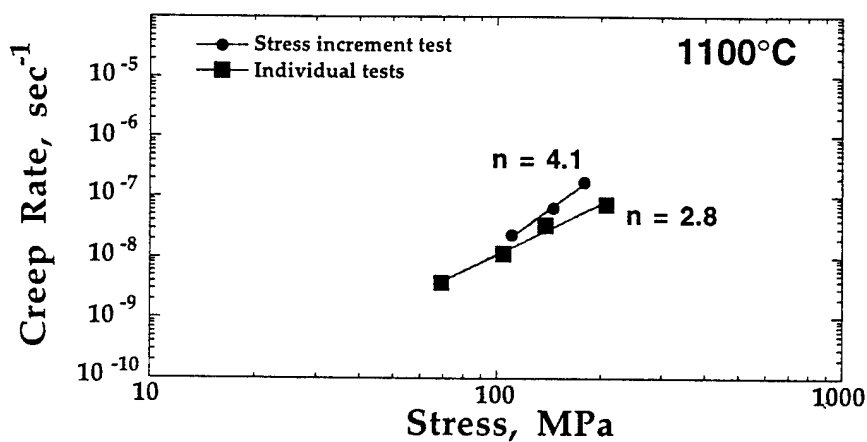


Figure 2-3. Comparison of Tensile Creep Data for Nb-10Si Obtained from Individual Creep Tests Vs. Stress Increment Tests.

on individual samples for each stress value vs. stress increment tests. It is observed that the incremental stress creep data are typically characterized by higher stress exponents than those obtained from the individual creep data. Such behavior can be correlated with the damage mechanism observed in the crept specimens from the incremental stress change tests.

Tensile creep tests were completed on an extruded (Nb) solid solution alloy of composition Nb-1.2 at.% Si at 1200°C and at stress levels between 5-13 ksi (35-90 MPa). The solid solution alloy corresponds to the composition of the beta phase constituent of the Nb-10Si alloy. Figure 2-4 compares the creep behavior of Nb-10Si at 1200°C with creep data for the constituent phases, namely, (Nb) solid solution and Nb₅Si₃.

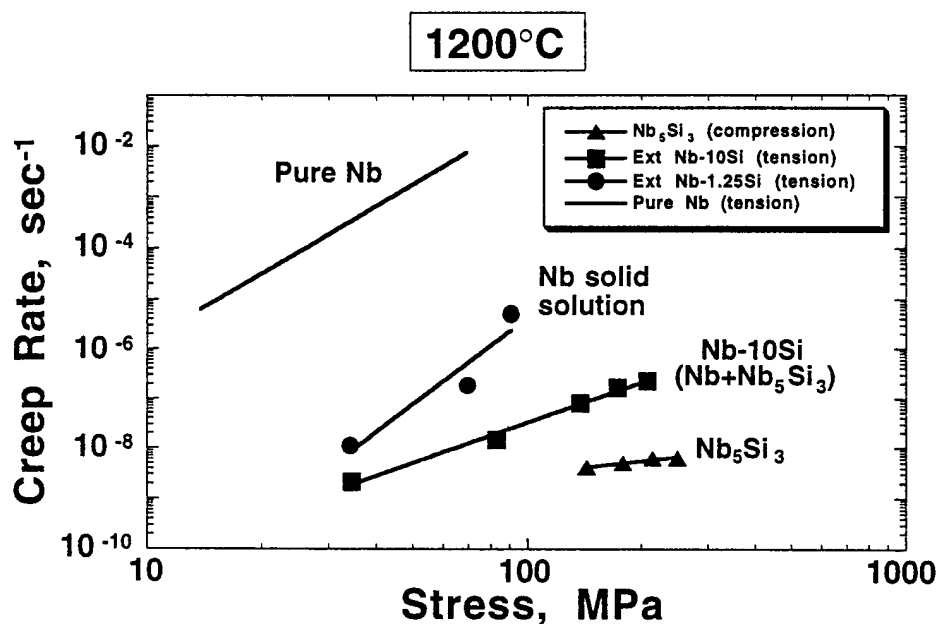


Figure 2-4. Comparison of Creep behavior of Nb-10Si at 1200°C with Creep Data for the Constituent Phases.

In addition to the tensile creep tests, compression creep tests were conducted on Nb-10Si at 1100, 1200, and 1300°C. The tensile vs. compressive creep behavior of Nb-10Si are compared in Figure 2-5; data from an unpublished report by G. Corman of General Electric Corporate Research and Development (GE-CRD) are also included for comparison. At all three temperatures, the compressive creep rates are higher than tensile creep rates, although the stress exponents are similar in both cases. This difference in creep behavior may be explained on the basis of the difference in creep damage in tension vs. compression. In the case of tensile creep, the ductile (Nb) phase undergoes plastic deformation within the Nb₅Si₃ matrix. Finite element analyses have shown that, for a remote applied stress of 207 MPa, the axial stress on the Nb₅Si₃ matrix adjacent to the Nb-Nb₅Si₃ interface can reach as high as 550 MPa, which is sufficient to crack the Nb₅Si₃ matrix. SEM examination was conducted on longitudinal sections of specimens crept in tension. The results showed several cracks in the Nb₅Si₃ matrix adjacent to the large primary (Nb) dendrite and running normal to the loading direction. Creep failure occurs as a result of the cracks in the Nb₅Si₃ matrix linking up, in combination with the ductile rupture of the (Nb) phase. In the case of compressive creep, the specimens showed macroscopic barreling. SEM examination of longitudinal sections of the crept specimens showed bending and buckling of the (Nb) dendrites. After high creep strains, it is observed that the elongated (Nb) dendrites have almost bent 90° with respect to the stress axis. These characteristics may contribute to a higher macroscopic creep rate in compression over that of tension.

Compressive creep tests were also conducted on extruded and heat-treated Nb-16.5Si at 1200°C. This alloy is closer to the eutectoid composition and contains a higher volume fraction of the Nb₅Si₃ phase. Figure 2-6 compares the creep behavior of Nb-10Si vs. Nb-16.5Si in compression at 1200°C. The stress exponents were observed to be similar in both cases. Several compression creep specimens of directionally solidified (DS) Nb-16Si were obtained from Bernard Bewlay, General Electric Corporate R&D for creep evaluation. The samples were grown by the Czochralski technique at GE. In the as-DS condition, this alloy had a microstructure of primary (Nb), along with an eutectic mixture of Nb+Nb₃Si. The compression specimens were

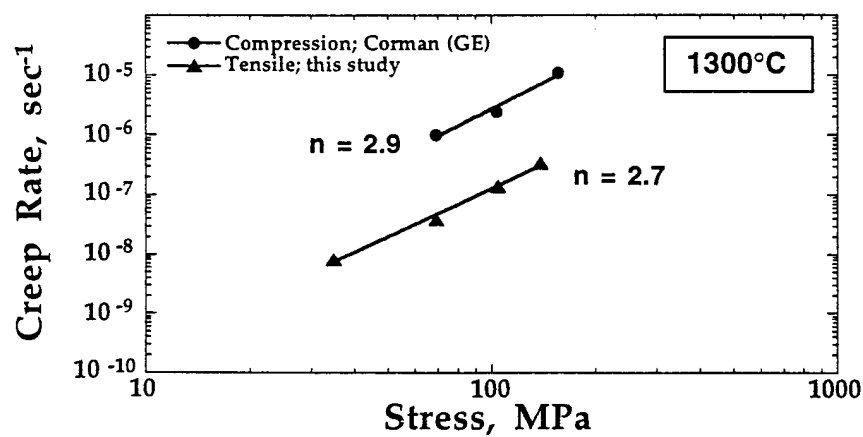
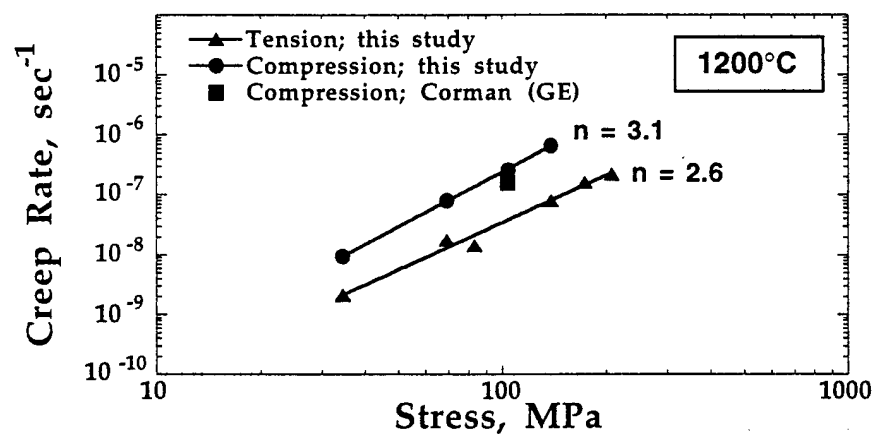
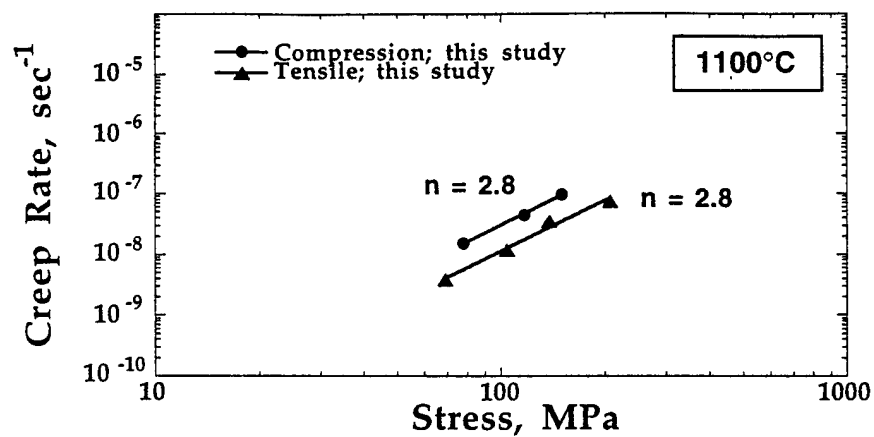


Figure 2-5. Comparison of Tensile vs. Compressive Creep Behavior of Nb-10Si.

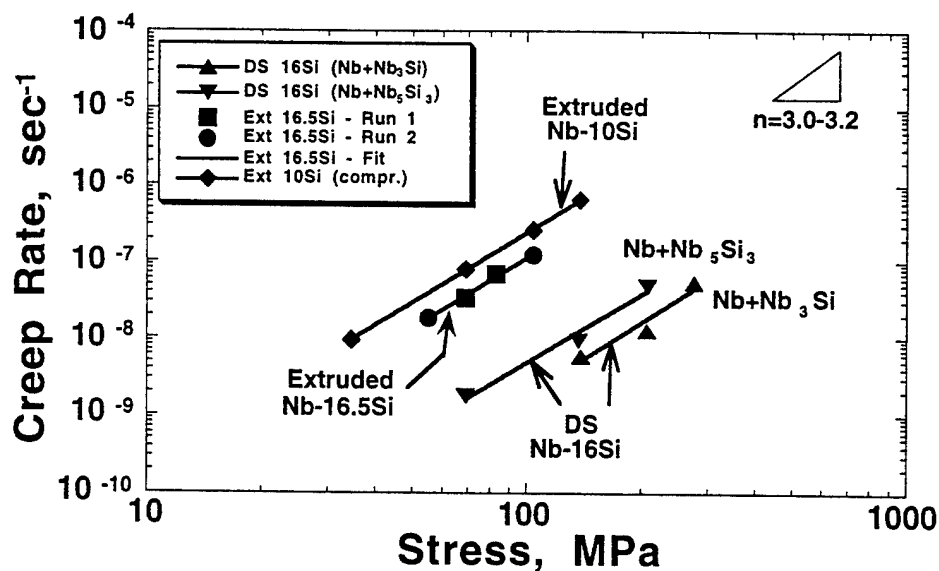


Figure 2-6. Comparison of Compressive Creep Behavior of Extruded Nb-10Si and Nb-16.5Si vs. Directionally Solidified (DS) Nb-16Si.

heat-treated at $1500^\circ\text{C}/100\text{ h}$ and $1500^\circ\text{C}/200\text{ h}$. Following the first heat-treatment, the microstructure consisted predominantly of (Nb) and Nb_3Si ; the second heat-treatment converted this microstructure to primary (Nb) and an eutectoid mixture of $\text{Nb}+\text{Nb}_5\text{Si}_3$. This allows us to provide a direct comparison of creep behavior of the DS alloy with the extruded alloy of the same composition. Compressive creep experiments were performed on this alloy at 1200°C for both microstructures, namely, $\text{Nb}+\text{Nb}_3\text{Si}$ as well as $\text{Nb}+\text{Nb}_5\text{Si}_3$. The resultant data are compared in Fig. 2-6 with the data for extruded Nb-16.5Si. It is observed that the DS alloy had much lower creep rates than the extruded alloy of the same composition, although the stress exponents were similar.

A paper incorporating the above results and entitled, "Creep Behavior of Nb/ Nb_5Si_3 In Situ Composites," was presented at the 1994 Materials Research Society Fall Meeting in Boston, MA on November 30, 1994.

Compression creep tests of monolithic Nb₅Si₃ were completed in the temperature range 1100-1400°C at stress levels between 10-60 ksi (69-414 MPa). In the temperature range from 1200 to 1400°C and stress regime of 52 to ~174 MPa, the creep data can be described by the following relation:

$$\dot{\epsilon} = \frac{2.773 \times 10^{-22}}{kT} \exp\left(\frac{-28125}{T}\right) \sigma^{0.8 \pm 0.1}$$

Based on a stress exponent of ~1 and activation energy of 234 kJ/mol, it is suggested that creep of Nb₅Si₃ probably occurs by the Nabarro-Herring mechanism with bulk diffusion of Nb in Nb₅Si₃ as the probable rate-limiting process. However, inhibition of grain boundary sliding by precipitates at triple points is believed to assist crack nucleation and propagation, thereby limiting the creep ductility in this material.

2.1.1.6 Mo-Cr-Si Beta + 3:1 Silicide Alloys

The invention disclosure, "High -Temperature Melting Molybdenum-Chromium-Silicon Alloys," describes a Mo-Cr-Si alloy system which possesses a range of desirable microstructures, excellent microstructural and morphological stability, and superior oxidation resistance at temperature ranges extending from 1000°C up to 1500°C. Such systems are continually sought for advanced aerospace propulsion systems and air vehicles. This material system possesses a two-phase microstructure consisting of a ductile phase and an intermetallic matrix, and which shows low metal recession rates combined with an adherent, continuous scale formation upon exposure to air at 1200°C.

The Cr-rich end of the Cr-Si phase diagram showed a wide two-phase field between the terminal Cr solid solution and the intermetallic phase Cr₃Si. This two-phase field is stable up to 1705°C. The Cr phase melts at 1863°C, while Cr₃Si melts at 1825°C. It is known that while

Cr_3Si is a highly creep-resistant phase, alloying with Mo will produce a further improvement in creep resistance over the binary intermetallic compound. The Cr-Mo-Si ternary phase diagram shows the existence of the phase $(\text{Mo,Cr})_3\text{Si}$, which essentially is a phase with continuous solid solubility between Cr_3Si and Mo_3Si . Further, the $(\text{Mo,Cr})_3\text{Si}$ phase is in equilibrium with the terminal (Mo,Cr) solid-solution phase over a large composition field.

Alloy compositions having Mo:Cr ratio of 20 (in atomic percent) and two different Si concentrations were selected for evaluation. Based on the compositions, the beta phase is a (Mo,Cr) solid solution phase with ~ 2.8 at.% Si in solid solution and the intermetallic phase the $(\text{Mo,Cr})_3\text{Si}$. From the phase analysis, it is evident that the two-phase field between (Mo,Cr) solid solution and $(\text{Mo,Cr})_3\text{Si}$ is thermochemically stable between 1200 and 1500°C, with little change in compositions.

Specimens from the annealed alloys were screened for oxidation behavior by exposure at 1200°C/24 h in an air furnace. The oxidized alloys showed a green surface oxide layer, which was rich in Cr, and which appeared to be uniform and continuous. The metal recession rates for the alloy with 16 at.% Si and 13 at.% Si were determined to be 8.1 $\mu\text{m/h}$ (0.32 mils/h) and ~ 1.4 mils/h, respectively. In terms of microstructure and oxidation response, the optimum Si concentration in the Mo-rich (Mo,Cr)- $(\text{Mo,Cr})_3\text{Si}$ two-phase field appears to be ~ 13 -14 at.% Si.

Bend testing of the alloy with 16 at.% Si, under four-point bending conditions, indicated that this class of alloys possess good high-temperature strengths up to 1400°C. Fracture strengths of 625 MPa (90.5 ksi) and 535 MPa (77.6 ksi) were obtained at 1000 and 1400°C, respectively. Based on the results of a microstructurally equivalent model system of Nb+ Nb_5Si_3 , the mechanical properties of such alloys will very likely be tailorable by varying the volume fraction of the constituent phases, and through appropriate thermomechanical treatments.

2.1.1.7 Nb-Ti-Hf(Cr)-Al-Si Alloys

Microstructural and oxidation studies have been completed on a series of Nb-Ti-Hf(Cr)-Al-Si alloys with compositions in the range (30-40)Nb - (28-33)Ti - (11.5-12)Hf or (8-9)Cr - (5-16)Al - (4-16)Si. SEM and EPMA after heat-treatment at 1500°C/100 h showed the alloys to consist of the terminal Nb-Ti base beta phase as well as Nb-base and Ti-base 5:3 silicides. Table 2-1 summarizes the various alloy compositions studied thus far, along with the compositions of the phases in these alloys after heat-treatment at 1500°C (or 1200°C). Oxidation screening studies were conducted by static air exposure at 1200°C/24 h and 1300°C/24 h. Metal recession was evaluated from SEM examination of the oxidized specimens, while oxygen penetration rates were obtained from microhardness profiles on the beta phase through the cross-section of the oxidized samples. Metal recession and oxygen penetration rates from the screening tests are listed in Table 2-2. Based on these studies, the Cr-containing alloys appeared to be most promising. The recession rates for the Cr-containing alloys were typically ≤ 0.1 mils/h at 1200°C and ~ 0.3 -0.5 mils/h at 1300°C. The oxygen ingress rates for the beta phase in these alloys were ~ 0.3 -0.4 mils/h at 1200°C. No further work was done on the Hf-containing system.

Two ingots of Nb-Ti-Cr-Al-Si with Si levels between 14 and 16 at.% Si were obtained from Pittsburgh Materials Technology, Inc., Large, PA. The ingots were canned in Mo and hot-extruded at 1300°C/4:1 and 1400°C/6:1. Smooth and notched bend bars were obtained from the extruded alloy with 14 at.% Si. Following annealing treatment at 1400°C/24 h, the samples were tested for room-temperature fracture toughness and bend strengths as a function of temperature. Bend strengths of 800, 1261, 715, 310, and 48 MPa were obtained at 25, 800, 900, 1000, and 1200°C, respectively. The alloy showed room-temperature fracture toughness ranging from 16 to 19.6 MPa \sqrt{m} .

Table 2-1. Nb-Ti-Hf(Cr)-Al-Si Alloy Compositions and EPMA Data.

Alloy Designation & Composition	Condition	Composition of Phases After 1500°C/ 100 h HT		
		Beta	5:3 Nb-Silicide	5:3 Ti-Silicide
<u>Nb-Ti-Hf-Al-Si</u>				
R1005 30Nb-29Ti-12Hf-15Al-14Si	Hypereutectic	40.2Nb-33.3Ti-8.1Hf- 18.5Al-0.0Si	21.7Nb-21.3Ti-18.0Hf- 8.5Al-30.5Si	
R1006 32Nb-32Ti-12Hf-12Al-12Si	Hypereutectic	41.4Nb-38.3Ti-7.0Hf- 13.3Al-0.0Si	23.5Nb-22.3Ti-16.2Hf- 5.9Al-32.1Si	16.3Nb-23.8Ti-21.6Hf- 7.3Al-31.0Si
R1195 35.7Nb-28.5Ti-12.2Hf-15.5Al- 8.1Si	Average eutectic composition from R1005	41.6Nb-32.3Ti-8.8Hf- 17.0Al-0.3Si	20.3Nb-19.9Ti-20.8Hf- 8.9Al-30.1Si	
R1196 36.9Nb-31.0Ti-11.5Hf-10.7Al- 9.9Si	Average eutectic composition from R1006			
R1197 37.1Nb-29.8Ti-12Hf-17Al-4.1Si	Hypoeutectic	39.5Nb-32.3Ti-10.3Hf- 17.6Al-0.3Si	19.1Nb-19.2Ti-22.3Hf- 10.0Al-29.4Si	
R1198 38.7Nb-32.6Ti-11.5Hf-12.2Al-5Si	Hypoeutectic			
<u>Nb-Ti-Cr-Al-Si</u>				
R1009* 40Nb-33Ti-8Cr-6Al-13Si	Hypoeutectic	43.8Nb-35.2Ti-12.5Cr- 7.8Al-0.7Si	37.7Nb-25.2Ti-0.5Cr- 1.7Al-34.9Si	26.9Nb-34.8Ti-1.2Cr -3.4Al-33.7Si
R1008* 37Nb-30Ti-8Cr-10Al-15Si	Hypoeutectic	39.3Nb-34.7Ti-11.0Cr- 14.4Al-0.6Si	41.2Nb-21.0Ti-1.3Cr- 7.0Al-29.5Si	27.7Nb-34.2Ti-1.6Cr -6.6Al-29.9Si
R1199 39.3Nb-30.1Ti-8.7Cr-10.8Al- 11.1Si	Average eutectic composition from R1008	41.6Nb-33.0Ti-11.9Cr- 12.5Al-1.0Si	36.9Nb-25.4Ti-2.1Cr- 6.0Al-29.6Si	32.0Nb-30.1Ti-1.7Cr -5.0Al-31.1Si
R1200 36.2Nb-33.4Ti-9.1Cr-5.4Al-15.9Si	Average eutectic composition from R1009	42.8Nb-35.8Ti-13.1Cr- 7.3Al-1.0Si	34.4Nb-27.2Ti-2.0Cr- 3.4Al-33.0Si	30.5Nb-30.7Ti-2.6Cr -2.8Al-33.4Si

* After 1200°C/100 h heat-treatment.

Table 2-2. Oxidation Data for Selected Nb-Ti-Hf(Cr)-Al-Si Alloys after Static Air Exposure at 1200°C/24 h.

Alloy Designation & Composition	Metal Recession mils/h	Oxygen Penetration mils/h
<u>Nb-Ti-Hf-Al-Si</u>		
R1005 30Nb-29Ti-12Hf-15Al-14Si	---	0.35
R1006 32Nb-32Ti-12Hf-12Al-12Si	~0.15	0.5
R1195 35.7Nb-28.5Ti-12.2Hf-15.5Al- 8.1Si	0.41	---
R1196 36.9Nb-31.0Ti-11.5Hf-10.7Al- 9.9Si	0.79	---
R1197 37.1Nb-29.8Ti-12Hf-17Al-4.1Si	0.91	---
R1198 38.7Nb-32.6Ti-11.5Hf-12.2Al-5Si	0.64	---
<u>Nb-Ti-Cr-Al-Si</u>		
R1009* 40Nb-33Ti-8Cr-6Al-13Si	0.1	---
R1008* 37Nb-30Ti-8Cr-10Al-15Si	0.08	0.38
R1199 39.3Nb-30.1Ti-8.7Cr-10.8Al- 11.1Si	0.14	---
R1200 36.2Nb-33.4Ti-9.1Cr-5.4Al-15.9Si	0.12	---

2.2 NANOLAYERED MATERIALS

2.2.1 SUMMARY OF MAJOR FINDINGS

2.2.1.1 Fabrication of Vapor Deposition System

A major activity in this area was the design, fabrication, and assembly of a physical vapor deposition (PVD) system for deposition of thin films and multi-layers by both magnetron sputtering and electron-beam evaporation. An existing clean room facility was modified with new power and water installations for this purpose. As part of the PVD system, the design, procurement, and installation of several subassemblies were completed, including the following:

(a) Water supply manifold, water flow switches, and pressure gauges. Water supply lines, filter, and return lines for the water recirculator were installed, along with the capability for supplying deionized water to the sputter cathodes.

(b) Vacuum valve drive panel. The vacuum valves incorporated in the PVD system are electro-pneumatic valves. The solenoid drive panel consists of 10 actuator switches, and 10 solenoids to operate any combination of vacuum valves or shutters for the sputter guns.

(c) Gas flow system. This includes the pressure regulation and metering for the vacuum chamber, load lock, and cryopump. The panel was designed to control the flow of the process gas, argon, as well as the purging gas, nitrogen.

(d) Installation of all blank flanges, vacuum valves, vacuum gauging, and electrical cables.

(e) Installation of the cryopump and all connecting cables.

(f) Configuration of the cryopump compressor and water cooling lines, roughing pump, roughing pump manifold, and all associated electronics.

(g) Installation of the specimen manipulator, and drive electronics.

A load-lock system was assembled and attached to the main chamber through a pneumatic gate valve. The load-lock system was designed to facilitate the loading of substrates to the main process chamber using a magnetically actuated loading arm, which transports the substrate holder into the process chamber and latches it into the rotary substrate manipulator. The load-lock system is independently pumped by an Alcatel turbo pump. Two 6-inch sputter guns were installed in the process chamber after mounting on linear drives that allow up to 4-inch travel. A baking system was procured for the main process chamber from BriskHeat. This system consists of an insulating jacket containing heating tapes that are designed to reach $\sim 250^{\circ}\text{C}$. The jacket is wrapped around the PVD chamber and is capable of being heated in three zones using independent controllers. An electron beam gun system consisting of two independent 100 cc capacity guns mounted on a 16.5-inch flange was procured from Thermionics. The drive system for the guns consists of a 15-kW power supply, position control, x-y beam sweep, and remote control for each gun.

2.2.1.2 Film Deposition

Sputter targets of pure Cu, Ni, and Nb were procured for initial testing and evaluation. Single crystal substrates consisting of 4-inch-diameter (100)Si wafers, 1-inch-diameter (100) NaCl, 1-inch-diameter (0001) sapphire, and 0.5-inch-diameter (100) Nb were procured from various sources.

In the first experiment, a 12- μm -thick copper film was deposited on a glass substrate. The copper deposit was peeled off the substrate and subjected to chemical analysis and X-ray diffraction. Interstitial analyses indicated an average concentration of 217 wppm oxygen and 39 wppm nitrogen, compared to 4 wppm oxygen and 0.6 wppm nitrogen for the bulk target material. X-ray analyses showed the Cu foil to be bcc. TEM examination of the Cu foil in plan view showed crystallites ranging in size from 200-1000 nm.

The next experiment consisted of mapping the temperature profile on the substrate holder during sputter deposition of Cu. Thermocouples were placed at four different locations on the back of the substrate holder. The sputtering of Cu was conducted at 500 W power input using argon at ~52 sccm flow rate and 4 m torr pressure. The substrate was kept stationary at a distance of 5.5" from the Cu target. The thermocouples showed an average temperature increase of ~100°C after 90 minutes of sputtering.

Following these initial experiments, efforts were initiated to deposit a Cu/Ni multi-layer film. The guns were loaded with Cu and Ni targets. While sputtering of Cu could be conducted without any problems, attempts to sputter Ni were unsuccessful. This difficulty is believed to be related to the magnetic behavior of Ni which is interfering with the sputtering process. A magnetron sputter gun capable of sputtering magnetic materials was procured from Kurt Lesker. This gun is capable of holding 4-inch-diameter target materials.

In the next experiment, efforts were made to deposit Cu/Nb multi-layers on (100)Si, (001) salt, glass, and Cu substrates. 11 layers of Cu and 11 layers of Nb were deposited at a power input of 500 W/gun and at 5 m torr argon pressure with an argon flow rate of 50 SCCM. Typical deposition times were 13 minutes for the Cu layers and 32 minutes for the Nb layers. Cross-sectional SEM examination showed that the Cu layers were ~200-300 nm thick, while the Nb layers were ~300-400 nm thick. The multi-layer films on Cu and Si substrate were intact at the end of the experiments, while those on salt and glass substrates peeled off. Interstitial analyses of the spalled multi-layers showed the presence of 2.8 wt.% oxygen and 2140 wppm nitrogen. It was determined that extensive bake-out of the PVD chamber is required for minimizing the interstitial contamination.

Current research is aimed at deposition of Cu/Nb multi-layers with low interstitial contamination. Following this, Cu/Nb multi-layers with various wavelengths will be deposited

with sufficient thickness so as to be amenable for bulk mechanical property measurements. The installation of the electron-beam evaporation system is planned for Spring 1997.

2.3 TiAl TECHNOLOGY DEVELOPMENT

2.3.1 SUMMARY OF MAJOR FINDINGS

2.3.1.1 Phase Relations and Microstructural Evolution

The mid-section of the Ti-Al binary phase diagram was established, as shown in Fig. 2-7. The sequence of phase transformations was investigated for alloy compositions, Ti-(30-55)Al, to find alpha decomposition paths, which are determined by cooling rate and method. Upon cooling, the alpha decomposition resulted in lamellar structures under relatively slow cooling ($0.05-1^{\circ}\text{C s}^{-1}$), Widmanstätten or "feathery"- type structures under air cooling, and massive gamma structures when water-quenched. The undercooling ($\Delta T_u = T_a - T_{\alpha/\gamma}$) required for the formation of the lamellar structures was measured to increase with increasing cooling rate. Naturally, lamellar spacing (l_L), which decreases with undercooling, depended on cooling rate (dT/dt) according to the relation, $l_L \sim (dT/dt)^{-1/2}$, Fig. 2-8. Ti-43Al yields finer lamellar spacing than Ti-47Al, indicating that lower aluminum content results in finer lamellar spacing under given cooling rate. The maximum cooling rate, above which the lamellar structure is disturbed by the formation of Widmanstätten structures, ranged from 1 to 4°C s^{-1} depending on composition and grain size. It is suggested that Widmanstätten structures are formed through first α -twinning followed by lamellar formation in both the matrix α grains and the α -twinned bands. The lamellar coarsen during subsequent cooling, depending on cooling rate.

Based on knowledge of the phase relations and transformations, four different types of standard microstructures were identified in wrought processed TiAl alloys: near-gamma, duplex, nearly-lamellar (NL), and fully-lamellar (FL) types. Duplex and FL microstructures have been

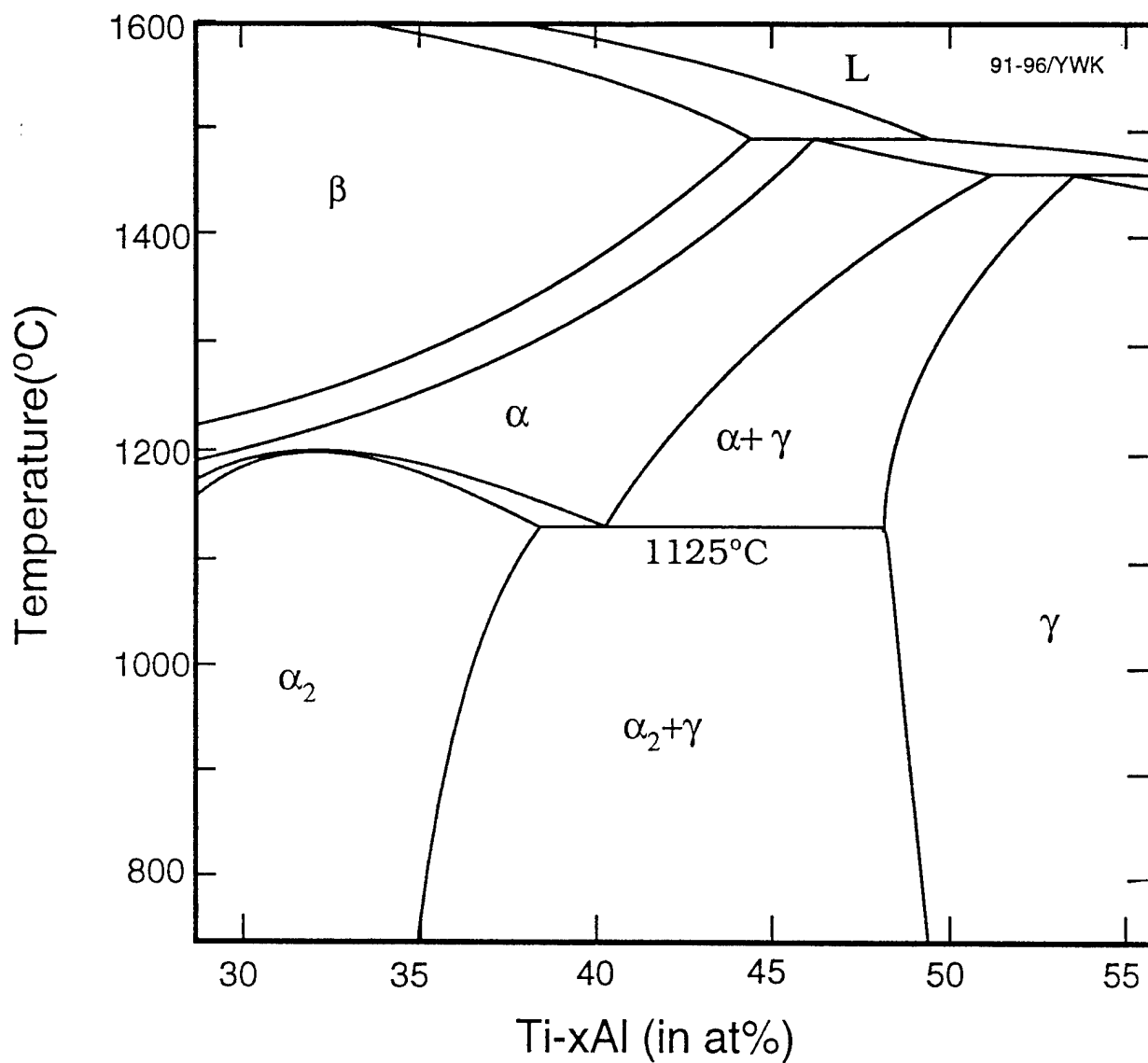


Figure 2-7. TiAl Phase Diagram Based upon DTA Data and the Phase/Composition Analysis.

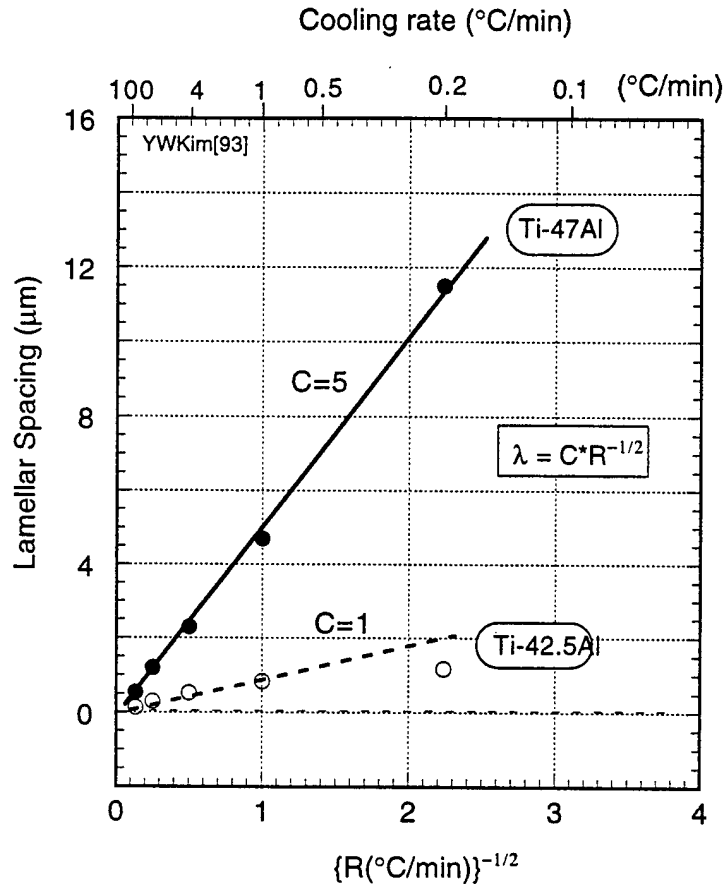


Figure 2-8. Lamellar Spacing as Function of Cooling Rate in Ti-42.5 at.% Al and Ti-47 at.% Al, Showing the Hall-Petch Type Relationships.

subjected to most investigation. A number of mechanical property measurements and evaluations have been conducted on these microstructures. In general, FL microstructures consist of large lamellar grains resulting in poor tensile properties, and duplex microstructures consist of fine grains which yield low toughness and creep-resistance. Investigations on both the room and elevated temperature deformation and fracture processes were also conducted. Microstructure optimization was attempted on the basis of the above described fundamental understanding, and production of the optimized microstructures into various product forms were attempted with successes. An effort was made in classifying and grouping all gamma alloys existing to date, as listed in Table 2-3.

Table 2-3. First-and Second-Generation Gamma TiAl Alloys.

Generation	Compositions (at.%)	Processing
1st	Ti-48Al-1V-0.3C	Wrought/PM/Cast
2nd	<u>Standard Alloys</u>	
(Current)	Ti-47Al-2Cr-2Nb	Cast Alloy
	<u>Modified Alloys</u>	
	Ti-47Al-2Mn-2Nb-7 vol.% TiB ₂	Cast XD Alloy
	Ti-(45-47)Al-2Nb-2Mn+0.8 vol.% TiB ₂	Cast XD Alloys
	Ti-47Al-1.6Fe-1.4V-2.4B	Cast Alloy
	Ti-47Al-3.5(Nb, Cr, Mn)-0.8(B, Si)	Cast Alloy
	Ti-47Al-2W-0.5Si	Cast Alloy
	<i>Alloy K5</i> (Ti-46.5Al-2Cr-3Nb-0.2W)	Wrought Alloy
	Ti-46Al-4Nb-1W	Wrought Alloy

2.3.1.2 Microstructure-Property Relationships

2.3.1.2.1 Hall-Petch Relation

The Hall-Petch (H-P) relationship between yield strength and grain size in FL microstructures was observed to exist with a large Hall-Petch constant of $k_y \sim 4 \text{ MPa}\sqrt{\text{m}}$ for grain sizes from 250-2600 μm and yield strengths from 290-500 MPa. This value is compared to that ($\sim 1.0 \text{ MPa}\sqrt{\text{m}}$) for fine gamma/duplex microstructures and that ($\sim 0.5 \text{ MPa}\sqrt{\text{m}}$) for polysynthetically twinned (PST) crystals in a hard orientation. This unusually large H-P constant is not readily explained, but it was considered to be related to the strong anisotropic flow stress behavior of the lamellar structure. The gage-diameter to grain-size ratio may also play a role in the unusual relation. The ratio ranged from 1.3-14 for the FL specimens. Therefore, the specimens containing large grains have only a few grains within the gage cross-section, thereby

rendering one or two soft grains to control the yielding process. A separate experiment was conducted to clarify the uncertainty in that a larger gage diameter (8 mm) was selected to contain larger number of grains in the cross section. According to this result, corrections were made to obtain $k_y \sim 2.3 \text{ MPa}\sqrt{\text{m}}$, Fig. 2-9. This value appears to be still unusually high. A possible explanation for this is suggested in Fig. 2-10 where a modified Hall-Petch constant ($k_d\lambda$) is obtained by combining the usual grain size (d) effect with the anisotropy effect which is a function of the lamellar spacing (λ_L).

2.3.1.2.2 Tensile Deformation and Fracture

The ductility of gamma alloys decrease, in general, with increasing grain size, and so do tensile strengths. The total strain in FL materials decreases from 2.5 to 0.5% as the grain size increases from 250 μm to 2500 μm . The decreases of tensile strength and ductility with increases of grain size in lamellar material can be explained using the characteristic anisotropy of tensile properties of lamellar structures and assuming that the fracture is controlled by the crack nucleation process involving the coalescence of dislocations under shear stress. In this process, the critical stress (σ^*) to generate the stress concentration (at the dislocation pileup) needed to initiate a microcrack can be expressed as a function of grain size (d), $d\sigma^{*2}=C$. Using this relation and the plastic flow equation, $\sigma=K\epsilon^n$, with the work-hardening coefficient (n) assumed to be constant, the complete stress-strain curves for the materials with two different lamellar grains ($d_1 < d_2$) can be constructed. This analysis shows that ductility is primarily controlled by the amount of general yielding which is greater for small grain sizes. A dislocation pileup nucleating a microcrack is achieved usually by either translamellar slip/twinning or additional interlamellar deformation. The microcrack usually forms in the translamellar direction often in the adjacent grain, although interlamellar microcracking should be possible depending on the lamellar orientation. The brittle-ductile transition temperature (BDTT) varied depending on alloy composition and microstructure and strain rate. For a given alloy, the BDTT increases with grain

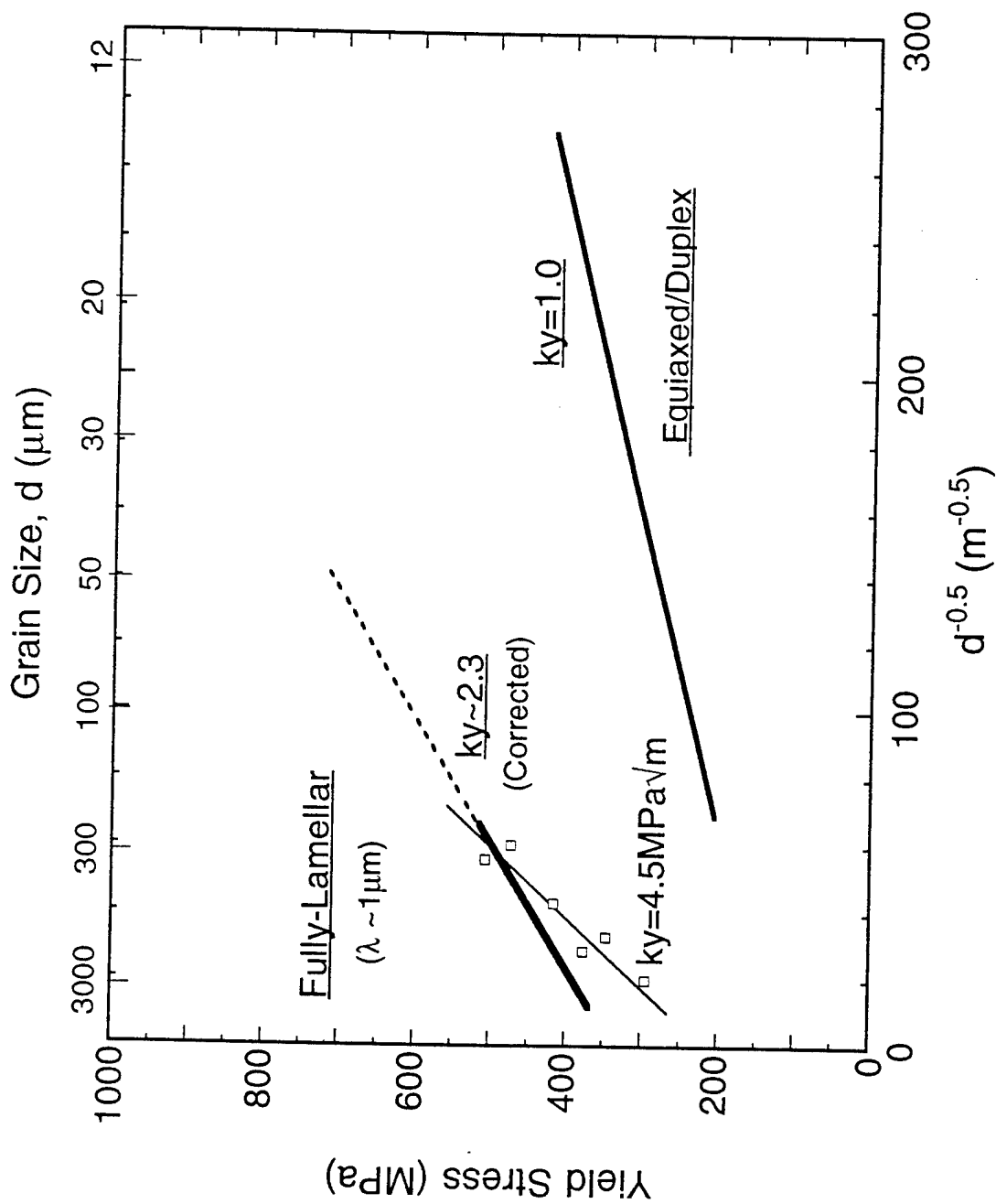


Figure 2-9. RT Hall-Petch Relationship Between Yield Stress and Grain Size in TiAl Alloys Having Duplex or Near-Gamma and Fully-Lamellar Microstructures.

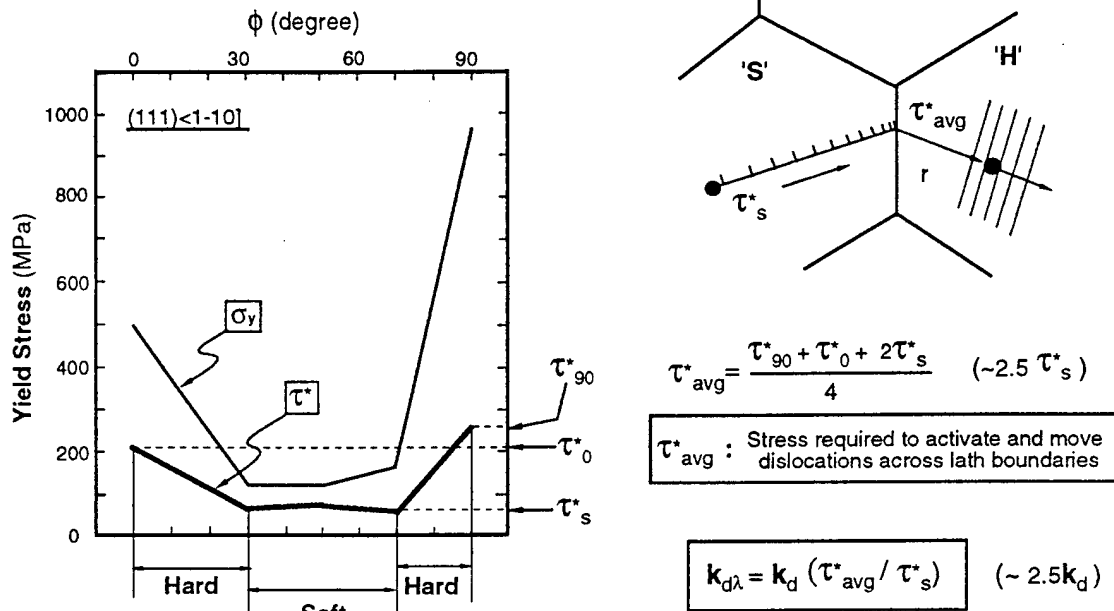


Figure 2-10. An Analysis of the Hall-Petch Relationship in Fig. 2-9 by Combining the Grain Size Effect and the Deformation Anisotropy of the Lamellar Structure.

size or with decreasing RT ductility. For a strain rate of $5 \times 10^{-4} \text{ s}^{-1}$, for example, it ranges from 650-700°C for duplex and from 800-850°C for FL. It is also very sensitive to strain rate, especially for duplex microstructures. The enhanced ductility above the BDTT appears to be the direct result of increases in both twinning/slip activity and systems.

For both materials, tensile strengths at temperatures below the BDTT depend on cooling rate and methods employed, with higher cooling rates yielding higher strength levels. In duplex microstructures, the α_2 phase is present in fine particle (instead of plate) forms with fast cooling rates. Finer lamellar spacings are resulted in NL and FL microstructures with increasing cooling rate. Transgranular and/or translamellar cleavage fracture is the dominant fracture mode at RT for both microstructures, although the fine duplex material occasionally shows intergranular failure. At temperatures above the BDTT, intergranular fracture prevails in duplex microstructures and

delamination and intergranular fracture become important for FL microstructures. In spite of the increased deformation activity with temperature, transmission of slip and twinning across GB's or lamellar interfaces appears to remain difficult. The apparent grain-boundary/interface weakening with increasing temperature has not elucidated yet.

2.3.1.2.3 Notch Fracture in γ -Titanium Aluminides

The notch fracture behavior of two γ titanium alloys, having duplex and fully-lamellar microstructures, has been investigated as a function of notch geometry and test temperature. The unnotched tensile properties and notch fracture loads are used to perform finite element analysis (FEA) to determine triaxial tensile stresses and effective plastic strains in the vicinity of notch roots. These results, together with fractographic examinations of notch failures, indicate that a crack nucleates in the triaxial tensile field below the notch tip where the effective von Mises stress just exceeds the uniaxial tensile yield stress. The high tensile stress component then propagates the nucleated microcrack to failure with local stress intensity reaching the toughness of the material. Thus, both plasticity and high tensile stress are required to cause notch failure. At room temperature, for the duplex and fully-lamellar materials, the fracture occurred at maximum principal stress and effective strain values of 600-650 MPa and 0.014 and 925 MPa and 0.01, respectively. These notch fracture values should be compared to those for the unnotched uniaxial tensile values i.e., 330 MPa and 0.018 for the duplex microstructure and 540 MPa and 0.018 for the fully lamellar microstructure. With increasing testing temperatures, the analyzed maximum principal stress at fracture (taken to be the fracture propagation stress) decreases gradually. For both microstructures, notch fracture can be quantified by simple fracture mechanics. Plasticity, as represented by von Mises criteria, initiates "Griffith" flaws which scale in size with microstructural features. Then, the peak component of triaxial tensile stress, acting on the flaws, causes final fracture once the combination of stress and the flaw size reaches the material fracture toughness.

2.3.1.2.4 Fracture Resistance

Fracture resistance experiments were conducted on CT specimens in air as well as in situ SEM vacuum environment. Duplex microstructures exhibited small plastic strain (about 3%) near the onset of crack extension and little resistance to crack propagation, whereas the FL structure yields large crack-tip plastic strains (about 20%) and increased resistance (which is a function of grain size) to crack propagation, Fig. 2-11. At RT, FL specimens show $K_{Ic}=16-20 \text{ MPa}\sqrt{\text{m}}$ and $K_{max}=25-42 \text{ MPa}\sqrt{\text{m}}$ at a displacement rate of 1×10^{-4} - $2 \times 10^{-2} \text{ mm/sec}$ and the duplex specimens show $K_{Ic}=K_{max}=11 \text{ MPa}\sqrt{\text{m}}$. The initiation toughness (K_{Ic}), a measure of the plasticity at the onset of the crack propagation, is related to the strain measured near the crack tip. The occurrence of crack growth resistance can be explained in terms of the redundant work expended in failing the ligaments formed in the wake of the crack. Translamellar deformation by either slip and/or twinning, either in the ligament or in front of the propagating main crack, often results in ultra-fine microcracks caused by plastic incompatibility at the lamellar interfaces. The absence of crack growth resistance behavior in duplex structures is directly related to the lack of bridging ligaments. The sensitivity of toughness to displacement or loading rate increases with temperature; for example, K_{Ic} and K_{max} values for the large-grained FL specimens at 800°C were measured to be $35 \text{ MPa}\sqrt{\text{m}}$ and $79 \text{ MPa}\sqrt{\text{m}}$, respectively.

2.3.1.2.5 Ductility Toughness Relationship

The measured inverse relationship between ductility and toughness, Fig. 2-12, is explained by relating the bulk tensile behavior and the crack-tip yielding behavior. As was discussed, the ductility is greater at small grain sizes. In toughness testing large ($>500 \mu\text{m}$) FL specimens, the crack-tip plastic zone encompasses only one or less grains in front of the crack tip, thereby confining the deformation behavior to the characteristics of those few lateral grains for thin specimens. The K_{Ic} is then closely related to the intrinsic ductility of the lamellar

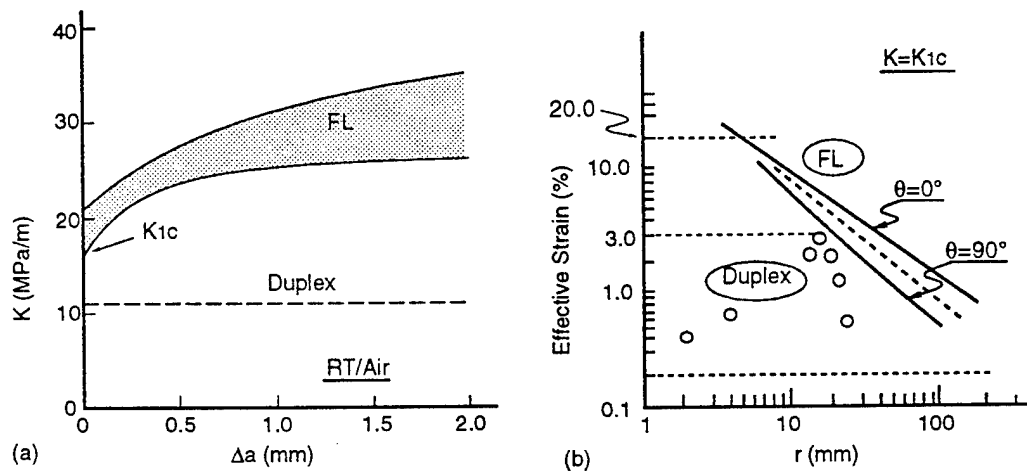


Figure 2-11. (a) R-Curve Behavior of Duplex and FL Materials at RT and (b) Strain Fields Measured Near the Crack Tips at the Onset of the Crack Propagation in TiAl Alloys.

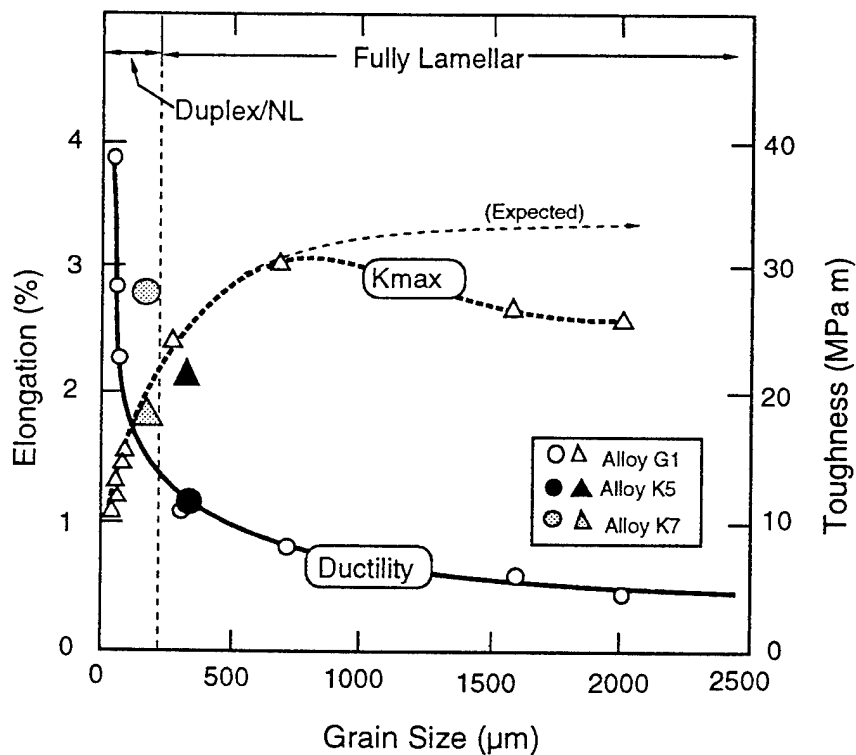


Figure 2-12. Tensile Ductility and Fracture Toughness Against Grain Size for Duplex, Nearly-Lamellar and Fully-Lamellar Materials in TiAl Alloys.

structure and can be used to estimate the tensile stress-strain curve of the sampled material. The near-tip effective strains measured in the lamellar structure, about 20% at the onset of crack propagation, are consistent with the interpretation.

Figure 2-13 compares the measured general tensile curves (a) and the estimated stress-strain curves within the near-tip plastic zone and (b) for coarse (larger than plastic zone size) FL and fine (10-40 μm) duplex (DP) materials. The stress-strain curves in the plastic zone were estimated using the following relationship between K_{Ic} and the local stress-strain curve,

$$(K_{Ic})^2 = C n E s_y e_{lf}$$

where C is a constant, n the local work hardening coefficient, E the elastic modulus, s_y the material's yield stress, and e_{lf} the local true fracture strain which corresponds to the maximum effective strain measured near the crack tip. The K_{Ic} values used for the estimation were 10.5 and 16 $\text{MPa}\sqrt{\text{m}}$, respectively, for the duplex and the FL materials. For FL materials, the plastic zone size (PZS) at the onset of crack initiation was calculated to be about 400 μm and can thus be contained within a FL grain in front of the crack tip. In this case, the local fracture strain is about 20% (Fig. 2-13). For duplex materials, the material within the plastic zone (which is estimated to be 300 μm in size and contains many randomly-oriented grains) is fairly isotropic and represents the bulk material with a fracture strain of about 3% (Fig. 2-13), and thus the near-tip plasticity is essentially identical to that of the bulk material. This analysis shows that the apparent inverse ductility-toughness relationship is caused simply by the difference in sampling between tensile testing and toughness testing. Within the plastic zone, the material obeys the classical relation between tensile properties and initiation toughness expressed by the above equation.

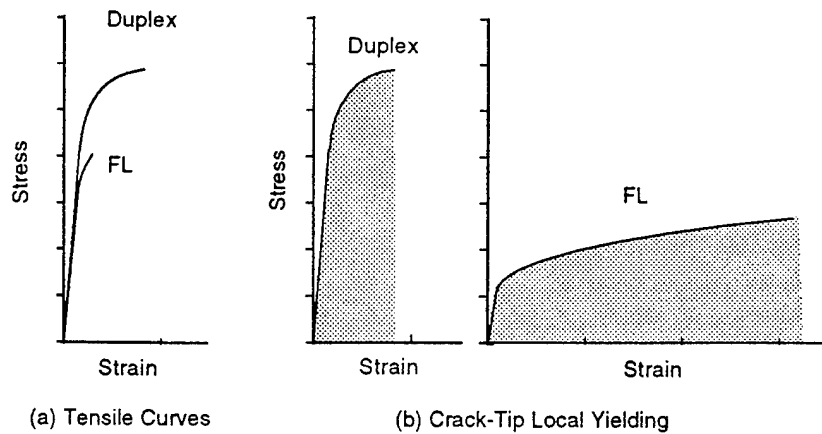


Figure 2-13. General Yielding vs. Crack-Tip Local Yielding: (a) Measured Tensile Curves on Bulk Tensile Specimens; (b) Stress-Strain Curves in the Near-Tip Plastic Zones Estimated from the Plasticity Near the Crack Tip at the Onset of Crack Propagation for Duplex and Fully-Lamellar CT Specimens.

2.3.1.2.6 Competition Between Grain Size and Lamellar Spacing on Toughness

The fracture toughness (K_{Ic} and K_{max}) increases with lamellar grain size up to about 500 μm , but appears independent of grain size for larger sizes, Fig. 2-14. In this constant toughness region, the plastic zone sizes at the onset of the crack propagation are calculated to range from 400-550 μm . For the larger grains, however, the fracture resistance (both K_{Ic} and K_{max}) and lamellar spacing (l_L) is seen to form a Hall-Petch type relationship in Fig. 2-14:

$$K_{max} \text{ (or } K_{Ic}) = K_0 + k_{lL}^{-1/2}$$

The increase in toughness with decreasing lamellar spacing can be explained in terms of increased stresses required for translamellar slip/twinning. The flow stresses of the lamellar structure in the hard orientation are higher than those of FL materials and increase to much higher levels with decreasing lamellar spacing. Interestingly, the K_{Ic} of the large-grained FL material appears to

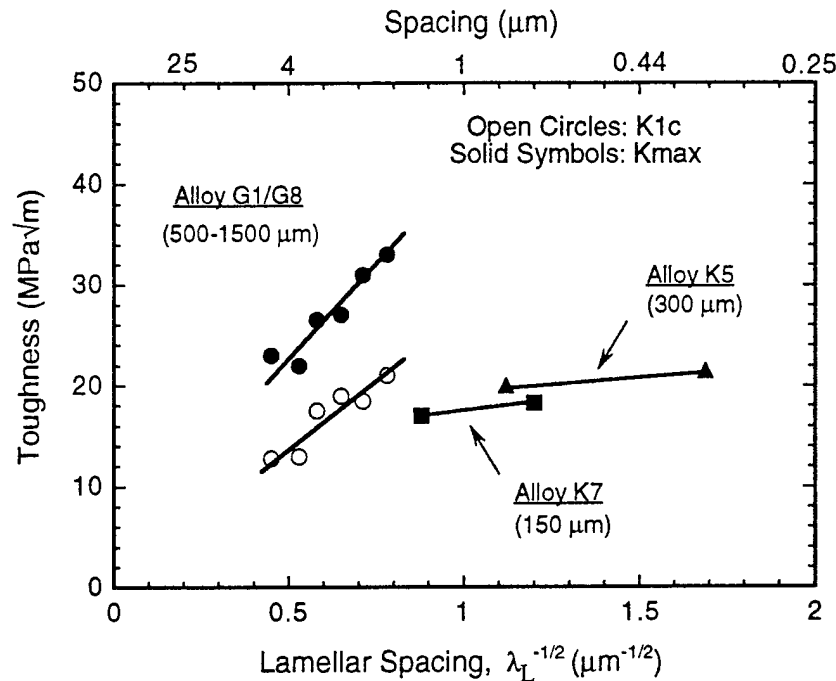


Figure 2-14. Relation Between Fracture Toughness, Grain Size and Lamellar Spacing in Fully-Lamellar Materials of Various Gamma Alloys.

approach that of duplex materials, about $10 \text{ MPa}\sqrt{\text{m}}$, when the lamellar spacing reaches about $10 \mu\text{m}$, suggesting that a coarsely spaced lamellar structure may behave like a fine grained material by losing the macroscopic anisotropy in deformation. When the grain size is smaller than the plastic zone size, the grain boundary effect on the toughness appears to prevail over the lamellar spacing effect. This prediction is evidenced from the test results for K5 and K7 alloy compact specimens containing, respectively, $300 \mu\text{m}$ and $150 \mu\text{m}$ lamellar grains, Fig. 2-14. In this grain size range, the variation of lamellar spacing between 0.4 and $1.2 \mu\text{m}$ does not alter the toughness, K_{max} , appreciably. The large drop in K_{max} values in this grain size range, compared to that in the large-grain range, is the direct result of the reduced resistance to crack propagation. The slight increases in toughness with decreasing lamellar spacing in this small-grain size range indicate that the Stroh stress nucleating a crack at the dislocation pile-up within the plastic zone develops at a slightly higher applied stress level with a small increase in fracture strain.

2.3.1.2.6 Creep Resistance

Creep test of alloy K5 showed that creep resistance of FL (300 μm) materials was superior to that of duplex (10 μm) materials under any stress levels at temperatures between 676°C and 870°C selected for this program. The difference in creep resistance increases with increasing temperature, which is evident in Fig. 2-15 where creep area is plotted against stress exponent (n). The creep behavior in these microstructural forms is compared with those of casting alloys in Larsen-Miller plot in Fig. 2-16. Clearly, RFL material is more creep resistant than casting alloys. The activation energy values were similar for both materials and ranged from 380-420 kJ/mol, depending on stress and temperature. The superior creep resistance for lamellar structures was explained in terms of composite-like strengthening in that α_2 plates acted as reinforcements. However, the fundamental mechanisms are basically yet unknown. Another creep experiment was conducted on FL alloy K5 modified with 0.1 at.% carbon at 760°C under a high applied stress of 276 MPa. Under the high stress, tremendous improvements in both the primary creep strain and the secondary creep rate were observed when the material was properly age-hardened. For example, the time for 0.3% creep strain was over 50 h when aged for 54 h at 900°C following cooling from the alpha phase field at a cooling rate of 80°C/min. Additional creep experiments were conducted at 815°C on the specimens which were coated with thin (1-2 μm) alumina layer at 950°C under a partial pressure of 10^{-3} Pa. The results show that the oxide layer was perfectly protective against oxygen penetration and that both the secondary creep and the rupture life were substantially improved. The mechanism for these effects has yet to be elucidated.

2.3.1.2.7 Fatigue Resistance

High cycle fatigue (HCF) behavior in alloy K5 in duplex (10 μm) and RFL (300 μm) microstructural forms was conducted on smooth hour-glass type specimens under tension-

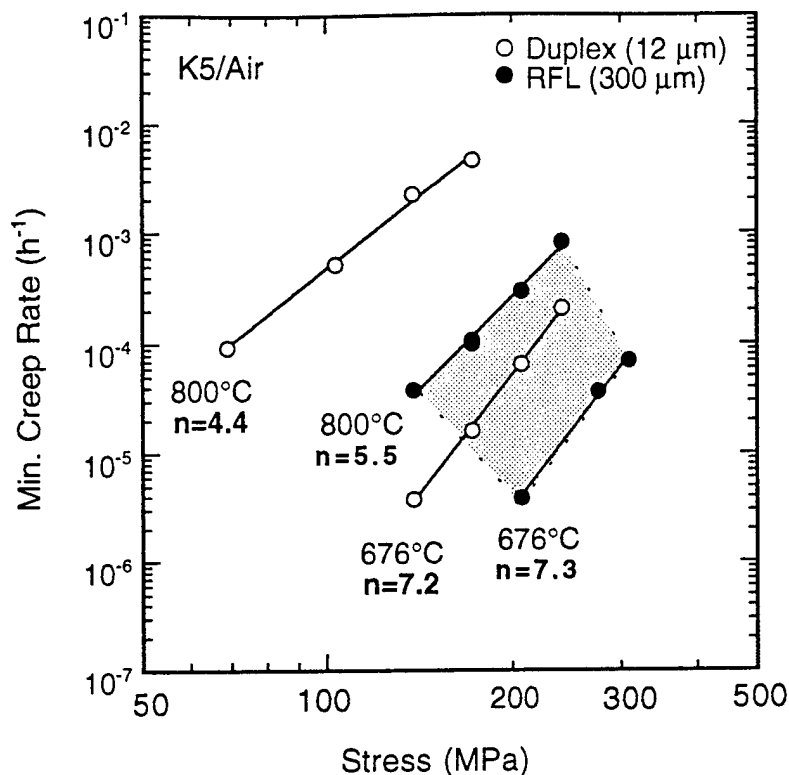
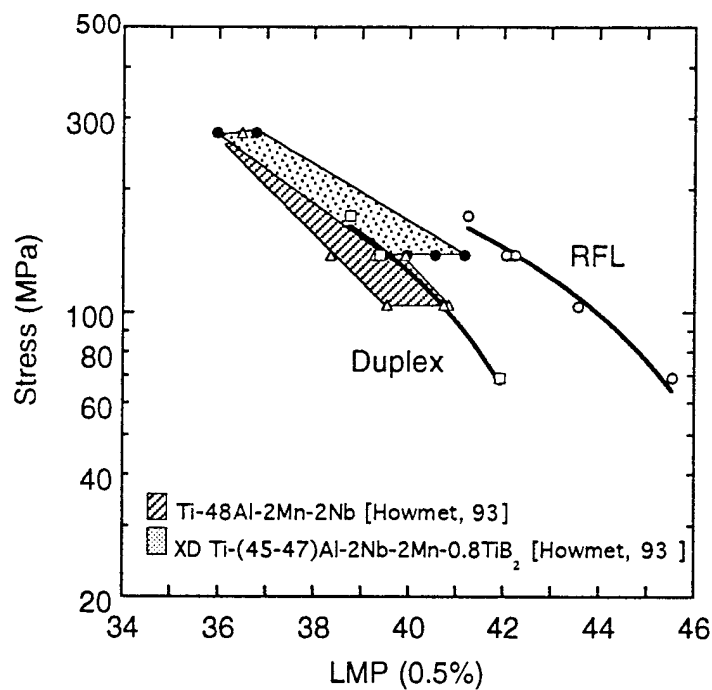


Figure 2-15. Stress Exponent (n) Values for Duplex and Refined Fully-Lamellar Materials at 676°C and 800°C.



L-M Plot of Time to 0.5% Creep Strain

Figure 2-16. Larsen-Miller Plots of Time to 0.5% Creep Strain for Alloy K5 in Duplex and RFL Microstructural Forms, as Compared to those for Two Casting Alloys.

tension loading conditions ($R=0.1$) at 600, 800, and 870°C in air. The S-N curves for all test conditions are plotted in Fig. 2-17(a) and also in Fig. 2-17(b) after normalizing the maximum stress to yield (s_{\max}/s_y). At 600°C, which is below the BDTT for both materials, the curves are fairly flat for both duplex and FL microstructures, and duplex materials exhibit higher fatigue stress at 10^7 runouts. At 800°C or higher, two-step S-N curves are observed for both materials. The first stage shows a gradual decrease up to the maximum applied stress, then reaches the yield stress ($s_{\max}=s_y$). The second begins at ($s_{\max}=s_y$), and decreases at a more rapid rate. Tensile glide is considered to be the predominant deformation mode in the first stage, while creep formation appears to become important in the second stage. At 800°C and 870°C, tensile component is retained to higher cycles in RFL than in duplex material, resulting in improved fatigue resistance for refined fully-lamellar materials. For both loading conditions at temperatures below the BDTT, the failure appears to take place by the formation of strain incompatibility induced microcracks which grow to a critical size, comparable to the grain size, leading to cleavage fracture. At high temperatures, intergranular and interlamellar fracture became predominant, although transgranular cleavage fracture was persistent in FL materials. The critical crack size for fatigue failure is related to the grain size, indicating that fine-grained FL materials are favored for enhanced fatigue resistance. Crack initiation took place in general at the specimen surfaces for duplex material and primarily in the interior but near the surface for FL materials, the latter of which is followed by a relatively slow crack growth stage. However, the relative significance of the crack growth stage in FL material with respect to fatigue lives, has yet to be investigated. Microstructural inhomogeneity appears to degrade the fatigue properties, as it does reduce tensile ductility.

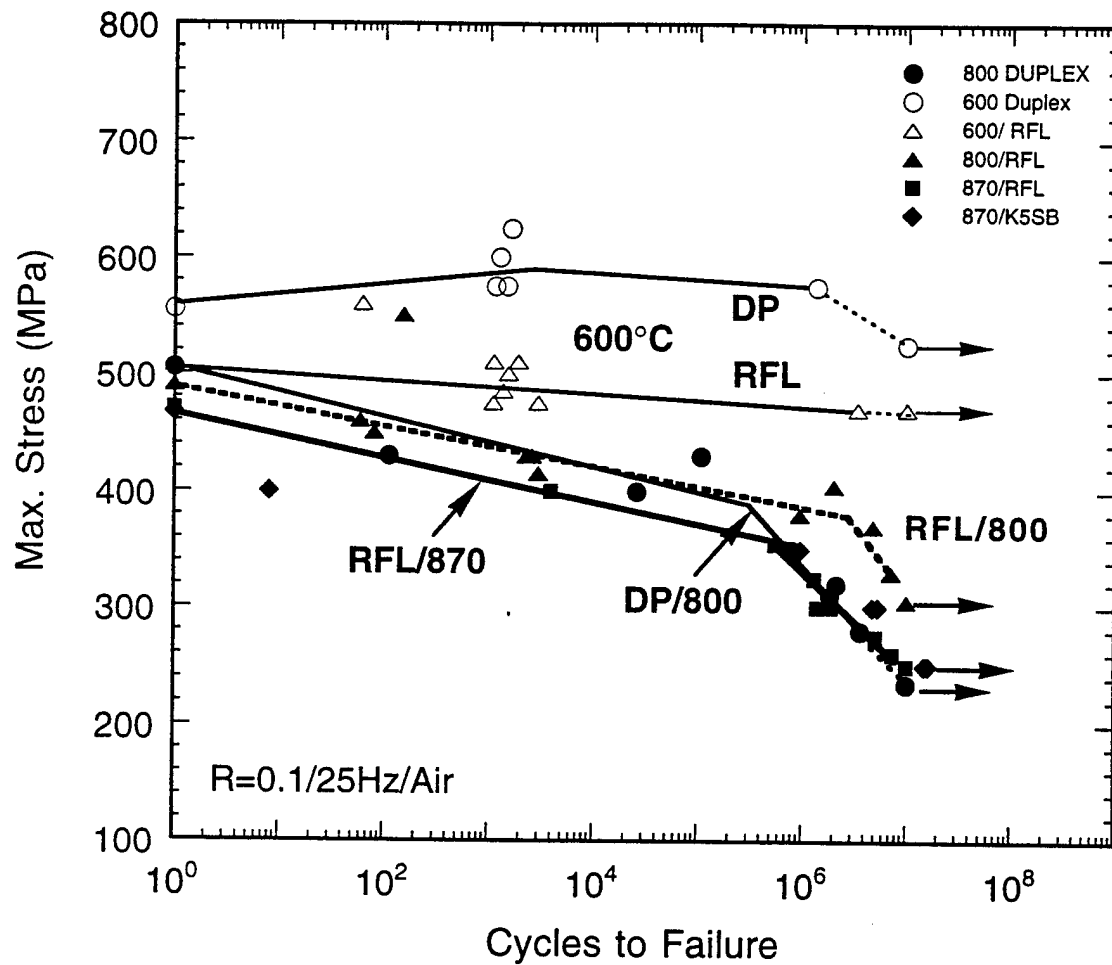


Figure 2-17(a). SN Curves for Load-Controlled HCF of Alloy K5 in Duplex and RFL Microstructural Conditions in Air at 600°C, 800°C and 870°C Measured on Smooth Hour-Glass Fatigue Specimens.

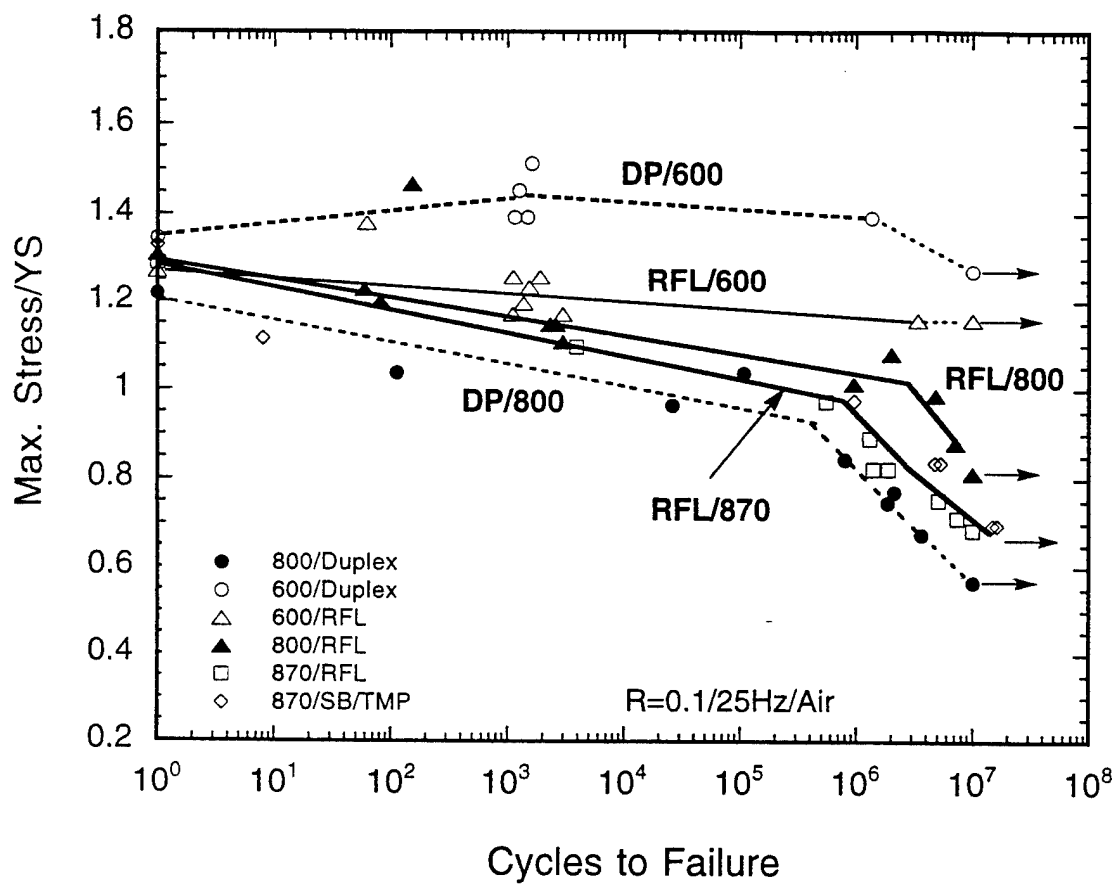


Figure 2-17(b). SN Curves with the Maximum Stress Normalized to Yield Stress.

2.4 DESIGNING MICROSTRUCTURES

2.4.1 SUMMARY OF MAJOR FINDINGS

2.4.1.1 Microstructure Optimization

Judging from the relationships between microstructure and mechanical properties described in the previous section, optimum microstructural features were derived as follows:

- Microstructure type: Fully-lamellar (FL) or lamellar structure based
- Grain size range: 50-400 μm
- Lamellar spacing (l_L): $l_{\min} < l_L < 1 \mu\text{m}$ (l_{\min} is determined by the maximum cooling rate above which the lamellar structures are disturbed or other types of microstructures are developed)
- Grain boundaries having serrated morphologies with a minimum number, or the absence, of gamma grains
- Average α_2/γ lath thickness ratio: 0.05-0.25

The exact magnitude or size of a specific feature should be component-specific and may be determined considering the property requirements, component configurations and dimensions (thickness) and processing routes selected. During the reporting period, it was recognized that such FL grain size is difficult to produce in Ti-48Al-2Cr-2Nb and alloys containing large amounts (>0.4 at.%) of boron (such as XD alloys) are not suitable as wrought alloys. Because of this, investigations were conducted to refine lamellar structures in alloy K5 and its modified versions. Fine-grained duplex or nearly-lamellar materials can also be useful if the use temperatures are relatively low and where property requirements are not fracture-critical. Certain types of microstructures are expected to improve the initiation toughness over current FL materials, by suppressing or retarding the formation of critical-size cracks. Included in such microstructures

are modified-Widmanstätten and/or modified-acicular type microstructures that may be of basket-weave type. Preliminary experiments showed that these microstructures can be produced through high-rate alpha-decomposition followed by innovative heat treatments. In addition, there are plenty of microstructures unexplored that can be generated by controlling cooling rate/scheme, heating method and processing routes. In the end, however, the material should not have microstructural nonuniformity which will lower property levels and shorten the life, especially, for fine-grained materials.

2.4.1.2 Process Development

Ingot conversion through isothermal forging, extrusion and multistep processing was experimented with and without homogenization treatments on various size work-pieces. Conditions and parameters for conversion of alloy ingots weighing up to 700 pounds were determined during the contract period, and were found to be effective, although more details have yet to be answered. Ingot breakdown by non-isothermal forging was shown to be feasible on canned work-pieces. Forging in the ($\alpha+\gamma$) phase field was successfully practiced, and now the so-called α forging is under experimentation. The development of a forging process, that can produce aligned lamellar structure in forged pancakes, has an engineering significance and is a milestone. Prototype blades having twisted air foils have been successfully forged isothermally. Forming by hot-die forging and high rate extrusion was tried with some successes, but many hurdles have to be overcome if wrought gamma components are to be produced through these processes. Recent trials of automotive valve extrusion in current production facilities, though limited to canned/insulated material, indicate that such high rate forming of gamma may eventually be technologically feasible if optimum processing conditions and parameters are identified on preconditioned material.

2.4.1.3 Microstructure Design

Three designed microstructures based on the lamellar structure were developed during the contract period, and include: thermomechanically treated lamellar (TMTL), refined-fully lamellar (RFL), and thermomechanically processed lamellar (TMPL) microstructures. The production fundamentals were formulated through combined knowledge/experience in the phase transformations, mechanisms and kinetics of microstructural evolution, and composition-processing microstructure relations, and also by the aid of process modeling. These designed microstructures were obtained in various forms. These microstructures exhibit improved high temperature strength retention with at least 50% of the RT strength levels retained at 1000°C. Both RFL and TMTL materials show reasonable RT strength levels between 450-600 MPa and the tensile elongation's in the range of 0.5-2.0%, with reasonable balances in various mechanical properties. By refining the lamellar spacing further, much higher yield strength levels are expected to be realized. Impressive improvements were observed in TMPL materials, with strength levels reaching as high as 1000 MPa at RT and more than 450 MPa at 1000°C, both with tensile elongations of about 2%. Probably, the most significant property improvements were achieved in TMPL materials produced in laboratory scale disk forms by alpha-forging experiments. Yield strength levels in the range of 650-950 MPa at RT and 450-550 MPa at 900°C in both longitudinal as well as transverse directions, were achieved. The full spectrum of mechanical properties have not yet been tested in these materials. Considerably more work has to be done in various aspects; such as understanding the formation mechanisms, thermal and mechanical stability, process control including heat treatment cycles, establishing data bases, property evaluation, and characterization of damage tolerance. By further refining the designed microstructures and with carbon additions properly aged for enhanced properties, wrought gamma alloys of engineering importance may emerge with significantly improved balances of properties and/or use temperatures increased by 50-200°C.

2.4.1.4 TMTL Microstructures

The TMTL microstructures were produced in wrought-processed alloys by adding small amounts of boron. The solubility of boron in gamma appears to be not more than 0.05 at.% in the alpha phase field temperatures. The excessive boron is present as fine lacy Ti-borides which apparently retard the growth of alpha grains during heat treatment in the alpha field. Upon cooling, alpha grains transform into lamellar grains with ragged boundaries, resulting in randomly oriented colony structures, similar to XD cast alloy microstructures. The exact mechanism for the formation of such an interlocked boundary morphology was not fully investigated. Preliminary investigations suggest that the TMT lamellar structures may form at smaller undercoolings compared to that for standard lamellar structures. The TMTL structures are produced even under air cooling without generating other types of microstructures. The colony size depends on the boron content, as shown in Fig. 2-18. The grain refinement begins to be effective when boron additions exceed 0.05 at.%, and fine TMTL grains (about 70 μm) can be obtained in Ti-47Al by the addition of 0.5 at.% B. Boron additions up to 0.5 at.% do not refine the cast microstructures. With 0.1 at.% B or higher, the grain sizes indicated in Fig. 2-18 are obtained in a very short time (order of minutes) during the alpha treatments and then they remain unchanged with further increases in annealing temperature and time. The inoculation capability of boron in wrought alloys appears to be only slightly dependent on the alloy composition. Tensile property measurements show that the strength levels of TMTL materials containing 0.2 at.% B are lower than expected, and this appears to be the tendency of boron additions increasing lamellar spacing. These adverse boron effects deserve further investigation, because adding certain amounts of boron are expected to become a standard practice for wrought alloy ingot production.

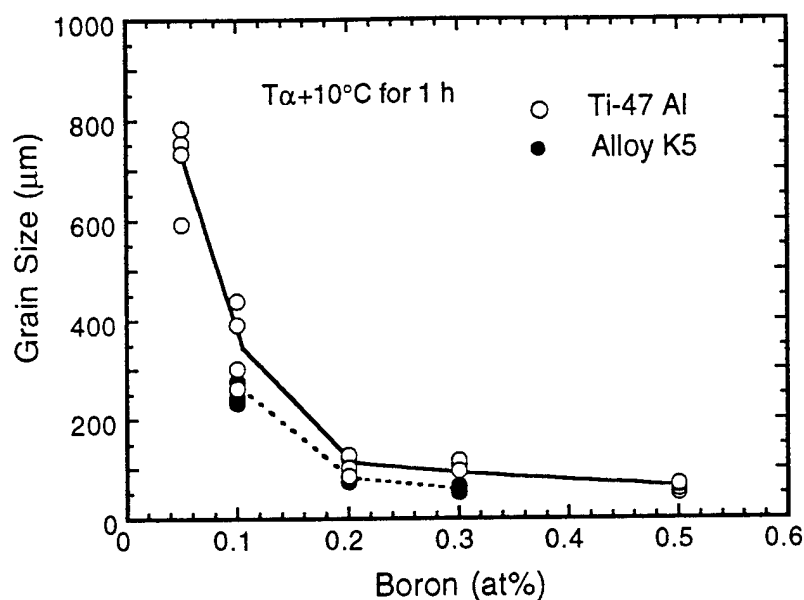
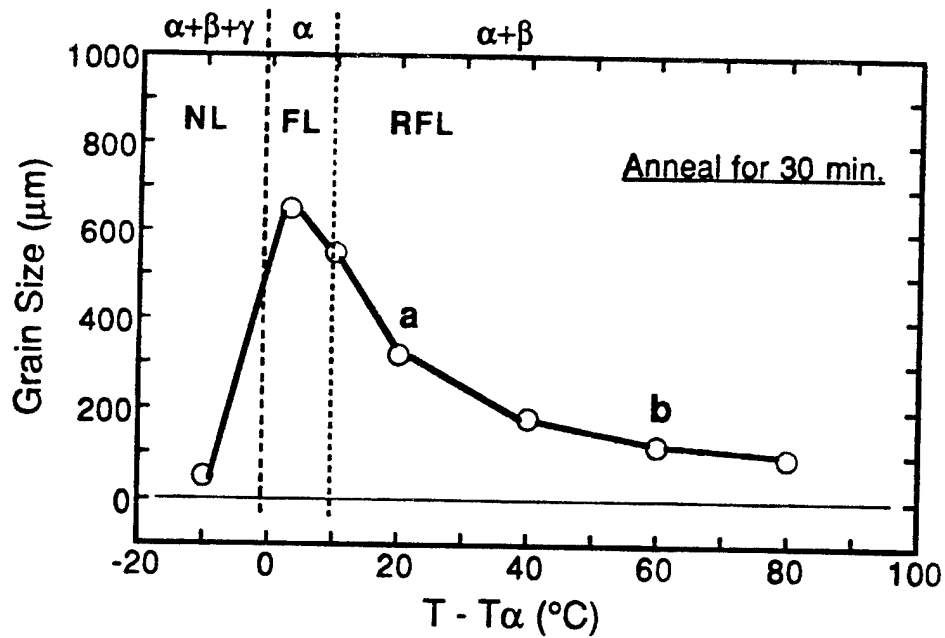


Figure 2-18. TMT Lamellar Grain Size as a Function of Boron Content in Forged Ti-47Al-xB and Ti-46.5Al-2Cr-3Nb-0.2W-xB after Alpha Treatment for One Hour.

2.4.1.5 RFL Microstructures

RFL materials are defined as refined FL materials having refined grain sizes (smaller than 400 μm) which can be produced by the standard alpha treatment followed by furnace cooling. RFL microstructures were found to be obtained through several ways, but in this program a ($\alpha+\beta$) treatment was developed using alloy K5 (Ti-46.5Al-2Cr-3Nb-0.2W). Alloy K5 has a wide ($\alpha+\beta$) field and a narrow ($DT \sim 15^\circ\text{C}$) field band, with $T_\alpha = 1320^\circ\text{C}$, $T_{\alpha+\beta} \sim 1335^\circ\text{C}$, and $T_{\alpha+\beta/\beta} > 1400^\circ\text{C}$. In the $\alpha+\beta$ field, the volume fraction of beta phase increases gradually with increasing temperature. Grain size variations upon annealing in the alloy forgings are plotted as a function of annealing temperature (with respect to T_α) in Fig. 2-19 where corresponding phase fields and microstructural features are incorporated. Clearly, the presence of the beta phase refines the grains effectively; however, the enhanced refinement appears to be associated with the enhanced formation of grain boundary gamma grains. Various mechanical properties and oxidation resistance have been extensively evaluated for alloy K5 RFL material with 300 μm grain sizes and about 0.5 μm lamellar spacing. As expected, the RFL material exhibited considerably



Lamellar Grain Size Control in Wrought Alloy K5

Figure 2-19. Variations of Microstructural Type and Grain Size with Annealing Temperature (with respect to $T_{\alpha}=1320^{\circ}\text{C}$) in Alloy K5 which has a Modified ($\alpha+\beta$) Phase Field. Two examples of RFL microstructures in forgings obtained after annealing at: (a) 1340°C for two hours and (b) 1380°C for one hour.

improved balances in mechanical properties over fine-grained duplex as well as coarse FL materials. Nevertheless, more work is needed to optimize the RFL material by identifying various fundamental aspects such as high temperature phase relations including phase boundaries and the origin and kinetics of the formation of grain boundary gamma grains.

2.4.1.6 TMPL Microstructures

TMPL microstructures are produced when gamma alloys are hot-worked at temperatures around or above T_a , and they can be fine grained, coarse grained, curved lamellar, or aligned lamellar. Fine or coarse TMPL colonies are produced when extruded at temperatures near or just above T_a and are similar to TMTL microstructures in morphology. The formation mechanisms of such fine lamellar colonies and random lamellae are not clearly known. Compressive yield stresses of these TMPL materials of various alloy compositions range from 750-850 MPa and remained fairly unchanged after aging in air at 900°C for 390 h. Further increases in strength levels appear to be possible by modifying extrusion parameters and conditions and also post-extrusion cooling rates. The extraordinarily high strength levels measured in TMPL materials are compared with those for duplex, fully-lamellar (FL), RFL and TMTL materials in Fig. 2-20. A special type of TMPL was produced when forging was conducted on canned work-pieces immediately following soaking at temperatures in the alpha phase field, under certain amounts of forging deformation and at slow forging rates. Impressive improvements were observed in TMPL materials, with strength levels reaching as high as 1000 MPa at RT and more than 450 MPa at 1000°C, both with tensile elongations of about 2%. A special type of TMPL was produced when nonisothermal forging was conducted on canned work-pieces immediately following soaking at temperatures in the alpha phase field, under certain amounts of forging deformations and at slow forging rates, Fig. 2-21. These alpha-forged microstructures, called aligned TMPL (or TMPAL), are characterized by both the grains and constituent lamellae aligned to the material flow direction. Significant property improvements were achieved in TMPAL materials produced in laboratory scale disk forms, as shown in Fig. 2-22. As shown, the yield

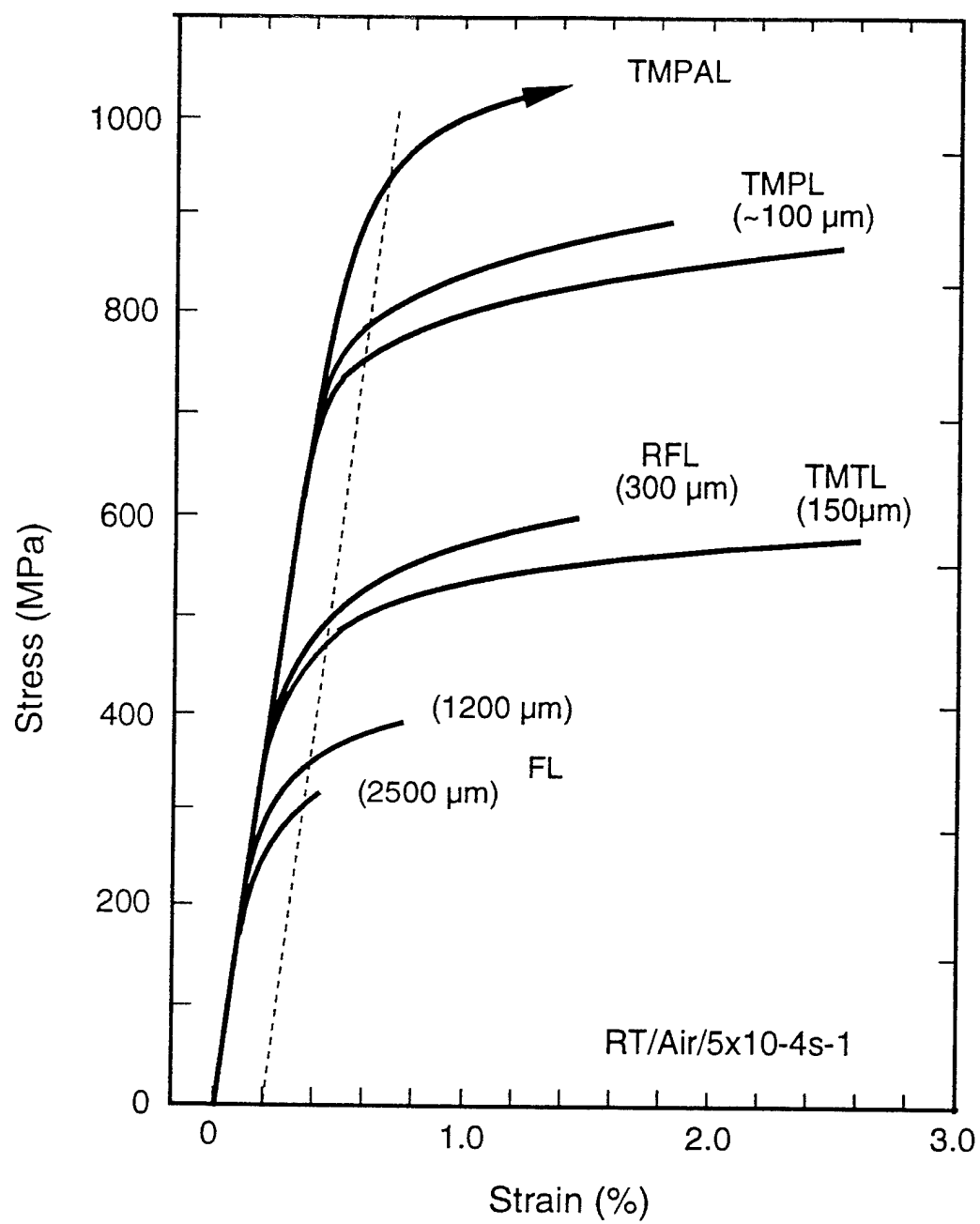


Figure 2-20. RT Flow Curves of Wrought TiAl Alloys in Various Fully-Lamellar Forms.

Alpha Forging for Aligned Lamellar Structures (TMPAL)

YWK(11/95-7/96)

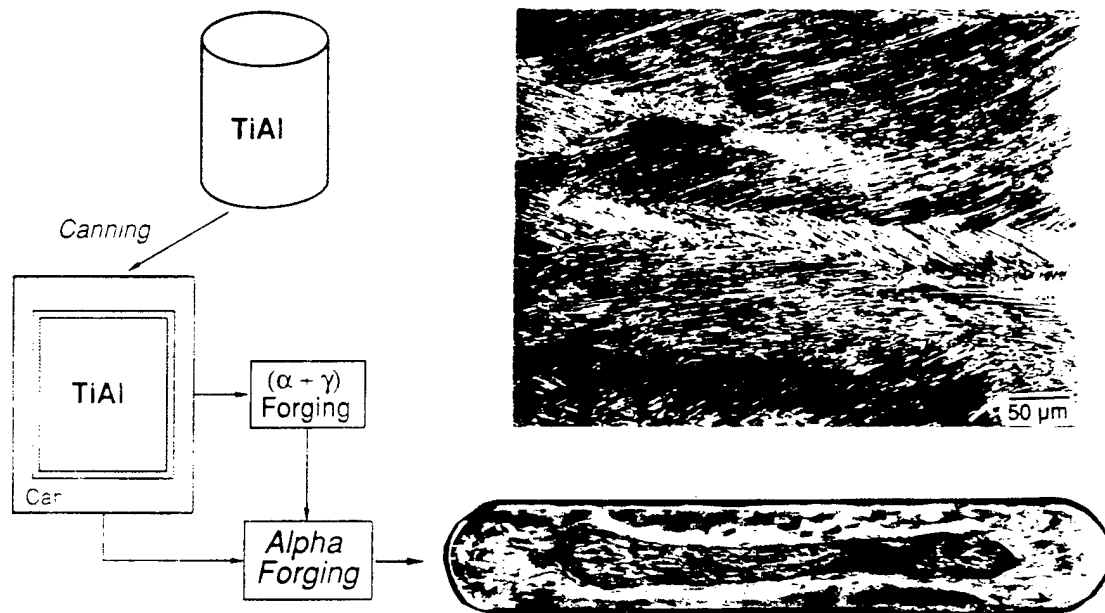


Figure 2-21. Schematic Alpha Forging Process, Cross-Sectional View of an α -Forged Plate, and the TMPAL Microstructure Consisting of Aligned Grains/Lamellae to the Material Flow Direction.

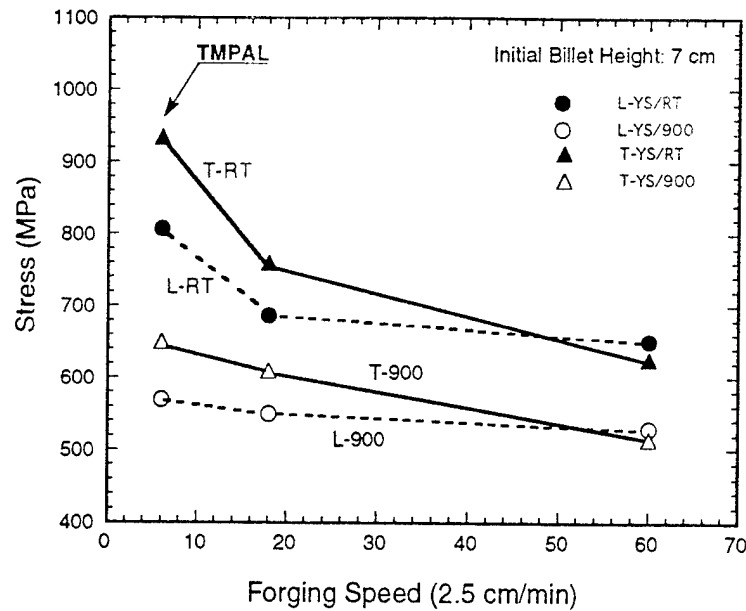


Figure 2-22. Yield Stress vs. Forging Speed and Temperature Measured in Radial (L) and Transverse (T) Directions in Alpha-Forged Pancakes.

stress is a function of forging speed, and TMPAL microstructures were produced at a forging rate of 15 cm/min with the best results. In this case, the yield strength levels were 945 MPa for transverse directions and 805 MPa for the radial direction, 650-950 MPa at RT, and 640 MPa and 570 MPa in respective directions at 900°C. Reduced yield stresses resulted as the forging rate decreased.

2.5 THEORETICAL STUDIES AND COMPUTATIONAL MATERIALS SCIENCE

2.5.1 SUMMARY OF MAJOR FINDINGS

2.5.1.1 Dependence of Strength on the Scale of the Microstructure

The Air Force has many requirements for materials which are strong at high temperatures. Great strength can best be achieved by reducing the scale of the microstructure but the strength does not increase indefinitely as the scale is reduced for a number of reasons. First, diffusive

creep mechanisms become important when the grains are small and equiaxed. Second, very fine microstructures have a large driving force for abnormal growth. Third, layered structures, which are immune to diffusive creep and stable against abnormal growth, become coherent, and, consequently, lose their strength when the layers are very thin. The theme of this work was to achieve a sufficiently exact understanding of strengthening mechanisms, grain growth and pinning, diffusive creep, and the coherent/incoherent transformation to be able to find and to exploit the conditions under which maximum strength occur. Emphasis was placed on the engineering layered materials gamma TiAl and metallic multi-layers.

2.5.1.1.1 Yield Stress of Multi-Layers

Metallic multi-layers can now be made with controlled layer thicknesses in the range of a monolayer to several microns. The finest of these multi-layers have exceptional indentation strengths and wear resistances while the coarser ones have very high strengths and some ductility. A first theory to predict the yield strength or nanohardness as a function of layer thickness and metal composition has been made by considering the components of the strength of a single interface and incorporating this into the Hall-Petch theory of yield. The contributors to interfacial strength which have been considered are: (1) the elastic mismatch (Koehler effect), (2) the lattice parameter mismatch, and (3) the dislocation core mismatch. Of these, the first and the last have been calculated atomistically and the second, which includes the effect of the mismatch dislocations and the difference dislocations left behind at an interface, has been calculated classically. The Hall-Petch theory used is a non-standard form which takes account of the very short glide paths available to dislocations in multi-layers. The resulting theory, when applied to Cu-Ni multi-layers, gives a good order-of-magnitude agreement with an experiment and reproduces the peak in the strength (1.7 GPa) observed at a layer thickness of about 10 nm. The theoretical predictions extend to layer thicknesses as small as 0.2 nm where there is no experimental data.

The above description refers to the hard-mode deformation of multi-layers, a mode in which deformation must cross the layer boundaries. By analogy with lamellar TiAl, however, it can be predicted that, in some multi-layers, there is also a soft mode of deformation in which slip occurs within the plane of the layers. In this mode, the multi-layers should lose almost all their exceptional strength. Again, there is no experimental data against which to test this prediction.

2.5.1.1.2 Yield Stress of Lamellar TiAl

In the theory of the yield strength of fully-lamellar gamma Ti-Al alloys, there are three separate Hall-Petch effects because there are three identifiable grain sizes: the lamellar thickness, the domain size within a lamella, and the lamellar colony size. The first two of these effects have been quantified satisfactorily and compared with measured values of the strength of polysynthetically twinned TiAl. The lamellar thickness influences the strength in the hard (cross lamellar) mode, the domain size influences the strength in the soft (intra lamellar) mode. In both of these modes the barrier strengths can be calculated with some confidence and the resulting yield strengths agree with the experiment to within a factor of two. Initially, the barrier strengths were calculated classically taking into account four contributions to the obstacle for a gliding dislocation: the presence of mismatch dislocations at the interfaces, caused by the tetragonality of $L1_0$, the small change in Burgers vector, also caused by tetragonality, the gross change in Burgers vector across certain interfaces caused by the crystallography of $L1_0$ and the discontinuities in the slip planes across lamellar interfaces. In some cases the classical calculations have been checked by means of atomistic simulations and these have revealed new contributions to the barrier strengths. For example, dislocations crossing a lamellar interface generally can lower their energies by dissociating in the interfacial plane. A large stress is required to reassociate the cores and hence make the dislocations mobile in the second lamella.

2.5.1.1.3 Shear Transformations in Gamma TiAl

The lamellar form of the grains in TiAl is critical to the engineering performance of the alloy. The origin of these lamellae and the mechanical properties which they confer are, therefore, of central importance. Gamma lamellae, in six variants, can form from a single alpha grain by the passage of a set of one of the six available Shockley dislocations. When a hexagonal close packed crystal, with ideal c/a ratio, is sheared by Shockley dislocations on alternate basal planes, the resulting crystal is face centered cubic. The six Shockley vectors generate cubic structures in two orientations which are twins of each other. The Shockley dislocations are the growth ledges on the interface between cubic and hexagonal grains. When the DO_{19} structure is sheared by the same six Shockley vectors, the result is three different 12H structures and their three twins. These 12H structures are composed of tetragonal unit cell building blocks, having axial ratios $1:1:\sqrt{2}$. In this description, all of the $\{100\}$ planes have alternate compositions Ti, TiAl, and the unique c axes are in six different directions, one resulting from each of the six Shockley shears. This 'tetragonal' description of the structures is the same as the tetragonal structure $L1_0$ except that in $L1_0$ the $\{100\}$ planes have alternate compositions Ti, Al. Thus, shearing the DO_{19} structure in one of the Shockley directions by $1/2\sqrt{2}$, creates a crystal structure which is as close to $L1_0$ as the composition allows. The six variants of gamma may, therefore, be formed from a single crystal of α_2 by the operation of dislocations with the six available Shockley Burgers vectors so long as the composition may be corrected by diffusion. The gamma lamellae are formed in a multiply twinned state (probably by the motion of the same Shockley dislocation backwards and forwards) but they lose the internal twins by the time they have grown to their final thickness (of the order of 1 micron). Twinning with a different morphology, this time across the thickness of the lamellae, is of major importance in plasticity because up to half the strain in TiAl is carried by twins. When a twin is blocked by a lamellar boundary, its stress field is that of a disclination dipole which has very high values of both tensile stress and shear stress ahead of the twin, in the neighboring lamella. A blocked twin is, therefore,

a potent source of crack nuclei and slip line nuclei but it is rarely a source of another twin because the crystallography generally prohibits the continuation of one twin into a neighboring lamella.

Traditional metallurgical practice is based on a semi-empirical correlation of materials properties with composition and microstructure. This theoretical effort concentrates on moving beyond a correctional understanding and focuses on developing a fundamental understanding of the processes that control specific properties of structural materials. The work includes building and using a collection of analytical and computational tools to study the properties of advanced metallics as a function of temperature and composition. Flow and fracture behavior are controlled by statistical combinations of interactions over a wide range of length scales. We have focused on the length scales covered by electronic, atomistic, and continuum methods. Where possible, the important physics from each level length scale were identified and incorporated consistently throughout the hierarchy of models.

The theory effort in the high temperature structural materials has concentrated on three critical areas. First, substructural mechanisms for enhanced strengthening in TiAl at high temperatures were studied using atomistic and first principles methods. The effects of chemistry were studied by calculating changes in dislocation core structure as a function of composition and applied stress. Second, a model of enhanced strength for layered, or nanocrystalline, materials came out of simulations of coherency strain and mismatches of elastic moduli across interface boundaries. Insights from atomistic simulations, coupled with analytical theory, produced an interface strengthening model that spans three orders of magnitude in the layer thickness. Third, the underlying substructural defects responsible for the anisotropy in strength and ductility in polysynthetically twinned TiAl were examined using available computational tools. These results raised the possibility of a super-soft mode of deformation in the soft mode and interfaces that act as strong barriers to dislocation in the hard mode. Simultaneous to these material science investigations, computational tools have been developed to further our insights to key structure-property relationships in high temperature structural materials.

2.5.1.2 Influence of Alloy Chemistry on Yield Stress

Understanding the chemical dependence of thermally activated processes, which govern plasticity in intermetallic alloys, requires that dislocation dissociation reactions be known as a function of composition. Variations in fault energies, with composition influence, dislocation core structure, and modified activation energies for cross slip, which depend on the constriction of partial dislocations, have been studied. Predicting variations in defect energy as a function of alloy composition would aid both alloy design and the interrogation of models of yield stress. A first principles method (LKRR-CPA) was used to calculate planar faults energies in γ TiAl over a range of compositions, for both the binary and ternary alloy compositions. This study included binary compositions, $\text{Ti}_{1-x}\text{Al}_x$, ranging from $0.48 \leq x \leq 0.51$, and ternary additions of Cr and Nb introduced at one and two atomic percent, giving a range of composition; $(\text{Ti}_{1-x}\text{Al}_x)_{1-y}\text{M}_y$ where $0.48 \leq x \leq 0.51$ and $0.00 \leq y \leq 0.02$. The predicted variation in planar fault energies is then used in conjunction with anisotropic theory to examine the influence of the composition on the driving forces for the cross slip of $\langle 101 \rangle$ super dislocations in TiAl. *The results of this effort suggest that: 1) changes in planar defect energies can be significant (20-50%) and 2) however, relative magnitude of the driving forces for cross slip on different glide planes remains the same as the composition changes. Therefore, alloy designers can only expect moderate improvements in the high temperature yield stress, due to the formation of $\langle 101 \rangle \{111\}$ super dislocation barriers, with changes in alloy composition.* In all cases the cross slip driving force strongly favored the formation of "roof barriers" over the formation of Kear-Wilsdorf locks, though the final energy of these two barriers can be comparable. A manuscript entitled, "Planar Fault Energies and Sessile Dislocations in Substitutionally Disordered TiAl with Nb and Cr Additions," has been published in Philosophical Magazine.

Further work on the dependence of complex stacking fault energies as a function of composition would be useful in understanding the role of ordinary dislocations and the constriction of partial dislocations associated with the $\langle 112 \rangle$ and $\langle 101 \rangle$ super dislocations.

2.5.1.3 Core Structure of Mobility of $a\langle 101 \rangle$ Super Dislocations in $L1_0$ TiAl

The low temperature (4°K - RT) yield stress of single crystals of γ -TiAl (54-56% Al) sharply increases with decreasing temperature, similar to simple BCC metals. Both the $a\langle 101 \rangle$ and $a/2\langle 112 \rangle$ super dislocations, as well as twinning, are thought to contribute significantly to the deformation process at these temperatures. The morphology of these dislocations also suggests that the Peierls stress is a strong function of line orientation. These experimental results are at variance with a classical Peierls model. Greenberg suggests that the magnitude and anisotropy of Peierls stress are related to the directional bonding prevalent in TiAl. In addition, there are numerous observations of faulted dipoles on specific line directions of $a\langle 101 \rangle$ dislocations, at both 77°K and RT, possibly as a result of their local decomposition into ordinary ($1/2\langle 110 \rangle$) and $1/2\langle 112 \rangle$ super dislocations. To gain insight into the deformation process, an empirical embedded atom method (EAM) potential, fit to the structural and elastic properties of $L1_0$ TiAl, has been used to simulate atomistically the mobility of two possible planar forms of $a\langle 101 \rangle$ dislocations in a model $L1_0$ compound. The two configurations examined were: SISF-APB-CSF coupled (P core) and the decomposed $1/2\langle 110 \rangle$ -SISF-SESF coupled form (D core). Six different line orientations of $a\langle 101 \rangle$ dislocations in the 'P' form have been considered. The core structure of all six line orientations is found to be planar and essentially confined to a single octahedral plane. However, the mobility of $a\langle 101 \rangle$ dislocations in the P form is found to be a function of line orientation, with the close packed line directions $\langle 101 \rangle$ (screw) and $\langle 110 \rangle$ (60°) having low mobility. Simulation results suggest that in a $L1_0$ structure, the mobility of $a\langle 101 \rangle$ dislocations can be low for specific close packed line directions even though their core structure is planar and the stoichiometry of the line direction ($\langle 110 \rangle$ vs. $\langle 011 \rangle$), exerts significant influence on the mobility, even without any directional interactions in the interatomic potential. The mobility of $a\langle 101 \rangle$ dislocations is consistently higher than that of $a/2\langle 110 \rangle$ (ordinary) dislocations, presumably as a result of their larger core spreading in the CSF region. Simulations of the interaction of glide stresses with the D core for the 60° (line direction, $\langle 110 \rangle$) and 120° (line

direction, $\langle 011 \rangle$) orientations show that the Shockley partials trailing the SESF in the D core are strongly pinned, and the dislocation moves by extension of SESF when stresses are applied with SESF as the trailing fault. These results have been published in a manuscript entitled "Core structure and mobility of $a\langle 101 \rangle$ dislocations in $L1_0$ TiAl".

2.5.1.4 Simulations of $1/2\langle 110 \rangle$ Dislocation in γ -TiAl

The results of the 2-D simulations of ordinary dislocations in γ -TiAl were summarized in a manuscript entitled, "Atomistic Simulations of Structures and Properties of $1/2\langle 110 \rangle$ Dislocations Using Three Different Embedded Atom Method Potentials Fit to γ -TiAl" and has been accepted for publication in Philosophical Magazine A.

Some 3-D simulations have been performed. In previous work, the structure and properties of the 'half kink,' in which the screw dislocation originates on an Al-position and terminates on a Ti-position had been simulated. This work was extended to the 'full kink,' in which the screw dislocation originates and terminates on the Ti-centered positions. The full kink was found to be spread out over a distance of ~ 5.0 nm and the friction stress was found to be less than 0.001μ , where μ is the shear modulus.

2.5.1.5 Nanostructured Layers

Experimental results show that a nanolayered composite structure made of two kinds of metallic materials strengthens dramatically as the layer thickness is reduced. This strengthening has been attributed, in epitaxial systems, to the modulus and lattice parameter mismatches between adjacent layers, using continuum mechanics calculations. However, these calculations suffer from the drawback that elasticity theory is being used for short range dislocation interactions. A parametric approach, using the embedded atom method (EAM), has been developed, to study dislocation-interface interactions in metallic nanolayers atomistically. The

aim is to elucidate the nature of the barrier which a dislocation has to overcome as it crosses a bimetallic interface, and understand the relative importance of 'lattice parameter', 'modulus' as well as 'chemical or fault energy' mismatches on the strengthening process. The results of these simulations in a model Cu-Ni system suggest that strengthening due to 'modulus mismatch', 'coherency stresses', and 'chemical mismatch' is significant in these multi-layered materials. The 'Koehler strengthening' is found to be of the order of $10^{-2} m$. Also, the atomistic simulation results on 'Koehler Strengthening' are in fair agreement with continuum calculations. However, a fairly minimal stacking fault energy mismatch of 19 mJ/m^2 across the Cu-Ni interface leads to an interface barrier of $\sim 0.002 m$, where m is the shear modulus. This indicates that 'chemical' mismatch effects lead to significant strengthening in metallic multi-layers.

Significant compositional gradient at the Cu-Ni interface is found to have very little effect on 'Koehler Strengthening'. The presence of multiple interfaces separated from each other by approximately the core width of the gliding dislocation is also found to have very little effect on 'Koehler Strengthening'. However, the presence of more than one dislocation at the Cu-Ni interface (mini-pile up) is found to significantly decrease the interface barrier for the gliding dislocation, almost in accordance with continuum calculations.

The major effect of coherency stresses is to modify the dislocation core significantly through Escaig type stresses, resulting in a change in the effective 'chemical' force as the glide dislocation crosses the Cu-Ni interface. The contribution from such a chemical force on the stresses required to cross the Cu-Ni interface has been found to be of the order of 'Koehler' effect. 3-D atomistic simulations of the structure of misfit dislocations at a (001) Cu-Ni interface and their interaction with glide dislocations have been performed. It is found that a square array of misfit dislocations spontaneously form at the interface if an initial vernier corresponding to the ideal lattice parameters of Cu and Ni are introduced at the interface. The structure of the edge misfit dislocations thus formed have been found to be non-planar, and similar to the classical description of the structure of a Lomer-Cottrell barrier. Qualitatively, the interaction between

glide and a square array of misfit dislocations have been found to be much more complicated than what is envisaged in a simple continuum description of the interaction process. The glide dislocations intersect the non-planar core of at least one misfit dislocation as it crosses the interface, which results in a significant modification of the core structure of the gliding dislocation at the intersecting region.

Another kind of interface has been considered for dislocation-interface interactions in Cu-Ni: a twinned (111) interface between Cu and Ni as well as Cu-Cu. Atomistic studies show that at both these interfaces, Cu-twinned Cu and Cu-twinned Ni, a gliding screw dislocation in the hard mode in Cu cross slips on to the Cu-Cu or the Cu-Ni twin interface at stresses of the order of 0.02 m. However, a gliding 60° dislocation in the hard mode defeats the twinned interface and cross slips on to the corresponding twinned (111) plane on the other side in the Cu-twin Cu study. For the Cu-Cu twinned interface, the stresses at which the 60° dislocation defeats the interface lies between 0.03-0.035 m. For the Cu-Ni twinned interface, the corresponding stresses lie between 0.05-0.06 m. However, in this case, the 60° dislocation moves on to the cube plane on the twinned Ni side, which is almost continuous with respect to the (111) octahedral plane in Cu. The atomistic potentials used in these studies are such that there is no lattice parameter mismatch between Cu and Ni, therefore, coherency stresses and misfit dislocations are absent at the Cu-Ni twinned interface. However, the Koehler effect still remains in the Cu-Ni study because of the different elastic constants in Ni as compared to Cu. The results from these studies show that a twinned interface in the Cu-Ni system has a strength of 0.03-0.035 m and this strength is additive to the Koehler effect.

Some of the results of the atomistic simulation studies on the strength of the interface barrier to gliding dislocations have been incorporated into an analytical (crystallographic and continuum) model for predicting yield stress as a function of wavelength for Cu-Ni multi-layers.

2.5.1.6 Coherent (111)TiAl:TiAl Interfaces

Recent experimental results on polysynthetically twinned alloys, alloys with a large volume fraction of TiAl/TiAl, and Ti₃Al/TiAl interfaces, show a large anisotropy in ductility and yield stress. The ease of twinning in these lamellae materials and the dynamics of glide along any interface is thought to influence the flow behavior of these materials. In this work the symmetry of the possible (111)TiAl/TiAl interfaces and the underlying coincident lattice (0-lattice) was evaluated. The corresponding lattice of coincident sites that produce the same 0-lattice (the \bar{b} -lattice) have the same energy, i.e.; they are degenerate. Using the symmetry of the 60° interface, we find a \bar{b} -lattice which includes the possible partial dislocation burgers vectors for (111) glide in bulk TiAl. *Therefore, these displacements on the 60° interface are degenerate. This result is independent of c/a ratio.* Similarly, the degeneracy is split into two energy levels for the 120° and 180° interfaces. These degeneracies make the elastic energies of ordinary and super dislocations on these interface planes much lower than in the bulk material. These data suggest that dislocations would glide preferentially on the γ/γ interfaces, and that dislocations intersecting these interfaces will cross-slip onto the γ/γ glide plane. These predictions have been confirmed using atomistic simulations. These results have been published in a manuscript entitled, "The Interaction Between Dislocations and Lamellar Grain Boundaries in PST γ TiAl".

2.5.1.7 Interaction of $a/2\langle 110 \rangle$ Ordinary Dislocations with γ/γ Interfaces

PST crystals are known to have unusual mechanical properties including very high ductility. It is believed that one of the contributing factors toward this unusual mechanical behavior could be the different types of γ/γ interfaces prevalent in PST crystals acting as easy channels for dislocation motion. We have simulated the motion of $a/2\langle 110 \rangle$ ordinary dislocations with the screw orientation at ideal 60° and 120° interfaces. A N-body EAM potential fit to the structural and elastic properties of L1₀ TiAl with a c/a ratio of one was used in the simulations.

It was found that the CSF energy at both the 60° and 120° interfaces were significantly lower (0 and 60 mJ/m^2), compared to the bulk, where the potential gives a value of 220 mJ/m^2 . As a result, at the 60° interface, the ordinary dislocation is present as two non-interacting Shockley partials. The mobility of ordinary dislocations is found to be significantly higher at both the 60° and 120° interfaces, as compared to the bulk. Also, both one and two atomic step ledges, at the 120° interface plane were found to be insignificant barriers to the motion of $a/2\langle 110 \rangle$ ordinary screw dislocations. However, a 60° dislocation, with Burger's vector $a/2[110]$, gliding on the interface plane was effectively blocked by a single atomic ledge at the interface.

It was also found that $a/2\langle 110 \rangle$ screw dislocations moving in the bulk on a cross slip octahedral plane cross slipped on to the interface plane as they intersect the 120° interface. However, a 60° dislocation, with Burger's vector $a/2[110]$, interacting with a 120° interface, required stresses of the order of $0.0275\text{--}0.03 \text{ m}$, to partially defeat the interface. Crystallographically, for the $a/2[110]$ 60° dislocation to defeat the 120° interface, has to drag an APB fault as it moves. However, even at stresses of 0.04 m , the trailing partial is stuck at the interface, with the leading partial moving onto the other side of the interface forming a stacking fault in between. These results have been published in a manuscript entitled, "The Interaction Between Dislocations and Lamellar Grain Boundaries in PST γ TiAl".

2.5.1.8 Green's Function Flexible Boundary Conditions

Two-dimensional (2-D) atomistic calculations of the core structure and mobilities of dislocations do not always capture the dynamic events occurring on dislocation lines which are often crucial in determining the macroscopic mechanical behavior of crystals. In order to determine activation parameters and mobilities for processes like kink pair formation, cross slip and climb of extended dislocations, there is a need for three-dimensional (3-D) atomistic calculations of dislocation activation processes. The use of fixed boundary conditions in such simulations may preclude the calculation of accurate formation energies and mobilities of the

defect complexes involved in such processes, for a given interatomic potential. To relieve the incompatibilities that arise at the boundary of these 3-D dislocation simulations, we have developed flexible boundary conditions using the Green's function technique. Subroutines to calculate the elastic response of a perfect lattice to a line as well as a point force (Elastic Green's function in 2-D and 3-D) as well as simple numerical techniques for the calculation of the response of a lattice to line, point forces and displacements (Lattice Green's function, force constant matrix in 2-D and 3-D) have been developed. This technique in combination with a conjugate gradient technique (empirical EAM potentials) has been tested successfully for both 2- and 3- D dislocation problems in simple metals (FCC Ni and BCC Fe) as well as alloys (L1₀ TiAl and B2 NiAl). In 3-D, the Green's function technique has been developed and tested for simulations involving both fixed and periodic boundary conditions along the dislocation line. The Green's function technique along with EAM potentials are now being used to study the structure and mobilities of kinks, kink pairs in B2 NiAl. Also, Green's function boundary conditions are now being implemented with MGPT potentials for Mo in an effort to study the core structure and mobilities of rigid $a/2[111]$ screw dislocations as well as kinks on such dislocations.

2.6 SUMMARY OF CURRENT WORK NOT REPORTED

The baseline experiments were conducted on alloys with more than 5 at.% Cr and 5 at.% Al. The phase equilibria data seemed to indicate that the solidification paths and microstructures are very sensitive to the Cr and Al concentrations. High concentrations of Cr and Al appeared to make the beta phase continuous, which is not a desirable microstructure for high-temperature properties. Two alloys were melted with lower Cr and Al contents to see if the silicide phase can be made continuous. The alloys had compositions of 45Nb-28Ti-5Cr-4Al-18Si and 46Nb-28Ti-5Cr-2Al-19Si. These alloys showed nearly desirable microstructures with 45-50% volume fraction of the beta phase.

A systematic study was initiated to study the effect of Hf, Cr, Al, Si content and Nb/Ti ratio on a GE alloy with composition 47Nb-25Ti-8Hf-2Cr-2Al-16Si, particularly with respect to element partitioning and the morphology and distribution of the beta and the silicide phases. These alloys had 0-8% Hf, 2-10% Cr, 2-10% Al, 13-19% Si, and 1.4-2.4 Nb/Ti ratio. The results are summarized in Table 2-4. Based on comparisons with the GE alloy, the results indicate that optimum compositions should have higher Nb, lower Ti, higher Hf, lower Cr, and lower Al than the alloys currently under investigation. These results will be used for selection of one or more alloy compositions for ingot melting and extrusion for scale-up property studies.

In a parallel study, the effect of Ta, W and Mo additions on phase stability of alloys with two different Si additions (~14 and ~21Si) were studied after heat-treatment at 1000 and 1400°C. The Mo-containing alloy showed the formation of the (Nb,Ti)₃Al phase within beta at both 1000 and 1400°C, while the Ta- and W-containing alloys showed no decomposition of the beta phase.

A preliminary study to evaluate oxidation-protective coatings was initiated in collaboration with Mel Jackson and Ann Ritter of General Electric Corporate R&D. Cylindrical pins of 150 mil diameter were machined from a cast + heat-treated Nb-Ti-Cr-Al-Si alloy and sent to GE. Two different oxidation protection coatings were deposited by a slurry process. The coating compositions were as follows: (A) 44Si-29Fe-27Cr and (B) 47Si-23Fe-19Nb-9Ti-2Cr. The coated specimens were tested under cyclic oxidation conditions at 1200 and 1400°C. At each temperature, weight changes were monitored by taking the specimens out of the furnace every hour; this process was continued until the coatings failed catastrophically. Coating A survived ~50 h at 1200°C with a weight gain of 10 mg/cm², followed by extensive spallation beyond 50 h, while coating B survived 200 hours with a net weight gain of 17 mg/cm². At 1400°C, coating A survived 3 hours, while coating B survived 21 hours followed by catastrophic failure. The results are plotted in Fig. 2-23.

Table 2-4. Effect of Alloying Modifications to the GE Alloy on Microstructures and Phase Equilibria.

Alloy	Composition of the phases at T = 1400°C			Comments
	Beta	Nb ₅ Si ₃ -Base	Ti ₅ Si ₃ -Base	
GE-6 (Nb/Ti = 1.88) 47Nb-25Ti-8Hf-2Cr-2Al-16Si	64Nb-27Ti-4Hf-3Cr-2Al-≤1Si	32Nb-18Ti-11Hf-3Cr-1Al-38Si	23Nb-23Ti-14Hf-3Cr-1Al-39Si	Large beta particles surrounded by silicide grains. Large, elongated blocky Nb-silicides.
GE-6 without Hf 52Nb-28Ti-0Hf-2Cr-2Al-16Si	59Nb-31Ti-0Hf-4Cr-5Al-1Si	41Nb-22Ti-0Hf-1Cr-1Al-36Si	29Nb-33Ti-0Hf-5Cr-2Al-35Si	Large dendritic 3:1 silicides (51Nb-23Ti-0Hf-3Cr-1Al-25Si). Can be viewed as matrix with discontinuous beta. 3:1 silicide undergoing cellular decomposition to beta & Ti-silicide.
GE-6 + high Cr (2->10) 42Nb-22Ti-8Hf-10Cr-2Al-16Si	57Nb-25Ti-3Hf-11Cr-3Al-≤1Si	31Nb-17Ti-11Hf-1Cr-1Al-38Si	not detected	Vol. fr. β same as GE-6, but β is continuous. Confirms earlier obs. that Cr makes β more continuous. Trace Cr ₂ Nb present.
GE-6 + high Al (2->10) 47Nb-25Ti-8Hf-2Cr-10Al-16Si	56Nb-24Ti-3Hf-3Cr-13Al-≤1Si	33Nb-17Ti-11Hf-3Cr-4Al-35Si	not detected	Microstructurally similar to hi Cr alloy. Vol. fr. β appears to be lower than hi Cr alloy.
GE-6 + low Si (16->13) 49Nb-26Ti-8Hf-2Cr-2Al-13Si	62Nb-28Ti-4Hf-3Cr-2Al-≤1Si	24Nb-23Ti-13Hf-3Cr-1Al-39Si	21Nb-23Ti-15Hf-3Cr-1Al-39Si	High vol. fr. β. β is continuous phase. Absence of large, block silicides. Silicides more finely and evenly distributed.
GE-6 + hi Si (16->19) 45Nb-24Ti-8Hf-2Cr-2Al-19Si	64Nb-27Ti-3Hf-3Cr-2Al-≤1Si	33Nb-19Ti-11Hf-3Cr-1Al-36Si	25Nb-23Ti-14Hf-3Cr-1Al-37Si	Although silicide has high volume fraction, beta is still continuous.
GE-6 + low Nb/Ti (1.4) 42Nb-30Ti-8Hf-2Cr-2Al-16Si	57Nb-33Ti-4Hf-3Cr-2Al-≤1Si	28Nb-21Ti-11Hf-3Cr-1Al-38Si	22Nb-27Ti-11Hf-3Cr-1Al-38Si	Continuous beta. Not at all a desirable microstructure.
GE-6 + hi Nb/Ti (2.4) 51Nb-21Ti-8Hf-2Cr-2Al-16Si	68Nb-22Ti-4Hf-3Cr-2Al-≤1Si	27Nb-20Ti-13Hf-4Cr-1Al-38Si	not detected	Continuous beta, but more linking of silicide phase. Fewer blocky silicides.

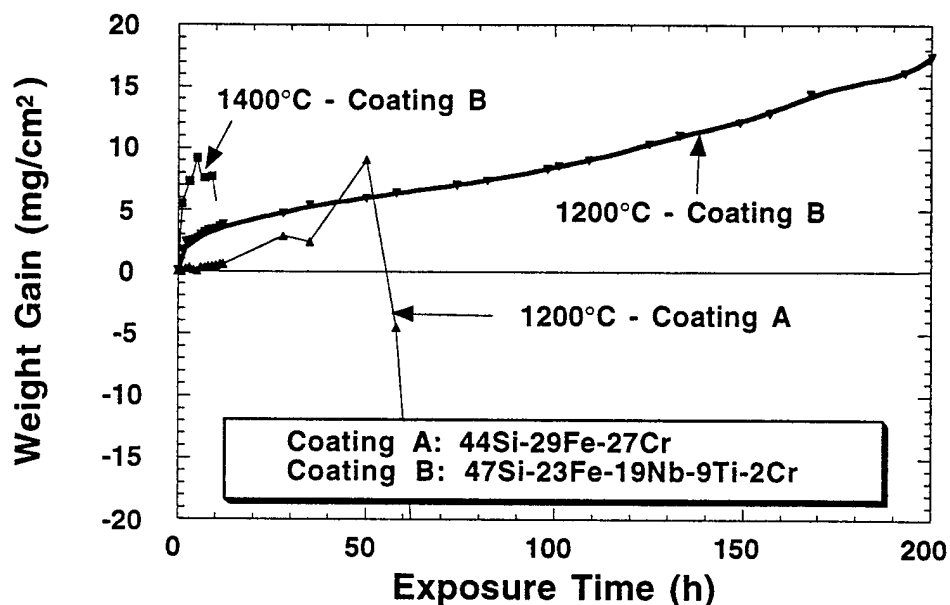


Figure 2-23. Weight Gain Data for Coated Nb-Ti-Cr-Al-Si Alloys after Cycle Oxidation Testing at 1200 and 1400°C.

A patent disclosure entitled, "Niobium-Titanium-Chromium-Aluminum-Silicon Alloys for High Temperature Applications," has been submitted to the Air Force Patents Office as Air Force Invention No. D00060.

2.6.1 COHERENCE STRESSES IN MULTI-LAYERS

The formulae given by Grinfeld for the stresses and strains in a multi-layer are being tested in special cases to check their validity and interpreted to determine their physical meaning. For example, in a PST specimen containing only gamma lamellae, the formulae predict that, when coherent, the lattice parameter in any direction is the weighted mean of the lattice parameters in the same directions of the individual lamellae. In a PST specimen containing gamma and alpha lamellae a similar result is true, but the biaxial moduli of the gamma and alpha phases appear in the weighting factors.

The Grinfeld formula for the coherency stresses in any layer of a multi-layer is correct for very thin layers. For thicker layers the energy of the multi-layer can be reduced by the formation of mismatch dislocations or corrugations at the layer interfaces. The theory for this coherency limit has been worked out for single interfaces. We are now applying this theory to multi-layers.

The coherency stresses can be resolved onto the slip planes of coherent multi-layers. In the hard mode the slip planes will be divided into strips within each of which there is a calculable coherency stress. We are using these results (and the results of Barnett on the energy factors of dislocations in materials having layers with different moduli) to simulate the operation of a dislocation source in one of the strips, to calculate the applied stress required to make the source multiply and to find how much extra stress is needed for the dislocation to overcome the first interfacial barrier. This simulation, based on the Brown-Orlov theorem, will give us, for the first time, values of the yield stress in a fully coherent multi-layer.

2.6.2 HALL-PETCH STRENGTHENING AND STROH THEORY FOR TWINNING

There is increasing experimental evidence that, at high temperatures and after large strains, twinning becomes the most important strain mechanism in TiAl. The Shockley dislocations which form the twins accumulate at barriers either in the form of regular pile ups or in the form of walls. In the former case, the theories of slip propagation or of fracture nucleation are similar to the theories for glide dislocations but in the latter (Muellner) case the dislocations have the stress field of a disclination dipole. This stress field is completely different from that of a pile up and has glide and tensile stresses which have different magnitudes and different directions from a pile up stress field. For example, the maximum tensile stress is very large and appears on the plane of the dislocation wall when the dislocations are edges. It is on this plane that fracture would be expected to nucleate. In TiAl this would appear as delamination fracture. The glide stress from a disclination dipole has a very large maximum value which is independent of the number of

dislocations in the wall. The Hall-Petch strengthening from twinning is, therefore, expected to be very different from regular Hall-Petch strengthening and will not have the characteristic $d^{-1/2}$ dependence on grain size. The theory for both Stroh fracture nucleation and Hall-Petch strengthening, and the competition between these two, is being calculated.

2.6.3 YIELD STRESS OF FULLY-LAMELLAR TiAl

In any material the three parameters in the Hall-Petch equation to be calculated are: (1) the stress to propagate a dislocation in a large grain, (2) the barrier strengths, and (3) the Taylor factors. In fully-lamellar TiAl, the calculations are complicated by the fact that each grain is subdivided into lamellae and domains. Furthermore, the scale of the lamellar structure appears to be linked to the grain size. The strength of fully-lamellar TiAl is, therefore, determined not only by the intrinsic strength of TiAl and the grain structure, but also by the properties of a single lamellar (PST) grain. Current work being undertaken to quantify the parameters in the Hall-Petch equation for fully-lamellar TiAl is: (1) the Viguier-Louchet model for the stress to move a $\langle 110 \rangle / 2$ unit dislocation can definitely be improved and probably replaced by a 'single dislocation' model. Such a model, based on Seshagiri's and Sun's observations and taking account of the spectrum of obstacles (caused by multiple cross slip) along a dislocation, is being developed. (2) Estimates of the barrier strengths of lamellar and domain boundaries, which are currently made classically in terms of difference dislocations, discontinuities in the slip planes, discontinuities in elastic modulus, discontinuities in burgers vectors, will continue to be replaced by computer simulation calculations. (3) A calculation will be made of the Taylor factor for the fully-lamellar grains. The calculation is analogous to the Tome calculation for zirconium alloys in the sense that there is a unique basal slip plane and a multitude of harder slip planes inclined to the basal plane.

2.6.4 STABILITY OF NANOCRYSTALLINE GRAIN STRUCTURES

In a material containing a matrix with a dispersion of particles, grain growth may stagnate when the grain boundaries are pinned by interaction with the particles. In the classical Zener theory, the stagnant grain size is proportional to the particle size and inversely proportional to the volume fraction of particles. However, computer simulations of stagnating grain growth give a different result. The particle size dependence is not determined and the grain size is inversely proportional to the one third power of the volume fraction of particles. This difference between the classical and numerical predictions was not resolved by the computer simulations carried out in the 1980s, either because the simulations were too small or because the shapes of the particles were not accurately simulated.

We have begun a new series of Monte Carlo simulations of grain growth and stagnation in which attention is focused on optimizing the speed of computation and the size of the simulation. In addition, realistically shaped particles with either spherical or plate or needle forms in a variety of spatial orientations are used in the simulations. Such simulations allow, for the first time, the grain size to be determined as functions of particle size, particle shape, and particle volume fraction.

The first results from the program show that particle shape does not affect the shape of the pinned grains as much as had been expected from classical theory. Particle size also influences the grain structure in an unexpected way: Instead of the grain size being linear in the particle size, the variation is much slower than linear.

2.6.5 DIRECT VERSUS INDIRECT HARDENING OF NANOCRYSTALLINE MATERIALS

Nanocrystalline materials which deform by a dislocation mechanism often contain dispersions of a second phase which are required to prevent the grains from growing out of the

nanocrystalline range (for example, cryomilled Al alloys). In such polycrystals, consisting of a matrix and a uniform dispersion of particles or bubbles with a grain size determined by critical Zener pinning, the yield stress is controlled not so much by direct particle-dislocation interactions as by indirect particle-grain boundary-dislocation interactions. The particles pin the grain boundaries and the grain boundaries obstruct the dislocations. After yield, dislocations accumulate in the matrix, at hard particles (but not at bubbles) and at grain boundaries. These accumulations cause work-hardening. In the case of hard particles, the particle (direct) work-hardening and the grain boundary (indirect) work hardening are equal. This is because the migration distance of a grain boundary through a dispersion of particles is the same as the glide distance of a dislocation through the same dispersion. In the case of bubbles the direct work hardening is zero because dislocations cannot accumulate at bubbles. At low strains, therefore, indirect hardening dominates the flow stress. Only at high strains can the matrix work-hardening be significant. In strong alloys, those with a high volume fraction of small particles, the matrix work-hardening is never significant and so the flow stress in these alloys is always controlled by indirect hardening.

The theory outlined above makes the firm prediction that the best way to obstruct dislocations, and, therefore, to increase the strength, is to use the particles to refine the grain size rather than to block the dislocations directly. However, the theory is somewhat idealized. Experiments on cryomilled nanocrystalline Al alloys, containing high volume fractions of oxide, provide a good opportunity to test out the theory to determine which parts of it are adequate and which parts need improvement.

2.6.6 COBLE CREEP IN NANOCRYSTALLINE MATERIALS

In the Hall-Petch theory for the yield stress in fine grained materials, the graph of yield stress versus $d^{-1/2}$ is linear at larger grain size, becomes increasingly stepped (but retains roughly the same average slope) as the number of dislocations falls and then changes to a parabola (d^{-1}

behavior) when single dislocations are traveling. The overall effect is that the $d^{-1/2}$ line is a good approximation down to grain sizes of ~ 100 nm, depending on the strength of the grain boundary in the particular material. The strength rises without limit as the grains are refined.

However, nanometer sized grains do have alternative deformation modes, for example Coble creep. For this process the stress is proportional to d^3 and, consequently, falls very rapidly as the grain size is reduced. This fall, combined with the Hall-Petch rise, gives a very sharp peak in the yield stress at a grain size in the range 10 nm-100 nm.

In real metals the sharpness of the peak is blunted by three effects. First, grains are not all the same size, so some can deform by Coble creep, while others are deforming by a dislocation process. A related effect is that in large grains the centers can deform by glide, while the outsides are undergoing Coble creep. The third effect is that each grain boundary has a different strength. The distribution in grain boundary strengths effectively widens the grain size distribution. In our theory, we assume a log-normal distribution of grain sizes with a σ value of ~ 2 .

When the theory is compared to experiments in Cu and Cu-void alloys, the agreement can be made very close when all the parameters are given plausible values. The most pleasing aspect of the fit is that the distribution of grain sizes completely changes the d^3 variation of yield stress to a form more nearly proportional to d , which is in good agreement with the experiment.

In order to fit the experimental values of yield stress, it is necessary to oppose Coble creep with a large (several hundred MPa) threshold stress. Experimentally this stress is known to be proportional to d^{-1} , which could be caused by the surface tension of the grains or else by the line tension of the dislocations which are sources and sinks of vacancies on the grain boundaries. We are currently investigating whether there might be a third possible explanation for the d^{-1} form of the threshold stress, namely that it is intrinsic to the Coble creep. To test this hypothesis we are calculating the rate of Coble creep *ab initio* in a grain structure with cuboid

grains. After many attempts the partial differential equations have not yet been solved and it may be necessary to solve the problem numerically.

2.6.7 CROSS SLIP OF $a/2[110]$ SCREW DISLOCATIONS IN FCC Ni

Cross slip of screw dislocations between different glide planes is thought to result in the formation of obstacles on screw dislocations in several materials including $L1_2$, B2 and $L1_0$ based intermetallic alloys like $L1_0$ TiAl, $L1_2$ Ni₃Al, giving rise to the high temperature yield stress peak observed in these structures. As a preliminary step toward an understanding of cross slip in FCC derivative intermetallic alloys, we have performed a parametric study of the cross slip of $a/2[110]$ screw dislocations onto conjugate octahedral planes in a Ni like FCC material, using empirical embedded atom method potentials with varying stacking fault energies. A combination of molecular statics and the newly developed Green's function technique of boundary force relaxation was used in the simulations. Results from this study suggest that the core structure at the constriction is diffuse. Also, self stress forces dominate line tension forces at the constriction leading to significant energetic asymmetry between the two constrictions involved in the cross slip process. The energy of cross slip is found to be smaller than the energy of a jog, indicating that cross slip constrictions are more favorable energetically as compared to the classical 'Stroh' constrictions.

2.6.8 SOLID SOLUTION EFFECTS IN B2 NiAl

Understanding the interactions of solutes with dislocations is important in modeling and designing with intermetallic alloys. In particular, in the case of B2 NiAl alloys, dilute amounts of substitutional impurities like Fe, Mo and Ga are known to have profound effects on their mechanical properties. Classical theories of solute-dislocation interactions have helped provide a basis for modeling, but they suffer from the drawback that continuum theories are used to describe short range solute-dislocation, kink interactions. We have developed a parametric

approach for determining solute-dislocation, kink interactions in metallic systems. Three different parameters which describe discrete solute-dislocation interactions: size, modulus and chemical are varied in a systematic manner. Different substitutional solute potentials for B2 NiAl are developed, within the empirical Embedded Atom Method (EAM) format. Solute potentials thus obtained have been used to simulate the interaction of substitutional solutes with rigid straight [001] mixed dislocations (line direction [111]), in B2 NiAl. Simulation results have been used to assess the strength of size, modulus and chemical terms in solute-dislocation interactions in B2 NiAl.

To study solute-kink interactions, the structure and mobilities of $a/6\langle 112 \rangle$, $a/3\langle 112 \rangle$ and $a\langle 112 \rangle$ kinks on $a\langle 001 \rangle$ mixed dislocations in B2 NiAl have been simulated using a combination of EAM and Green's function techniques. It is found that the formation energy of $a\langle 112 \rangle$ kinks are significantly larger than the other two type of kinks, indicating that they do not play a major role in the low temperature flow behavior of B2 NiAl. The formation energy of the other two types of kink pairs at large separation distances has been found to be comparable and of the order of 0.40 eV, which is in accordance with experimental determination of the activation energy for low temperature flow process at zero stress. The mobilities of single $a/3\langle 112 \rangle$ kinks have been found to be large in general, with stress to move kinks at 0°K to be less than 0.0005-0.002 m. However, atomistic simulations of the mobilities of single $a/6\langle 112 \rangle$ kinks show that for particular kink types and direction of the applied stress, the mobilities could be low with stress to move values of the order of 0.005-0.006 m. Such low mobilities for the $a/6\langle 112 \rangle$ kinks have been found only for two cases. For all other $a/6\langle 112 \rangle$ kinks and directions of the applied stress, the stress to move values are less than 0.002 m.

The results of the $a/6\langle 112 \rangle$ single kink simulations are being used to study the energies of propagation stresses of unstable kink pair configurations at various separation distances in an attempt to correlate with the low temperature flow behavior of B2 NiAl. To date, simulations of kink propagation stresses for four types of $a/6\langle 112 \rangle$ kink pair configurations at a separation

distance of $2b$ have been performed. The results from this study so far show that the stress required to propagate kink pairs even at a small separation distance of $2b$ is significantly smaller than the stress required to move a rigid dislocation, suggesting that kink pair propagation is the active deformation process even at very low temperatures approaching 0°K .

2.6.9 PREDICTING POINT DEFECT PROPERTIES AND POINT DEFECT-DISLOCATION INTERACTIONS IN INTERMETALLIC ALLOYS

One tool alloy designers use to improve the flow and fracture behavior of high temperature intermetallic alloys is alloy chemistry. The activation and propagation of glide systems for a range of deformation temperatures is influenced by the presence of dilute substitutional and interstitial solutes. In order to control the deformation modes as a function of alloy chemistry, alloy designers require a better understanding of the interaction of point defects with dislocation line segments. Using state-of-the-art electronic structure methods, we are calculating point defect properties in simple metals and intermetallic alloys. The interaction of point defects with dislocation line segments can then be determined using a classical solute-dislocation interaction model (Fleischer and Rao). Size misfit parameters have been calculated for constitutional and ternary point defects in B2 NiAl (Cu) , $\gamma \text{ TiAl (Nb and Si)}$, and B32 LiAl . Modulus misfit parameters are being calculated for these defects. Tables 2-5, 2-6, and 2-7 contain the results of these calculations, up to this time, for NiAl , TiAl and LiAl respectively. Results are in reasonable agreement with available experimental data.

2.6.10 POINT DEFECT PROPERTIES IN INTERMETALLIC ALLOYS

Using the results of first principles electronic structure calculations in a statistical mechanics model, we predict the density of thermal point defects as a function of stoichiometry and temperature. Limited experimental data exist for the density of thermal defects in intermetallic alloys that are candidates for high temperature structural applications. However, a

Table 2-5. Size Misfit in B2 NiAl.

Defect	$\frac{1}{V} \frac{\partial V}{\partial c}$	
	Exp. ¹	This Work
V _{Ni}	-0.492	-0.356
V _{Al}	---	-0.159
Al _{Ni}	---	0.757
Ni _{Al}	-0.230	-0.028
Cu _{Ni}	0.102	0.142

¹Taylor and Doyle, 1972²Jacobi and Engell, 1971Table 2-6. Size Misfit in γ TiAl.

Defect	$\frac{1}{a_0} \frac{\partial a_0}{\partial c} (10^{-3})$			$\frac{1}{c_0} \frac{\partial c_0}{\partial c} (10^{-3})$		
	Exp. ¹	Exp. ²	This Work	Exp. ¹	Exp. ²	This Work
V _{Ti}	--	--	-2.80	--	--	-2.24
V _{Al}	--	--	6.25	--	--	-4.10
Al _{Ti}	-35.3±0.8	-41.9±2.3	-6.64	19.0±0.4	2.31±0.2	7.45
Ti _{Al}	--	--	1.85	--	--	-4.37
Nb _{Ti}	--	--	0.70	--	--	0.91
Nb _{Al}	--	--	3.79	--	--	-6.89

¹Taylor, 1952; ²Mennon, 1996

Table 2-7. Size Misfit in B32 LiAl

Defect	$\frac{1}{V} \frac{\partial V}{\partial c}$	
	Exp. ¹	This work
V _{Li}	-0.29	-0.36
Li _{Al}	0.25	-0.33

¹K. Kishio, J. O. Brittain, J. Phys. Chem. Solids, 1979.

wealth of experimental information is available for B32 LiAl because of interest in using this material in high energy density batteries and as a blanket material in fusion reactors. We have calculated the density of point defects in B32 LiAl using the defect energies calculated from first principles methods in a simple thermodynamic model. The results of these calculations are shown in Fig. 2-24. The experimental data of Kishio and Britain are shown as filled and open circles, the present results are shown as solid and dashed lines. Results based on calculations using 16 and 64 atom unit cells, the defect densities are so large in LiAl that the 16 atom primitive unit cell is representative of the real material. Our results for the 16 atom unit cell are in excellent agreement with the experimental results. The 64 atom results also follow the experimental data when the defect densities are evaluated at lower (500K) temperatures. Similar plots results have been calculated for both binary and ternary alloys of TiAl (Nb, and Si). These are shown in Figs. 2-25, 2-26, and 2-27. Site selection of ternary additions can be determined from this analysis. For example, in good agreement with ALCHEMI experiments, we find that Nb prefers to substitute on Ti sites in Al rich TiAl. These thermal defect properties as a function of composition and temperature can be used to study predict trends in solid solution strengthening. Also, the concentration of thermal vacancies as a function of composition can be used to optimize properties associated with mass transport (diffusion) such as creep.

2.6.11 FIRST PRINCIPLES DETERMINATION OF CRITICAL PARAMETERS FOR MATERIALS PROPERTIES

The long term objective is to put in place a set of robust and well documented first principles methods that can be used to sample key defect centers in a wide class of structural materials. The motivation for this work comes from the fact that atomistic, and mesoscopic methods are based on uncontrolled approximations and as such are limited in their predictive capabilities. First principles methods offer systematic and well defined procedures for improving the accuracy of a method and are used extensively in many fields to predict specific materials

Point defect Concentration in B32 LiAl

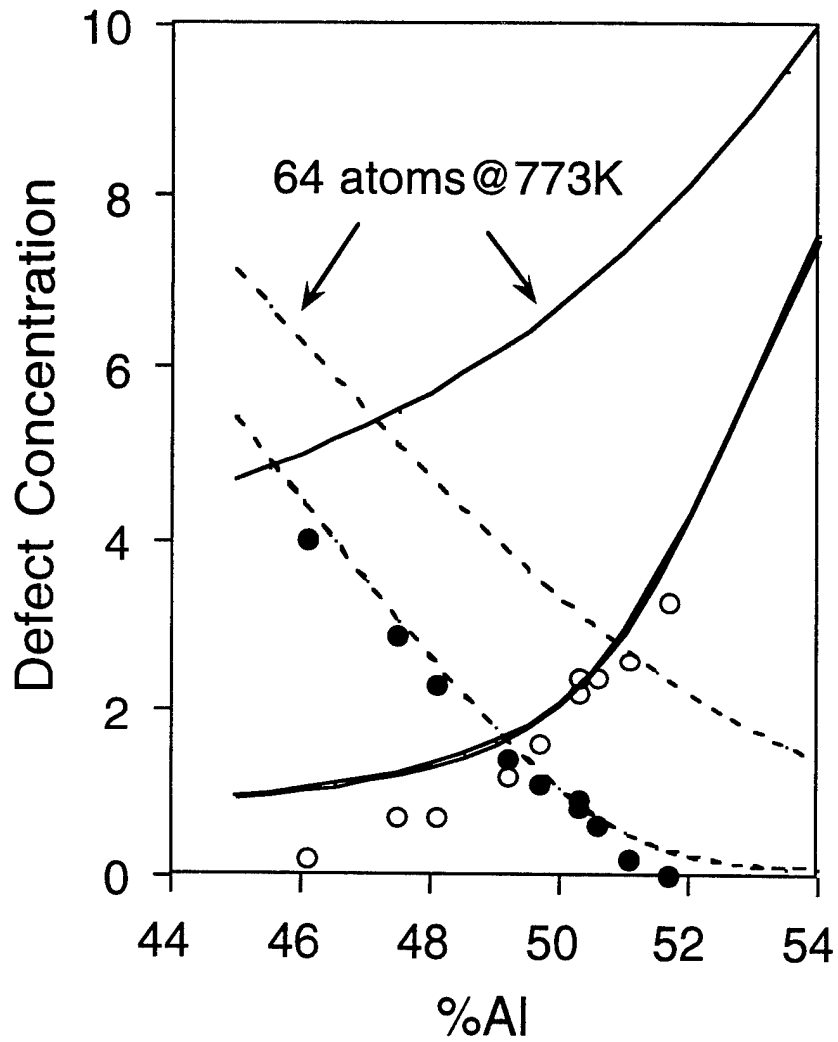


Figure 2-24. Density of Thermal Point Defects in B32 LiAl.

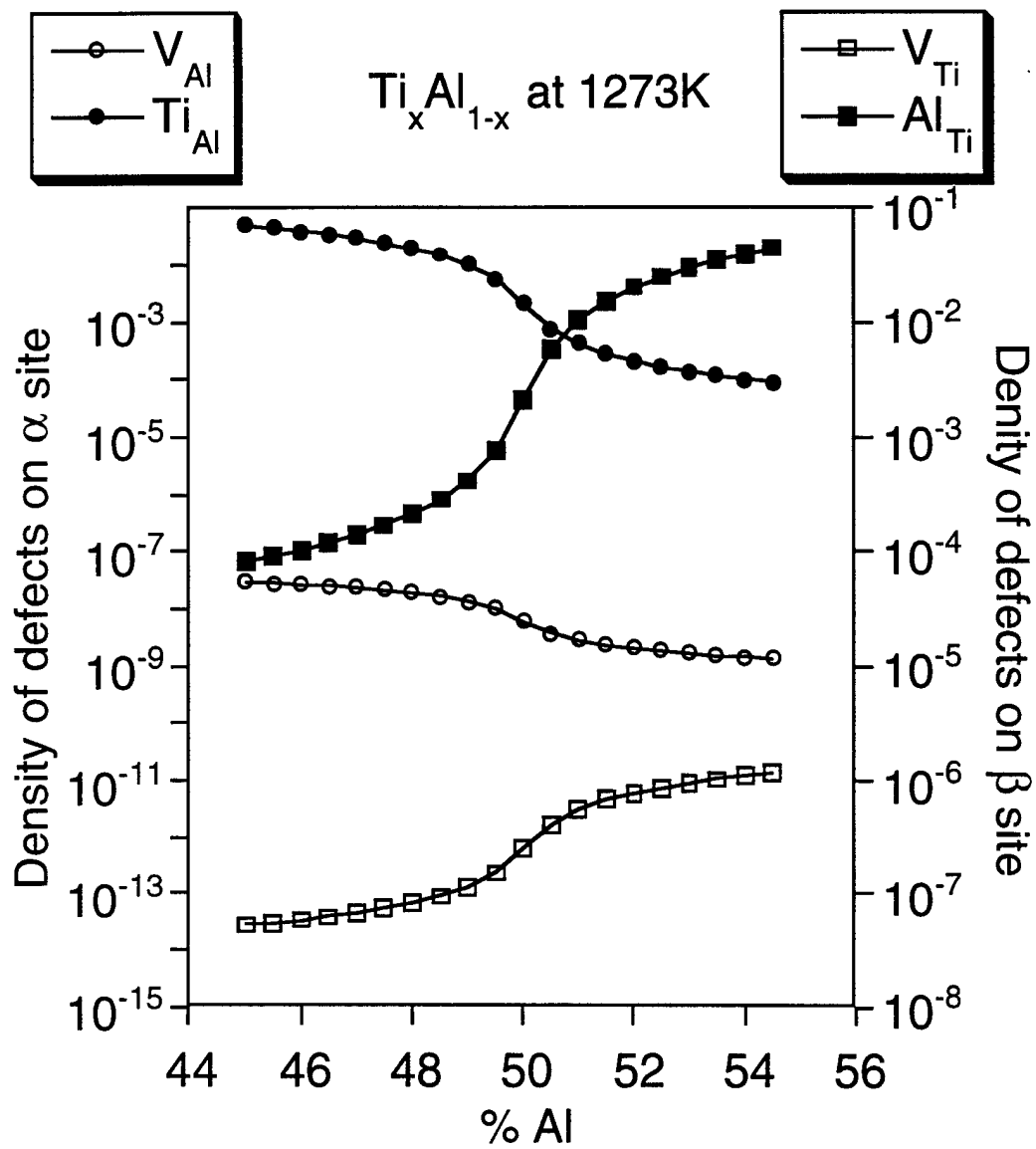


Figure 2-25. Density of Thermal Point Defects in TiAl.

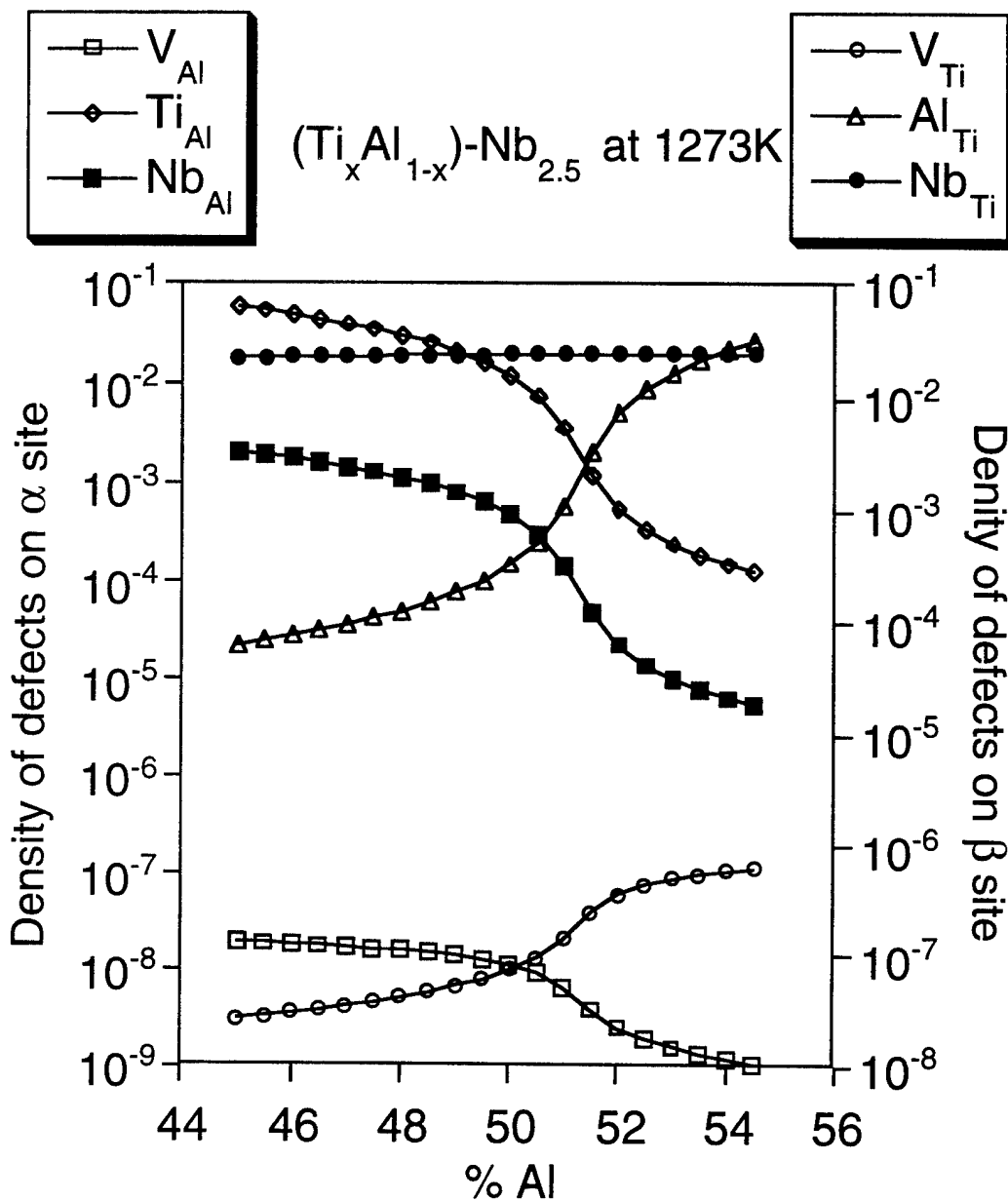


Figure 2-26. Density of Thermal Point Defects in TiAl-Nb.

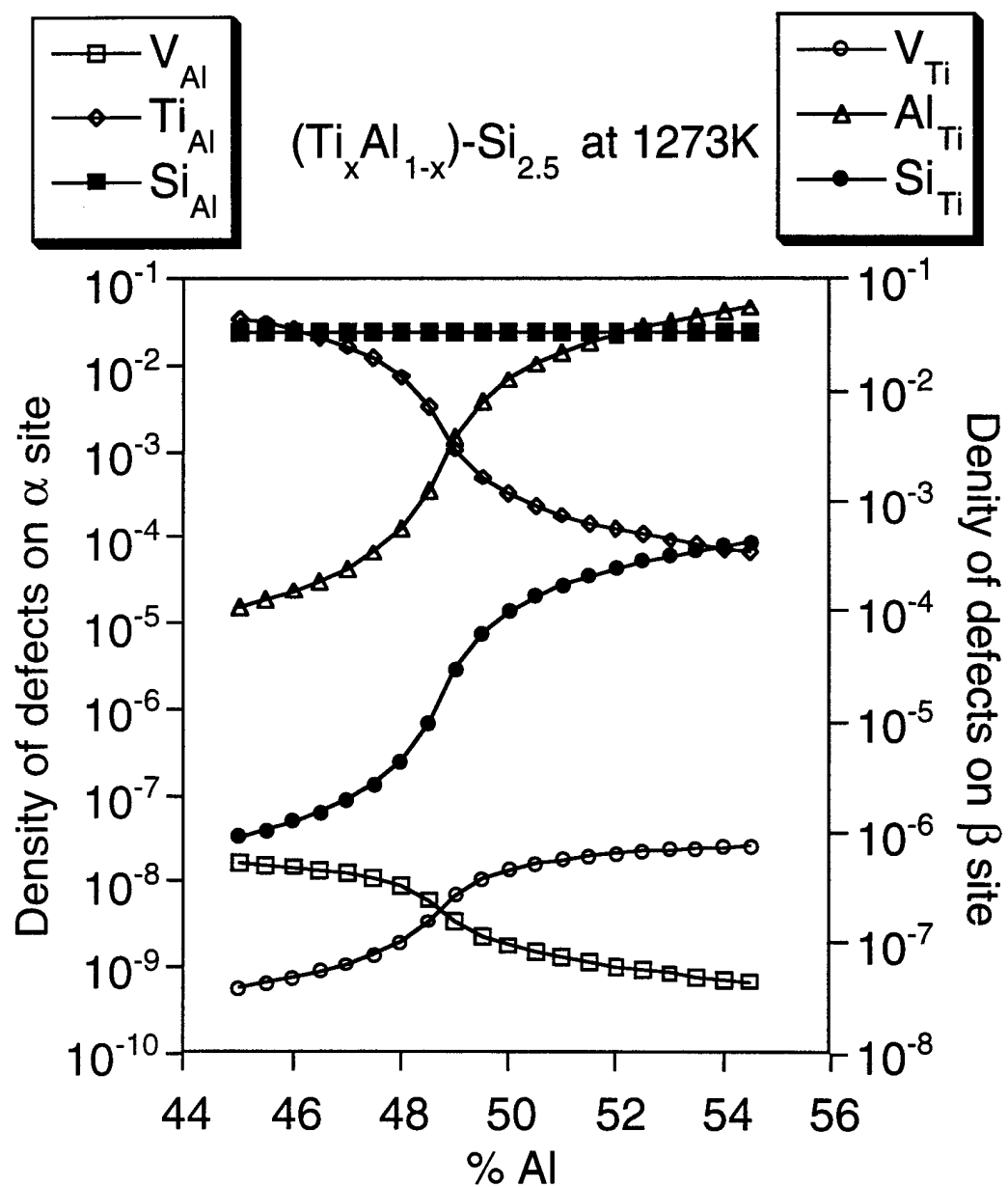


Figure 2-27. Density of Thermal Point Defects in TiAl-Si.

properties. Also, one of the major critical areas that emerged from the Materials Directorate in-house review of the research was the use of parallel processing to perform computational research. The latest generation of parallel processors have enormous potential for applications to Material Science problems. In order to take advantage of these resources, UES, Inc. is porting serial programs to these parallel platforms (see previous research topic). This work will focus almost exclusively on electronic structure methods. A major code development project (~2.5 FTE) is now underway. In collaboration with David Singh (Naval Research Laboratory), the first principles electronic structure method is being ported to scaleable parallel architectures. The existing method has been ported to a scaleable parallel computer (the SP-2), and a version for the T3D will be available shortly.

2.6.12 DEVELOPMENT OF A PHASE TRANSFORMATIONS INITIATIVE

Work is underway defining a research effort in microstructural evolution in alloys. The overall objective of the present phase of this work is to determine the windows of opportunity for making an impact on the field by: (1) determining the state of the technology available for this effort and by (2) assessing the Air Force needs.

The first of these objectives is being met by organizing a seminar series of presentations in which leaders in their respective fields will be asked to give a presentation to address the opportunities afforded by modern computational techniques towards simulations of microstructural evolution in alloys. This series is expected to involve representatives of: (1) the electronic structure and atomistics communities, (2) the phase transformations community, and (3) the alloy processing community. The first of these speakers, Professor Y. Wang, of the Ohio State University, will give a presentation on the mean field methods and results of the Khachaturyan group. In addition to this, an extensive literature survey is being conducted of works published in the literature on microstructural evolution simulations as well as studies of microstructural evolution in superalloys and titanium aluminides.

The Air Force needs are presently being assessed by consultation with Air Force personnel as well as attending relevant conferences. To this end, the Eighth International Symposium on Superalloys was attended.

2.7 PUBLICATIONS

1. M. G. Mendiratta and D. M. Dimiduk, "Strength and Toughness of a Nb/Nb₅Si₃ Composite," *Metall. Trans. A*, 24A, 501-504 (1993).
2. M. G. Mendiratta, Y-W. Kim, and D. M. Dimiduk "Loading Rate Effects and Fracture in a TiAl Alloy," *MRS Symposium Proceedings*, 288, 543-548 (1993).
3. D. M. Dimiduk, M. G. Mendiratta, and P. R. Subramanian, "Development Approaches for Advanced Intermetallic Materials - Historical Perspective and Selected Successes," in *Structural Intermetallics*, Eds., R. Darolia, J. J. Lewandowski, C. T. Liu, P. L. Martin, D. B. Miracle, and M. V. Nathal, TMS, Warrendale, PA, 619-630 (1993).
4. P. M. Hazzledine, B. K. Kad, and M. G. Mendiratta, "Internal Strains and Relaxations in Lamellar TiAl," in *Thin Films: Stresses and Mechanical Properties IV*, Eds., P. H. Townsend, T. P. Weihs, J. E. Sanchez, and P. Borgesen, *MRS Symposium Proceedings*, 725-730 (1993).
5. P. R. Subramanian, M. G. Mendiratta, and D. M. Dimiduk, "Microstructures and Mechanical Behavior of Nb-Ti Base Beta + Silicide Alloys," in *High-Temperature Silicides and Refractory Alloys*, Eds., C. L. Briant, J. J. Petrovic, B. P. Bewlay, A. K. Vasudevan, and H. A. Lipsitt, *MRS Symposium Proceedings*, 322, 491-502 (1994).
6. P. R. Subramanian, M. G. Mendiratta, and D. B. Miracle, "Microstructures and Mechanical Behavior of NiAl-Mo and NiAl-Mo-Ti Two-Phase Alloys," *Metall. Trans. A*, 25A, 2769-2781 (1994).
7. P. R. Subramanian, T. A. Parthasarathy, M. G. Mendiratta, and D. M. Dimiduk, "Compressive Creep Behavior of Nb₅Si₃," *Scripta Metall. et Mater.*, 32(8), 1227-1232. (1995).
8. G. A. Henshall, M. J. Strum, P. R. Subramanian, and M. G. Mendiratta, "Simulations of Creep in Ductile-Phase Toughened Nb₅Si₃/Nb In-Situ Composites," in *High-Temperature*

Ordered Intermetallic Alloys VI, Eds., J. A. Horton, I. Baker, S. Hanada, R. D. Noebe, and D. S. Schwartz, MRS Symposium Proceedings, 364, 937-942 (1995).

9. K. S. Ravichandran, D. B. Miracle, and M. G. Mendiratta, "Microstructure and Mechanical Behavior of Cr-Cr₂Hf In-Situ Intermetallic Composites," Metall. Trans. A, 27A, 2583-2592 (1996).
10. M. G. Mendiratta, R. L. Goetz, and D. M. Dimiduk, "Notch Fracture in γ -Titanium Aluminides," Metall. Trans A, 27A, 390-3912, (1996).
11. M. G. Mendiratta and P. R. Subramanian, "Evaluation of Cr₂Nb/(Cr) and Cr₂Nb/(Nb) Composites as High Temperature Structural Materials," Submitted to Mater. Sci. & Eng. A (1996).
12. M. G. Mendiratta, R. Goetz, D. M. Dimiduk, and J. J. Lewandowski, "Unconstrained and Constrained Tensile Flow and Fracture Behavior of an Nb-1.24 at.% Si Alloy," Mater. Trans A, 26A, 1767-1776 (1995).
13. M. G. Mendiratta and D. M. Dimiduk, "Strength and Toughness of a Nb/Nb₅Si₃ Composite," Mater Trans A, 24A, 501-501 (1993).
14. M. Mendiratta and D. M. Dimiduk, "Phase Relations and Transformation Kinetics in the High Nb Region of the Nb-Si System," Scripta Metall. et Mater., 25, 237-242 (1991).
15. M. Mendiratta, J. J. Lewandowski and D. M. Dimiduk, "Strength and Ductile-Phase Toughening in the Two-Phase Nb/Nb₅Si₃ Alloys," Metall. Trans. A, 22A, 1573-83 (1991).
16. D. M. Dimiduk, D. B. Miracle, Y-W. Kim and M. G. Mendiratta, "Recent Progress on Intermetallic Alloys for Advanced Aerospace Systems," ISIJ International, special issue on Advanced High Temperature Intermetallics, 31, 1222-33 (1991).
17. M. G. Mendiratta and D. M. Dimiduk "Strength and Toughness of a Nb/Nb₅Si₃ Composite," Metall. Trans. A, 24A, 501-504 (1993).
18. S. Rao, D. M. Dimiduk, and M. Mendiratta, "Anisotropic Analysis of Dislocation Line Energies and Possible Dislocation Core Dissociations in MoSi₂," Phil. Mag. A, 68, 1295-1313 (1993).
19. D. M. Dimiduk, P. R. Subramanian, and M. G. Mendiratta, "Exploration of Nb-Based Advanced Intermetallic Materials," Acta Metall. Sinica, 8, 519-530 (1995).

20. P. R. Subramanian, M. G. Mendiratta, and D. M. Dimiduk, "The Development of Nb-Based Advanced Intermetallic Alloys for Structural Applications," *JOM*, 48(1), 33-38 (1996).
21. E. S. K. Menon, P. R. Subramanian, and D. M. Dimiduk, "Phase Equilibria in Niobium Rich Nb-Al-Ti Alloys," *Scripta Metall. et Mater.*, 27, 265-270 (1992).
22. D. B. Miracle, Frank Scheltens, and P. R. Subramanian, "Crystal Structure Determination of Al₂Ta," *Phil. Mag. B*, 71(5), 941-953 (1995).
23. E. S. K. Menon, P. R. Subramanian, and D. M. Dimiduk, "Phase Transformations in Nb-Al-Ti Alloys," *Metall. Trans. A*, 27A, 1647-1659 (1996).
24. P. R. Subramanian and J. A. Shields, Jr., "Refractory Metals and Materials: Joining and Applications," *JOM*, 48(1), 32 (1996).
25. G. A. Henshall, P. R. Subramanian, M. J. Strum, and M. G. Mendiratta, "Continuum Predictions of Deformation in Composites With Two Creeping Phases - II. Nb₅Si₃/Nb Composites," *Acta Metall. Mater.*, submitted (1996).
26. Y-W. Kim, "Microstructural Evolution and Mechanical Properties of a Forged Gamma Titanium Aluminide Alloy," *Acta Metall. Mater.*, 40(6), 1121-1134 (1992).
27. C. T. Liu and Y-W. Kim, "Room-Temperature Environmental Embrittlement in a TiAl Alloy," *Scripta Metall. et Mater.*, 27, 599-603 (1992).
28. K. S. Chan and Y-W. Kim, "Influence of Microstructure on Crack-Tip Micromechanics and Fracture Behaviors of a Two-Phase TiAl Alloy," *Metall. Trans. A*, 23A, 1663-1677 (1992).
29. Y-W. Kim and D. M. Dimiduk, "Processing/Microstructure/Property Relationships in TiAl Alloys," in Processing, Properties and Applications of Metallic and Ceramic Materials, Eds., M. H. Loretto and C. J. Beavers, September 7-10, 1992, IRC, Birmingham, UK, Vol. II, pp. 589-600.
30. Y-W. Kim, "Effects of Microstructure on the Tensile, Fracture Toughness and Fatigue Behavior of TiAl Alloys," in Proceedings of International Workshop on Ordered Intermetallics, Eds., D. Lin and C. T. Liu, 28 September -1 October 2, Hangzhou, China; Also in *J. Mater. Sci. Technol.*, 10, 79-91 (1994).
31. Y-W. Kim and D. M. Dimiduk, "Strain-Rate Effects on the Room Temperature Tensile Properties of a TiAl Alloy," *MRS Symposium Proceedings*, 288, 671-677 (1993).

32. K. S. Chan and Y-W. Kim, "Rate and Environmental Effects on Fracture of a Two-Phase TiAl-Alloy," Metall. Trans. A, 24A, 113-125 (1993).
33. Y-W. Kim, "TiAl Alloys as High Temperature Structural Materials ?," in The Bulletin of the Japan Institute of Metals, NKZKAU, 32(2), 73-77 (1993).
34. Y-W. Kim and D. M. Dimiduk, "Deformation and Fracture Behavior of Gamma Titanium Aluminides," in Aspects of High Temperature Deformation and Fracture of Crystalline Materials - JIMIS-7, Eds., Y. Hosoi, et al., Japan Institute of Metals, Sendai, Japan, 373-382 (1993).
35. W. B. Lee, H. S. Yang, Y-W. Kim, and A. K. Mukherjee, "Superplastic Behavior in Two-Phase TiAl Alloy," Scripta Metall. et Mater., 29(11), 1403-1408 (1993).
36. Y-W. Kim, "Current Status of the Research and Development on Gamma TiAl Alloys," in Intermetallic Compounds for High Temperature Structural Applications, Eds., M. Yamaguchi and H. Fukutomi, 3rd Japan International SAMPE Symposium, Chiba, Japan, pp. 1310-1317, December 7-10, 1993.
37. Y-W. Kim, "Titanium Aluminides and Their Applications," in Encyclopedia of Advanced Materials, Eds., D. Bloor, et al., Pergamon Press, Oxford, pp. 2873-2880, (1994).
38. K. Chan and Y-W. Kim, "Relationships between Slip Morphology, Microcracking and Fracture Resistance in a Lamellar TiAl Alloy," Metall. Trans. A, 25A, 1217-28, (1994).
39. G. Malakondaiah, Y-W. Kim, and T. Nicholas, "Some Observations on the Ambient Temperature Deformation Behavior of Fully-Lamellar Ti-46Al-2Cr-2Nb Alloy," Scripta Metall. et Mater., 30(7), 939-944 (1994).
40. Y-W. Kim, "Ordered Intermetallic Alloys, Part III: Gamma Titanium Aluminides," JOM, 30-39 (1994).
41. K. Chan and Y-W. Kim, "Effects of Lamellae Spacing and Colony Size on the Fracture Resistance of a Fully-Lamellar TiAl Alloy," Acta Metall. et Mater., 43(2) 439-451 (1995).
43. J. Kumpfert, Y-W. Kim and D. M. Dimiduk, "Effect of Microstructure on Fatigue and Tensile Properties of the Gamma Alloy Ti-46.5Al-2.1Cr-3.0Nb-0.2W," Mater. Sci. Eng., A192/193, 463-473 (1995).
44. Y-W. Kim, "Effects of Microstructure on the Deformation and Fracture of TiAl Alloys," Mater. Sci. Eng., A192, 519-533 (1995).

45. K. T. V. Rao, Y-W. Kim, C. L. Muhlstein, and R. O. Ritchie, "Fatigue-Crack Growth and Fracture Resistance of Duplex and Lamellar Microstructures in a Two-Phase TiAl Intermetallic Alloy," *Mater. Sci. Eng.*, A192/193, 474-482 (1995).
46. K. T. Venkateswara Rao, Y-W. Kim, and R. O. Ritchie, "Fatigue Crack Growth Behavior in a Two-Phase TiAl Intermetallic Alloy," *Scripta Metall. et Mater.*, 33, 459-465 (1995).
47. Y-W. Kim, "Gamma Titanium Aluminides: Their Status and Future," *JOM* 39-41, (1995).
48. K. T. V. Rao, Y-W. Kim, and R. O. Ritchie, "Fatigue-Crack Growth Behavior in a Dual-Phase ($\gamma+\alpha_2$) TiAl Intermetallic Alloy at Elevated Temperatures," in Gamma Titanium Aluminides I, Eds., Y-W. Kim, R. Wagner, and M. Yamaguchi, TMS, Warrendale, PA 893-902 (1995).
48. M. Yoshihara, K. Miura, and Y-W. Kim, "Oxidation Behavior of Structure-Controlled TiAl," in Gamma Titanium Aluminides I, Eds., Y-W. Kim, R. Wagner and M. Yamaguchi, TMS, Warrendale, PA, 93-100 (1995).
50. S. W. Schwenker and Y-W. Kim, "The Creep Behavior of Gamma Alloy Ti-46.5Al-3Nb-2Cr-0.2W in Two Microstructural Conditions," in Gamma Titanium Aluminides I, Eds., Y-W. Kim, R. Wagner, and M. Yamaguchi, TMS, Warrendale, PA, 985-992 (1995).
51. Y-W. Kim, "Trends in the Development of Gamma Alloys," in Gamma Titanium Aluminides I, Eds., Y-W. Kim, R. Wagner, and M. Yamaguchi, TMS, Warrendale, PA, 637-654 (1995).
52. D. U. Furrer, R. R. Hoffman, and Y-W. Kim, "Closed-Die Impression Forging of Near-Gamma TiAl," in Gamma Titanium Aluminides I, Eds., Y-W. Kim, R. Wagner, and M. Yamaguchi, TMS, Warrendale, PA, 611-618 (1995).
53. R. S. Mishra, W. B. Lee, A. K. Mukherjee, and Y-W. Kim, "Mechanism of Superplasticity in Gamma TiAl Alloys," in Gamma Titanium Aluminides I, Eds., Y-W. Kim, R. Wagner, and M. Yamaguchi, TMS, Warrendale, PA, 571-578 (1995).
54. Z. Jin, C. Cady, G. T. Gray III, and Y-W. Kim, "Mechanical Response and Microcrack Formation in Fine-Grained Duplex TiAl at Different Strain Rates and Temperatures," in Deformation and Fracture of Ordered Intermetallic Materials, Eds., W. O. Soboyejo, T. S. Srivatsan, and H. L. Fraser, TMS, Warrendale, PA (1996).
55. Y-W. Kim, "Equilibrium and Nonequilibrium Phase Relations in Ti-(25-55)Al," *Metall. Trans. A*, Submitted for publication (1996).

56. P. M. Hazzledine and Y. Q. Sun, "The Strain Field and Work-Hardening from Antiphase Boundary Tubes in Ordered Alloys," *Mater. Sci. Eng.*, A152, 189 (1992).
57. P. M. Hazzledine, "Direct Versus Indirect Dispersion Hardening," *Scripta Metall. et Mater.*, 26, 57 (1992).
58. B. K. Kad and P. M. Hazzledine, "Shear Boundaries in Lamellar TiAl," *Phil. Mag. Letts.* 66, 133 (1992).
59. C. H. Worner and P. M. Hazzledine, "Abnormal Grain Growth in Systems with Different Dimensionality," *Mater. Sci. Forum*, 113-115, 379 (1992).
60. P. M. Hazzledine, B. K. Kad, H. L. Fraser, and D. M. Dimiduk, "Internal Stresses in TiAl-Based Lamellar Composites," *MRS Symposium Proceedings*, 273, 81 (1992).
61. R. I. Todd and P. M. Hazzledine, "Large Anelastic Strains at Constant Volume in Superplastic Tin-Lead Eutectic Alloy," *Scripta Metall. et Mater.*, 27, 127 (1992).
62. C. H. Worner and P. M. Hazzledine, "Grain Growth Stagnation by Inclusions or Pores," *JOM*, 44[9], 16 (1992).
63. P. M. Hazzledine and J. H. Schneibel, "Theory of Coble Creep for Irregular Grain Structures," *Acta Metall. et Mater.*, 41, 1253 (1993).
64. C. H. Worner and P. M. Hazzledine, "An Analytical Model for Two-Dimensional Zener Drag," *Scripta Metall. et Mater.*, 28, 337 (1993).
65. B. K. Kad, H. L. Fraser, and P. M. Hazzledine, "Lamellar Interfaces and Their Contribution to Plastic Flow Anisotropy in TiAl-Based Alloys," *MRS Symposium Proceedings*, 288, 495 (1993).
65. P. M. Hazzledine, K. S. Kumar, A. G. Jackson, and D. B. Miracle, "Synchroshear of Laves Phases," *MRS Symposium Proceedings*, 288, 591 (1993).
67. M. A. Stucke, D. M. Dimiduk, and P. M. Hazzledine, "The Influence of Prestrain on the Flow Stress Anomaly in TiAl Single Crystals," *MRS Symposium Proceedings*, 288, 471 (1993).
68. D. J. Evans, S. A. Court, P. M. Hazzledine, and H. L. Fraser, "Deformation Mechanisms in the Intermetallic Compound MoSi₂," *MRS Symposium Proceedings*, 288, 567 (1993).
69. P. M. Hazzledine and P. Pirouz, "Synchroshear Transformations in Laves Phases," *Scripta Metall. et Mater.*, 28, 1277 (1993).

70. D. J. Evans, S. A. Court, P. M. Hazzledine, and H. L. Fraser, "Dislocation Dissociation in the Intermetallic Compound MoSi_2 ," *Phil. Mag. Letts.*, 67, 331 (1993).
71. P. M. Hazzledine and C. H. Worner, "An Analytical Model for Secondary Recrystallization," in Modeling of Coarsening and Grain Growth, Eds., S. P. Marsh and C. S. Pande, TMS, Warrendale, PA, p. 145 (1993).
72. H. A. Hoff, P. M. Hazzledine, and C. S. Pande, "Montecarlo Simulation of Nanocrystalline Thick Films," in Modeling of Coarsening and Grain Growth, Eds., S. P. Marsh and C. S. Pande, TMS, p. 311 (1993).
73. Y. Q. Sun, P. M. Hazzledine, and J. W. Christian, "Intersections of Deformation Twins in TiAl I," *Phil. Mag., A* 68, 471 (1993).
74. Y. Q. Sun, P. M. Hazzledine, and J. W. Christian, "Intersections of Deformation Twins in TiAl II," *Phil. Mag., A* 68, 495 (1993).
75. P. M. Hazzledine, B. K. Kad, and M. G. Mendiratta, "Internal Strains and Relaxations in Lamellar TiAl," *MRS Symposium Proceedings*, 308, 725 (1993).
76. B. K. Kad, K. S. Vecchio, H. L. Fraser, and P. M. Hazzledine, "Dilatation Versus Shear Effects in Convergent Beam Electron Diffraction Techniques Applied to TiAl-Based Lamellar Composite," *MAS Conference Proceedings*, 2, 224 (1993).
77. P. Pirouz and P. M. Hazzledine, "Dislocations and Polytypic Phase Transformations," *Solid State Phenomena*, 35-36, 183 (1994).
78. B. K. Kad, P. M. Hazzledine, and H. L. Fraser, "On the Mechanism of Transformation of γ -TiAl from α_2 -Ti₃Al," *MRS Symposium Proceedings*, 319, 311 (1994).
79. P. M. Hazzledine, "Twinning by Synchroshear in the Cubic Laves Phase," in Twinning in Advanced Materials, Eds., M. H. Yoo and M. Wuttig, TMS, Warrendale, PA, pp. 403 (1994).
80. P. M. Hazzledine and N. P. Louat, "Direct As Against Indirect Dispersion Work Hardening," *Phil. Mag. Letts.*, 70, 129 (1994).
81. P. M. Hazzledine and B. K. Kad, "Yield and Fracture of Lamellar γ/α_2 TiAl Alloys," *Mater. Sci. Eng.*, A192/193, 340 (1995).

82. Y. Q. Sun, G. Taylor, R. Darolia, and P. M. Hazzledine, "<111> Slip in NiAl Single Crystals Between 4.2K and 100K," MRS Symposium Proceedings, 364, 261 (1995).
83. D. M. Dimiduk, Y. Q. Sun, and P. M. Hazzledine, "Interfacial Structure and Lattice Mismatch in Lamellar TiAl Alloys," MRS Symposium Proceedings, 364, 599 (1995).
84. K. S. Kumar and P. M. Hazzledine, "The C14-to-C15 Transformation in Cr₂Hf," MRS Symposium Proceedings, 364, 1383 (1995).
85. T. R. Smith, R. W. Armstrong, P. M. Hazzledine, R. A. Masumura, and C. S. Pande, "Pile-up Based Hall-Petch Considerations at Ultra-Fine Grain Sizes," MRS Symposium Proceedings, 362, 31 (1995).
86. P. M. Hazzledine, "The Hall-Petch Effect in Lamellar TiAl," in Micromechanics of Advanced Materials, Eds., S. N. G. Chu, P. K. Liaw, R. J. Arsenault, K. Sadananda, K. S. Chan, W. W. Gerberich, C. C. Chau, and T. M. Kung. TMS, p. 551 (1995).
87. M. A. Grinfeld and P. M. Hazzledine, "Rearrangement at Coherent Interfaces in Heterogeneous Solids," Phil. Mag. Letts., 74, 17 (1996).
88. P. M. Hazzledine and S. Rao, "Yield Stress of Nano and Micro Multilayers," MRS Symposium Proceedings, 434, 135-140 (1996).
89. J. Simmons, S. Rao, and D. Dimiduk, "Atomistic Simulations of Structures and Properties of 1/2<1010> Dislocations Using Three Different Embedded Atom Method Potentials Fit to γ -TiAl," Phil. Mag. A, in press.
90. C. Woodward and J. M. MacLaren, "Planar Fault Energies and Sessile Dislocations in Substitutionally Disordered TiAl with Nb and Cr Additions," Phil. Mag., A74, 337 (1996).
91. J. P. Simmons, M. J. Mills, and S. Rao, "Structure of 1/2[110] Dislocations in γ -TiAl by High Resolution TEM and Embedded Atom Method Modeling," MRS Symposium Proceedings, 364, 137-144 (1995).
92. S. Rao, P. M. Hazzledine, and D. M. Dimiduk, "Interfacial Strengthening in Semi-Coherent Metallic Multilayers," MRS Symposium Proceedings, 362, 67-77 (1995).
93. S. Rao, C. Woodward, J. Simmons, and D. Dimiduk, "Core Structure and Mobility of a<101> Dislocations in L1₀ TiAl," in High-Temperature Ordered Intermetallic Alloys VI, Eds., J. A. Horton, I. Baker, S. Hanada, R. D. Noebe, and D. S. Schwartz, MRS Symposium Proceedings, 364, 129-135 (1995).

94. C. Woodward, Y. Song, S. P. Tang, J. H. Xu, O. N. Mryasov, A. J. Freeman, and D. M. Dimiduk, "Ti-Ti Bonding in γ -TiAl and FCC Ti," *Phil. Mag. B*, 70B, 987-1002 (1994).
95. S. Rao, B. He, and C. R. Houska, "A Simplified Procedure For Obtaining Relative X-Ray Intensities When A Texture And Atomic Displacements Are Present," *Appl. Phys.*, 75, 4456-4464 (1994).
96. S. Rao, C. H. Wu, and C. R. Houska, "Thermal Diffuse Scattering In Polycrystalline Materials With A Texture," *J. Appl. Phys.*, 75, 4465-4469 (1994).
97. S. I. Rao, C. Woodward, and P. M. Hazzledine, "The Interaction Between Dislocations and Lamellar Grain Boundaries in PST γ TiAl," in Defect-Interface Interactions, Eds., E. P. Kvam, A. H. King, M. J. Mills, T. D. Sands, and V. Vitek, MRS Symposium Proceedings, 319, 285-292 (1994).
98. J. Simmons, S. Rao, and D. M. Dimiduk, "Embedded Atom Method Simulation of $1/2\langle 110 \rangle$ Dislocation Core Structures and Properties in $L1_0$ Compounds," in Alloy Modeling and Design, Eds., G. M. Stocks and P. E. A. Turchi, TMS Proceedings, 183 (1994).
99. C. Woodward and J. M. MacLaren, "Electronic Structure of Planar Faults and Point Defects in High Temperature Intermetallics," in Application of Multiple Scattering Theory to Materials Science, Eds., W. H. Butler, A. Gonis, P. H. Dederichs, and R. L. Weaver, MRS Symposium Proceedings, 253, 387-392 (1994).
100. C. Woodward, J. M. MacLaren, and D. M. Dimiduk, "Energy of Planar Faults as a Function of Composition in Binary and Ternary TiAl Alloys," in High-Temperature Ordered Intermetallic Alloys V, Eds., I. Baker, R. Darolia, J. D. Whittenberger, and M. H. Yoo, MRS Symposium Proceedings, 288, 171-176 (1993).
101. S. Rao, J. P. Simmons, and D. Dimiduk, "Effect of Planar Fault Energies on Dislocation Core Structures and Mobilities in $L1_0$ Compounds," MRS Symposium Proceedings, 288, 335-341 (1993).
102. C. Woodward and J. M. MacLaren, "Electronic Structure of Planar Defects in Ordered and Disordered High Temperature Intermetallics," NATO Conference Proceedings, Greece, June 1992.
103. C. Woodward and R. Benedek, L. H. Yang, and B. I. Min, "Formation Energy and Lattice-Relaxation for Point Defects in Li and Al," *Phys. Rev. B*, 45, 2607-2612 (1992).

104. C. Woodward, J. M. MacLaren, and S. I. Rao, "Electronic Structure of Planar Faults in TiAl," *J. Mater. Res.*, **7**, 1735-1750 (1992).

2.8 PRESENTATIONS

1. M. G. Mendiratta, P. R. Subramanian, R. Goetz, D. M. Dimiduk, "The Flow and Fracture Behavior of Refractory Phase Constituents of In-Situ Intermetallic Matrix Composites," TMS/ASM, Symposium on Fatigue and Fracture of Ordered Intermetallic Materials, TMS/AIME, Fall Meeting, Pittsburgh, PA, October 18, 1993.
2. M. G. Mendiratta, P. R. Subramanian, and D. M. Dimiduk, "Conventional Solidification, Thermomechanical Processing and Mechanical Properties of Intermetallic-Refractory Metal Composites," presented at the Processing and Design Issues in High Temperature Materials, Engineering Foundation Symposium, Devos, Switzerland, May 19-25, 1996,
3. D. M. Dimiduk, M. G. Mendiratta, and P. R. Subramanian, "Development Approaches for Advanced Intermetallic Materials - Historical Perspective and Selected Successes," 1st International Symposium on Structural Intermetallics, Seven Springs, PA, September 26-30, 1993.
4. P. R. Subramanian, M. G. Mendiratta, and D. M. Dimiduk, "Microstructures and Mechanical Behavior of Nb-Ti Base Beta + Silicide Alloys," MRS Fall Meeting, Boston, MA, December 3, 1993.
5. P. R. Subramanian, M. G. Mendiratta, and D. M. Dimiduk, "Refractory Metal-Intermetallic Matrix Composites," Workshop on Refractory Metal-Intermetallic Matrix Composites, Wright State University, Dayton, OH, October 20, 1994.
6. P. R. Subramanian, T. A. Parthasarathy, M. G. Mendiratta, and D. M. Dimiduk, "Creep Behavior of Nb/Nb₅Si₃ In-Situ Composites," MRS Fall Meeting, Boston, MA, November 30, 1994.
7. P. R. Subramanian, Krish Krishnamurthy, and M. G. Mendiratta, "Fabrication of Ti-Aluminide Metal Matrix Composites by Vapor Deposition of Matrix Alloy on Reinforcing Fibers," TMS Annual Meeting, Las Vegas, NV, February 14, 1995.
8. P. R. Subramanian, M. G. Mendiratta, and D. M. Dimiduk, "Development of Niobium-Based Advanced Intermetallic Materials," Bhabha Atomic Research Center (BARC), Trombay, India, December 6, 1995; Indian Institute of Science, Bangalore, India, December 15, 1995.

9. Y-W. Kim, "Microstructure and Properties of Gamma TiAl Alloys for Automobile Applications," EMTEC Meeting on Titanium Aluminides for Automobile Applications, EMTEC, Dayton, OH, January 10, 1992.
10. Y-W. Kim and D. M. Dimiduk, "Processing/Microstructure/Property Relationships in TiAl Alloys," International Conference on Processing, Properties and Applications of Metallic and Ceramic Materials, IRC, Birmingham, England, September 7-10, 1992.
11. Y-W. Kim, "Gamma Titanium Aluminides," Lecture for IRC and University of Birmingham, England, September 11, 1992.
12. Y-W. Kim, "Physical Metallurgy of Gamma TiAl Alloys," Jiao Tong University, Shanghai, China, September 25, 1992.
13. Y-W. Kim, "Effects of Microstructure on the Deformation and Fracture of TiAl Alloys," International Workshop on Ordered Intermetallics (IWOI), Hangzhou, China, September 28, 1992 - October 1, 1992.
14. Y-W. Kim, "TiAl Alloys as High Temperature Structural Materials ?," Guest Lecture for Intermetallic Symposium, JIM (Japan Institute of Metals), Fall Meeting, Toyama, Japan, October 6-8, 1992.
15. Y-W. Kim, "Fundamentals of Gamma TiAl Alloys: Phase Transformations, Deformation and Fracture," Iron & Steel Research Institute Beijing and Shanghai University of Technology, China, July 5-7, 1993.
16. Y-W. Kim, "Gamma Titanium Aluminides," Two-Day Lectures, ADD (Agency for the Defense Department), Daejeon, Korea, July 22-23, 1993.
17. Y-W. Kim and D. M. Dimiduk, "Deformation and Fracture Behavior of Gamma Titanium Aluminides," Lecture at JIMIS-7 (Japan Institute. of Metals International Symposium) on Aspects of High Temperature Deformation and Fracture of Crystalline Materials, Nagya, Japan, July 27-31, 1993.
18. Y-W. Kim, "Evolution and Types of Microstructures in Hot-Worked Gamma Titanium Aluminides," National Research Institute for Metals, Tokyo, Japan, July 27, 1993.
19. Y-W. Kim, "The Application of the Anisotropic Properties of PST Crystals to Explain the Adverse Ductility/Toughness Relations in Gamma TiAl Alloys," Kyoto University, Kyoto, Japan, July 28, 1993.

20. Y-W. Kim, "Tensile Deformation and Fracture Resistance in TiAl Alloys," Symposium on Fatigue and Fracture of Ordered Intermetallics," TMS Meeting, Pittsburgh, PA, October 18-21, 1993.
21. Y-W. Kim, "Effects of Composition and Microstructure on the Mechanical Properties in Gamma TiAl Alloys," Department of Materials Science and Mechanics, Michigan State University, Lansing, MI, November 16, 1993.
22. Y-W. Kim, "Microstructural Evolution and Resulting Mechanical Properties in Gamma TiAl Alloys," A Meeting of R&D Institute of Metals and Composites for Future Industries (RIMCOF), Tokyo, Japan, December 6, 1993.
23. Y-W. Kim, "Current Status of the Research on Gamma TiAl Alloys," International Symposium on Intermetallic Compounds for High-Temperature Structural Applications, at 3rd Japan SAMPE Symposium, TiAl Workshop, Chiba, Japan, December 7-10, 1993.
24. Y-W. Kim, "Nonequilibrium and Phase Transformations in the Ti-(30-51) at.% Al System," Tokyo Institute of Technology, Tokyo, Japan, December 10, 1993.
25. Y-W. Kim, "Fabrication of Automobile Engine Valves from Gamma TiAl Alloys Using Wrought Processing," Meeting jointly called by R&D Groups from GM, Ford and Chrysler, Ford Research Center, Dearborn, MI, April 11, 1994.
26. Y-W. Kim, "New Gamma Alloys for More Demanding Structural Applications," NASA Lewis Research Center, Cleveland, OH, April 12, 1994.
27. Y-W. Kim, "Microstructural Design Using the Understanding of the Inverse Relationships Between Ductility and Fracture Toughness," International Workshop on Practical Aspects of Gamma Titanium Aluminide Alloys, Organized by GKSS, Irsee, Germany, May 2-6, 1994.
28. Y-W. Kim, "High Temperature Deformation and Fracture of Two-Phase Gamma Titanium Aluminides," International Conference on High Temperature Intermetallics and Aluminides, San Diego, CA, May 16-19, 1994.
29. Y-W. Kim, "Potential Applications of Advanced Titanium-Base Alloys in Energy Industry," Metals and Ceramics Division, Oak Ridge National Laboratory, TN, May 27, 1994.
30. Y-W. Kim, "Tensile Deformation and Fracture Behavior of TiAl Alloys in Duplex and Fully-Lamellar Forms," Symposium on Fracture and Fatigue of Ordered Intermetallics, TMS Meeting, Rosemont, IL, October 3-6, 1994.

31. Y-W. Kim, "The Current Status of the Gamma Technology," ASM Cincinnati Division Meeting, University of Cincinnati, Cincinnati, OH, October 13, 1994.
32. Y-W. Kim, "Phase Transformations and Microstructure Evolution in Binary Ti-(30-50)Al Alloys," University of Wisconsin, Madison, WI, November 17, 1994.
33. Y-W. Kim, "Our Current Understanding of the Relationships among Composition, Processing, Microstructure and Mechanical Properties in Gamma TiAl Alloys," International Symposium on Gamma Titanium Aluminide Alloys, TMS Annual Meeting, Las Vegas, NV, February 12-16, 1995.
34. Y-W. Kim, "Recent Advances in Gamma TiAl Alloy Technology," NASA-Lewis, Cleveland, OH, March 2, 1995.
35. Y-W. Kim, "Designing Gamma TiAl Alloys," Internal Workshop on Ordered Intermetallic Alloys and Composites (IWOIAC), Beijing, China, June 25-30, 1995.
36. Y-W. Kim, "Fracture Resistance under Monotonic and Cyclic Loading Conditions," Pohang Steel Institute of Technology, Pohang, Korea, July 12, 1995.
37. Y-W. Kim, "Microstructure Evolution in Wrought Gamma TiAl Alloys," Yokohama National University, Yokohama, Japan, July 21, 1995.
38. Y-W. Kim, "Status of Gamma Alloy Technology-Development of Designed Microstructures," RIMCOF, Tokyo, Japan, July 20, 1995.
39. Y-W. Kim, "Fatigue Deformation and Failure in TiAl Alloys," JIM/TMS All Meeting, Honolulu, HI, December 13-15, 1995.
40. Y-W. Kim, "Development of Refined Lamellar Microstructures," GKSS Research Institute, Geesthacht, Germany, April 17, 1996.
41. Y-W. Kim, "Recent Advances in the Gamma Titanium Aluminide Technology," University of Oxford, Oxford, England, April 26, 1996.
42. Y-W. Kim, "Recent Advances in the Development of Component-Specific Gamma TiAl Alloys," International Workshop on TiAl Alloys, IRC, Birmingham, England, May 1-3, 1996.
43. Y-W. Kim, "Designing Gamma TiAl Alloys," AeroMat'93, Dayton, OH, June 3-6, 1996.
44. Y-W. Kim, "Fatigue Resistance of Gamma TiAl Alloys," POSTECH, Pohang, Korea, July 1, 1996.

45. Y-W. Kim, "Effects of Interstitial Elements on Creep Resistance in Gamma TiAl Alloys," Tohoku University, Sendai, Japan, July 9, 1996.
46. Y-W. Kim, "Issues in the Gamma Alloy Technology," Kyoto University, Kyoto, Japan, July 12, 1996.
47. Y-W. Kim, "Effect of Microstructure on fatigue Resistance in Gamma TiAl Alloys," Symposium on Fatigue and Fracture of Ordered Intermetallics, TMS Fall Meeting, Cincinnati, OH, October 7-10, 1996.
48. P. M. Hazzledine, "Transmission Electron Microscopic Observations of Dislocations in Intermetallic Alloys," presented at the TMS Fall Meeting, 1991, Cincinnati, OH.
49. P. M. Hazzledine, "Work Hardening of Intermetallics," presented at a seminar at Case Western Reserve University, Cleveland, OH, October 7, 1991.
50. P. M. Hazzledine, "Towards Ductile TiAl," presented at a seminar at Georgia Institute of Technology, February 6, 1992.
51. P. M. Hazzledine, "Plasticity of Intermetallics," presented at a seminar at Ohio State University, Columbus, OH, February 28, 1992.
52. P. M. Hazzledine, "An Analytical Model for Secondary Recrystallization," presented at the TMS Fall Meeting, 1992, Chicago, IL.
53. P. M. Hazzledine, "Plasticity of Intermetallics," presented at a seminar at the University of Cincinnati, OH, October 23, 1992.
54. P. M. Hazzledine, Workshop on Synchroshear at Case Western Reserve University, January 14, 1993.
55. P. M. Hazzledine, "Mechanical Properties of Lamellar TiAl," ASM International, presented at Materials Week, October 1993, Pittsburgh, PA.
56. P. M. Hazzledine, "Twinning by Synchroshear in the Cubic Laves Phase," presented at the TMS Symposium on Twinning in Advanced Materials, Materials Week, October 1993, Pittsburgh, PA.
57. P. M. Hazzledine, "Plasticity of Lamellar TiAl," presented at a seminar at the Naval Research Laboratory, Washington, D.C., December 8, 1993.

58. P. M. Hazzledine, "Nucleation and Growth in Lamellar TiAl," presented at the Indo-U.S. Workshop on Physical Metallurgy, Bangalore, India, March 1994.
59. P. M. Hazzledine, "Gamma Titanium Aluminides," presented at the International Workshop on Processing, Properties and Physical Metallurgy, Irsee, Germany, May 1994.
60. P. M. Hazzledine, "Yield and Fracture of Lamellar TiAl," presented at a Seminar at the University of California, Irvine, CA, May 20, 1994.
61. P. M. Hazzledine, "Constitutive Laws for Intermetallics," presented at the Los Alamos Summer Research Group Workshop, Los Alamos National Laboratory, NM, August 1994.
62. P. M. Hazzledine, "Yield and Fracture of Lamellar TiAl," presented at a seminar at Case Western Reserve University, Cleveland, OH, November 8, 1994.
63. P. M. Hazzledine, "Interfacial Strengthening in Semi-Coherent Metallic Multilayers," presented at the MRS Symposium on Grain Size and Mechanical Properties, Boston, MA, December 1994.
64. P. M. Hazzledine, "Theory of Multilayers," presented at a seminar at NITS, Gaithersburg, MD, March 1, 1995.
65. P. M. Hazzledine, "Topics in Mechanical Metallurgy," presented at a seminar at Wayne State University, Detroit, MI, April 22, 1995.
66. P. M. Hazzledine, "Theory of the Yield Stress of Nano-Multilayers," presented at the NIST Workshop on Nanoscale Layered Materials for Protective Coating and Structural Applications, Gaithersburg, MD, August 14-15, 1995.
67. P. M. Hazzledine, "Work-Hardening in Intermetallic Alloys," presented at the NIST Workshop on Computational Simulations of Plasticity, Gaithersburg, MD, September 28-29, 1995.
68. P. M. Hazzledine, "The Hall-Petch Effect in Lamellar TiAl," presented at Mechanics of Advanced Materials, TMS Materials Week, Cleveland, OH, October, 1995.
69. P. M. Hazzledine, "Strength of Nano and Micro Multilayers," presented at a seminar at Brown University, Providence, RI, November 15, 1995.

70. P. M. Hazzledine, "Yield Stress of Nano- and Micro-Multilayers," presented at the MRS Symposium on Layered Materials for Structural Applications, San Francisco, CA, April 1996.
71. C. Woodward, "Elastic and Defect Properties in High Temperature Intermetallic Alloys," Complex Systems Theory Branch, Naval Research Laboratory, Washington, D.C., February 1996.
72. C. Woodward, "Electronic Structure and Atomistic Methods as Tools to Study High Temperature Intermetallic Alloys," Department of Materials Science and Engineering, Ohio State University, Columbus, OH, May 1995.
73. C. Woodward, "Dislocation Stability and Mobility in Intermetallic Alloys," Materials Research Society Meeting, Boston, MA, December 1994.
74. C. Woodward, "Energy of Planar Faults in Binary and Ternary TiAl Alloys," Division H, Lawrence Livermore National Laboratory, Livermore, CA, August 25, 1994.
75. C. Woodward, "Energy of Planar Faults in Binary and Ternary TiAl Alloys," Department of Physics, University of Cincinnati, Cincinnati, OH, May 4, 1994.
76. C. Woodward, "Influence of Chemistry on Dislocation Stability and Mobility in Intermetallic Alloys," Annual TMS/ASM Meeting, Pittsburgh, PA, October 18, 1993.
77. C. Woodward, "Energy of Planar Faults in Binary and Ternary TiAl Alloys," Department of Metallurgy and Materials Engineering, Colorado School of Mines, October 7, 1993.
78. D. M. Dimiduk, C. Woodward, S. I. Rao, J. Simmons, and T. A. Parthasarathy, "Atomistic Modeling of Solution Hardening in Intermetallics," Gordon Research Conference on Physical Metallurgy, Plymouth, NH, August 5, 1993.
79. C. Woodward, "Electronic Structure of Planar Faults and Point Defects in TiAl," Department of Metallurgical and Materials Engineering, Colorado School of Mines, Golden Colorado, January 21, 1993.
80. C. Woodward, "Electronic Structure of Planar Faults and Point Defects in TiAl," Department of Physics, Ohio State University, June 19, 1992.

2.9 INVENTION DISCLOSURES/PATENTS

1. P. R. Subramanian, M. G. Mendiratta, and D. M. Dimiduk, "High Temperature Melting Molybdenum-Chromium-Silicon Alloys," U. S. Patent No. 5,505,793, April 9, 1996.

2. P. R. Subramanian, M. G. Mendiratta, and D. M. Dimiduk, "Niobium-Titanium-Chromium-Aluminum-Silicon Alloys for High-Temperature Applications," U.S. Air Force Invention No. D00060; submitted.
3. P. R. Subramanian, M. G. Mendiratta, and D. M. Dimiduk, "Method of Making High Temperature Melting Molybdenum-Chromium-Silicon Alloys," U.S. Air Force Invention No. 21157A; submitted.
4. Y-W. Kim and D. M. Dimiduk, "Method to Produce Gamma Titanium Aluminide Articles Having Improved Properties," U.S. Patent 5,226,985, July 13, 1993.
5. P. McQuay, D. M. Dimiduk, and Y-W. Kim, "Methods to Produce Gamma Titanium Aluminide Articles Having Improved Properties," U.S. Patent 5,417,781, May 23, 1995.
6. Y-W. Kim and D. M. Dimiduk, "Methods to Design Microstructures for Improved Properties in New Gamma Titanium Aluminide Alloys Containing Small Amounts of Tungsten," U.S. Patent 5,558,729, September 24, 1996
7. Y-W. Kim and D. M. Dimiduk, "Methods to Produce Refined Duplex and Lamellar Microstructures in Wrought-Processed Gamma Titanium Aluminide Alloys by Adding Small Amount of Boron," Invention Disclosure Submitted for US Patent (17 April 1996).
8. Y-W. Kim and D. M. Dimiduk, "Methods to Produce Aligned Lamellar Microstructures by Alpha-Gorging in Gamma Titanium Aluminide Alloys," Invention Disclosure Submitted for US Patent (October 1996).

2.10 BOOKS

1. P. R. Subramanian, D. J. Chakrabarti, and D. E. Laughlin, Phase Diagrams of Binary Copper Alloys, ASM International, Materials Park, OH (1994).

2.11 EDIT CONFERENCE PROCEEDINGS

1. "Gamma Titanium Aluminides," eds. Y-W. Kim, R. Wagner and M. Yamaguchi, TMS, Warrendale, PA, September 1995.

2.12 AWARDS

AFOSR Star Team Award, 1994.

AFOSR Star Team Award, 1991.

2.13 REFERENCES

1. Madan G. Mendiratta, John J. Lewandowski, and Dennis M. Dimiduk, Metall. Trans. A, 22A, 1573-1583 (1991).
2. J. J. Lewandowski, D. Dimiduk, W. R. Kerr, and M. G. Mendiratta, MRS Symposium Proceeding, 120, 103-108, (1990).
3. Madan G. Mendiratta and Dennis M. Dimiduk, Metall. Trans A, 24A, 501-504 (1993).

SECTION 3.0

TASK II. METAL MATRIX COMPOSITES

Titanium alloy/intermetallic based metal matrix composites (MMCs) are considered as 'enabling' materials in a number of aero-propulsion components, particularly under the IHPTET program. For example, IHPTET performance goals stipulate severe stress-temperature combinations in various stages of the turbine compressor, which can only be met (enabled) by incorporating titanium matrix composites (TMCs). Hence, a significant effort is in progress, under the sponsorship of the Air Force, to develop MMCs that meet the stringent load-temperature-weight requirements.

In recent years, the emphasis on hypersonic flight under the NASP program had produced a flurry of activities in MMC research, with the intention of rapidly transitioning the technology to military and commercial usage. A significant part of that effort focused on development of a material database, without sufficient knowledge of the failure mechanisms involved. At the same time, a design methodology had to be established that could not accommodate large factors of safety, due to stringent strength-to-weight requirements. Compounding the problem was the fact that material choices had to be made early, without clear understanding of how constituent properties affected bulk composite response, and how to process composites in a reliable manner. Problems arising from these and other issues led to a rather abrupt decrease in NASP activities.

However, the NASP experience was beneficial, since it highlighted the importance of understanding some fundamental issues in metallic composites. These include: understanding the role of the interface on MMC response, the role of the matrix, its texture, and its modification through reactions with the fiber, matrix stability issues, progressive fiber fracture mechanisms and its effects on creep and thermomechanical fatigue (TMF) response, tailoring of the interface for optimizing properties in the longitudinal and transverse directions, etc. It is precisely here

that ongoing research on MMCs at Wright Laboratory has provided a leadership to the MMC community.

In about 4 years, UES contractors, in collaboration with government staff, visiting scientists, and other research groups at the USAF Materials Directorate, have laid the foundations of a program aimed at developing superior titanium matrix composites. The program at the Materials Directorate is based on the measurement and improvement of constituent properties (primarily those of the interface and the matrix), and on qualitative and quantitative understanding of the influence of constituent properties (including the fiber) on bulk MMC response. A key outcome of the research has been the establishment of a comprehensive methodology that involves fabrication and testing of single-fiber and single-ply MMCs, so that data can be obtained from a small volume of material. This methodology, which is significantly different from approaches used by other research groups working on MMCs, is extremely efficient in terms of the time, efforts, and costs required to evaluate new interfaces and matrix microstructures. The validity of the approach as a tool for improving bulk multi-ply MMC properties has been partially established using modeling and experimental efforts, and is upgraded on a routine basis.

The bulk of the research activities on MMCs can be classified under the following subheadings:

- (1) Interface Research: measurement of interface properties, how those properties influence bulk composite response, and development of interface systems
 - (2) Matrix Research: structure-property understanding of primarily orthorhombic alloys with the goal of obtaining microstructures for optimized TMC performance
 - (3) Composite Research: effects of matrix microstructure on fiber strength utilization and TMC response, including influence of matrix texture and interstitial diffusion.
- Additional research included improvement of an automated digital deformation analysis (ADDA) software for local strain measurements, and preliminary investigation

of fracture mechanisms in discontinuously reinforced aluminum (DRA) composites for improved toughness-strength combination.

3.1 SUMMARY OF MAJOR FINDINGS

3.1.1 INTERFACE BEHAVIOR AND EFFECTS ON MMC RESPONSE

The ultimate goal of this effort was to develop fiber-matrix interfaces that provided improved bulk TMC performance. In particular, there was and still exists a need for optimization of the interface, since the properties required for improved transverse [90°] behavior of the composites are in partial variance to the interface properties required for longitudinal performance. The necessary requirements for this effort were: (1) the existence of methodologies by which the normal and shear properties of interfaces could be characterized, and (2) adequate understanding of how those interface properties actually influenced bulk composite response. As it turned out, both aspects needed attention. First, there were concerns that existing methods for determining interface properties did not adequately address the mechanisms of interface failure that occurred during such tests. For example, while the bulk of push out tests reported in the literature relied on interface crack initiation from the indenter end, our research provided clear evidence of crack propagation from the bottom face due to high residual stresses. Consequently, improvements were needed in the analyses procedures. Similarly, there were concerns that existing methodologies for evaluating the normal strength of interfaces were inadequate due to stress singularities and stress reversals at free surfaces, so that a new specimen geometry had to be designed to avoid such problems. Second, while there was general understanding that the transverse strength and creep response of composites increased with the normal bond strength of the interface, there was inadequate understanding of how the interface affected longitudinal responses, such as the longitudinal strength, fatigue crack growth response, and so on. Without sufficient quantitative understanding, it is not possible to arrive at interface property requirements for optimized TMC performance. Our recent review [1] on interfaces in MMCs provides additional description of the important issues involved.

3.1.1.1 The Push-Out Test

The push-out test for MMCs was investigated in detail, since it is a robust technique for obtaining fiber-matrix interface properties under primarily shear loading. Although many papers have been published on the subject, there remained questions as to the mechanism of interface failure, the crack initiation location, and whether available analyses of push-in were able to provide interface properties that were consistent with the mechanism of failure. Experiments with thick (2 mm and higher) specimens showed that crack initiation in SCS-6/Ti-alloy composites was extremely difficult from the indenter end, because of high residual stresses; i.e., push-in was essentially absent. On the other hand, experiments with thinner specimens (0.4 mm - 0.8 mm) provided clear evidence of crack initiating from the bottom face (away from the indenter) and propagating towards the indenter end (top-face). This mode of failure was established by simultaneously measuring displacements of the fiber at both the top and bottom ends, and indicated that previous analyses of push-out data were in error because crack initiation was assumed to occur from the top face. Stress analyses showed that a shear stress argument was unable to explain the interface fracture mechanism. Therefore, a fracture mechanics procedure was developed for explaining crack propagation from the bottom face, and it provided reasonable values of interface parameters from the push-out test. The interface toughness was found to be around 20 J/m² for SCS-6 fibers in Ti-6Al-4V and Ti-15-3 matrices. Although this is measured at a mode mixity around 75°, yet the number appears high, and may be influenced by radial compression of the fibers due to residual stresses. Initial attempts at obtaining lower values of radial compression were only partially successful, so that additional work is needed for arriving at true values of interface toughness from the push-out test. Refer to [Publications 2-3] for additional details.

3.1.1.2 The Single-Fiber Fragmentation Test

This test was investigated because there were concerns that the push-out test did not simulate interface failure conditions that occur when fibers fail in a ductile matrix composite, in the absence of a matrix crack. Another important reason was that results from this single-fiber test allowed assessment of local versus global load sharing behavior in multiple-fiber specimens under longitudinal tension.

The single-fiber fragmentation test has been successfully used in polymeric composites to arrive at an interface friction stress based on the final average length of fiber fragments and the strength of fibers. Our experiments involved testing of single-fiber SiC/Ti-6Al-4V samples that were fabricated by a foil-fiber-foil hot-pressing technique, and monitoring the strain at fiber breaks by the acoustic emission technique. Three different fibers were used to evaluate the effect of different interfaces on fragmentation behavior: they were SCS-0 ("strong" interface), SCS-6 ("medium" strength), and Trimarc ("weak"), the first two being made by Textron, and the last one fabricated by Amercom. The interface categories are based on measured normal and shear (from push-out tests) strengths of the interfaces, and are available in published and submitted papers. The final fragment length distribution was determined both by the ultrasonic shear-wave back reflection technique (SBR), and by etching away of the matrix.

It was clear at the very beginning that the simple critical length approach was unable to provide information on the interface friction stress. Therefore, emphasis was focused on two essentially independent sets of experimental data: namely, the stress at each fiber break, and the distribution of fragment lengths. These were then analyzed using Curtin's exact model of fiber fragmentation [25], and also by using an indigenously developed Fiber-Link software [8]. Results showed that the friction stress determined from the fragmentation test was much higher (3-5 times) than from push-out tests, although the different fibers followed the same relative ranking as in push-out tests. A possible reason for the high friction stress in the fragmentation

test is radial constriction of the fiber at locations of breaks by the surrounding plastically deforming matrix, and this has important consequences on local versus global load sharing behavior in high volume fraction composites. The fragmentation test also provided *in situ* Weibull strength and Weibull modulus of fibers that were lower than for extracted fibers, a possible reason being damage of the reaction-zone, carbon-rich interface, and the fiber as the sample was strained to high strains (4-10%). Overall, the fragmentation test shows that the mechanism of shear failure of the interface adjacent to a fiber break is far more complicated than the often-used shear-lag scenario, and that matrix plasticity plays a critical role on local stress conditions. In fact, matrix plasticity can overshadow interface effects, as was observed in multiple-fiber single-ply specimens tested at room temperature, and which will be discussed later in the context of local versus global load sharing behavior in composites. Refer to [Publications 4-12] for additional details about this research.

3.1.1.3 The Slice Compression Test

This test was investigated because of its apparent simplicity in obtaining an average shear strength of the interface, which could then be used to rank different interfaces. The test essentially involves indenting a slice of the composite (sectioned perpendicular to the fiber axis) on to a soft material such as brass. The modulus difference between the fiber and the matrix sets up shear stresses that are able to break the interface, and this is evidenced by the fiber protruding out of the composite and fiber impressions left on the brass. The extent of the protrusions and brass impressions can then be used to arrive at an "average" shear strength, more appropriately an interface friction stress.

The slice compression test was performed on SiC/Ti-6Al-4V composites using different fibers: SCS-0, SCS-6, and Trimarc. While the test provided shear strengths that were in general agreement with friction stresses interpreted from push-out tests, the experiments were greatly hampered by alignment difficulties and, consequently, there was a large scatter in the friction

stress data. Because of this difficulty, the slice compression test does not appear to have any advantage over the better controlled push-out test, and it was discontinued part way through the program. Refer to [Publications 13] for additional details.

3.1.1.4 Damage Assessment in MMCs Using Ultrasonic NDE

The objective of this work, which was a cooperative effort between UES staff and the Materials Directorate NDE group (P. Karpur and T. Matikas of UDRI), was to determine the applicability of ultrasonic NDE for detecting consolidation defects in MMCs, and for detecting damage in the form of fiber cracks and normal interface debonding arising from mechanical loading. Two different ultrasonic techniques using shear wave and longitudinal wave interrogations were applied to study the consolidation and interface damage characteristics of SiC/Ti-alloy composites. In particular, the shear back reflection (SBR) technique was found to be excellent for detecting consolidation problems around fibers, and for detecting fiber break locations. The methodology that was developed has been immensely beneficial for analyzing fiber fragmentation behavior in single-fiber composites, and for assessing local load sharing behavior in single-ply composites. Further work has shown that this ultrasonic technique is generic and is applicable to ceramic matrix composites as well. The ultrasonic technique has also been used for measuring shear stiffness of fiber-matrix interfaces. Refer to [Publications 5,9,14,15] for additional details of this research.

3.1.1.5 Normal Strength Characterization of the Interface

In collaboration with the Government scientists and visiting scientists at WL/MLLM a cruciform/cross specimen geometry was designed to determine the normal (transverse) strength of the fiber-matrix interface. This specimen geometry was designed because the conventional uniform-width transverse [90°] specimen suffers from stress-singularity and stress reversals near free surfaces, which can provide erroneous values of interface normal strength. In the

cross/cruciform geometry, the arms of the cross prevent loading of the interface near the free surface. Also, the geometry preserves a reasonably uniform stress over the central section, as was shown by analytical modeling of a fiberless specimen using an Airy stress-function approach. Single-fiber and multiple-fiber single-ply specimens have been extensively tested and analyzed by D. Gundel (visiting scientist at the Materials Directorate), while UES's contribution, in collaboration with the Government scientists and visiting scientists at WL/MLLM, has been the novel specimen geometry, stress analysis, and evaluation of multi-fiber multi-ply specimens. As indicated earlier, a major advantage of single-fiber specimens for evaluating interface normal strength is that new interfaces can be studied by using only small amounts of coated fibers.

FEM analysis was performed to determine the stress distributions in uniform-width and cruciform-shaped single-fiber specimens. It was shown that during transverse testing, there exists a singularity due to the applied load at the interface (near the free edges) in the uniform-width specimen and that it is absent for the cruciform geometry. This allows a bond strength to be determined from the cruciform geometry, provided there is a good estimate of the radial residual stress on the fiber. The ratios of critical length parameters in the specimen geometry was shown to be sufficient in producing uniform stresses in the direction of the applied stress over a large portion of the interface in the loading region before debonding initiated. The cruciform geometry has shown interface normal bond strengths of around 350 MPa, 100 MPa, and 10-30 MPa for SCS-0, SCS-6, and Trimarc fibers, respectively, in SiC/Ti-6Al-4V composites. The interface bond strength in multi-ply Sigma SiC/Ti-6242 was assessed to be less than 30 MPa. Refer to [Publications 3,16-21] for additional details of this research.

3.1.1.6 Failure Mechanisms During Transverse Loading and Development of the Torsion Test for Tangential Shear Strength Determination

Finite element computations showed that during transverse [90°] loading of unidirectional composites, significant tangential shear stresses are set up at the fiber-matrix interface at locations of ~ 45° from the axis of loading. Depending upon the properties of the interface, these

stresses may be large enough to initiate an interface tangential shear crack at those locations, followed by propagation of the shear crack along the fiber circumference towards the poles (zero degree to the loading axis) of the fiber. These unit processes can occur before normal separation between the fiber and the matrix (normal debond) at the poles of the fiber. The FEM analysis showed that the effect of shear failure of the interface prior to normal debonding is equivalent to a higher stress concentration at the poles, where the latter is defined as the ratio of the local normal stress at the interface at the poles to the far-field applied stress. Thus, the stress concentration can increase from 1.3 for a non-slipping interface in the SiC/Ti-alloy system to ~ 1.7 for an easily slipping (friction coefficient of 0.05) interface, suggesting that a higher tangential strength and friction coefficient would be beneficial for composite transverse properties.

Because of the above importance of tangential interface failure prior to normal debonding, a torsion test technique was developed by UES staff to determine the tangential shear strength of several SiC/Ti alloy interfaces. In this test, a single-fiber MMC specimen is torqued about the axis of the fiber, and the torque-versus-angle-of-twist curve is analyzed for determining initiation of the tangential interface crack and its subsequent propagation characteristics. Tangential shear strengths for different SiC/Ti-6Al-4V interfaces were determined from experimental results of the torsion tests, coupled with analytical fracture mechanics and stress analysis using FEM. Based on those results, it was deduced that during transverse [90°] loading of SCS-6/Ti alloy and Trimarc/Ti-6Al-4V systems, interface failure due to tangential shear stresses precede normal interface separation. Refer to [Publications 22-24] for more details.

3.1.1.7 Interface Effects on Load Sharing Behavior Under Longitudinal Tension

The study is important because there is an engineering need for improving the transverse strength of composites, and an attractive approach (possibly the only one available) is to increase the normal interface strength. Since increased interface strength can be at the expense of

longitudinal strength, there is a need to assess how interface strength affects the longitudinal strength of the composite.

In the absence of a matrix crack, the influence of the interface is only felt when a fiber fracture occurs. If failure of one fiber leads to successive failures of adjacent fibers, the failure mechanism is termed local load sharing (LLS). On the other hand, if adjacent fibers are not stressed to any greater extent than fibers that are far away, then fibers can fail randomly in the composite before unstable failure of the specimen. This mode of failure is termed global load sharing (GLS), and it allows better utilization of fiber strength than LLS. Conventional wisdom has been that weak interfaces allow significant fiber-matrix sliding adjacent to a fiber break, so that GLS will occur, and Curtin's GLS model [25] has been used in the literature for modeling the longitudinal strength of TMCs. Unfortunately, our experience has been that GLS is absent even for reasonably weak interfaces (SCS-6 fibers in Ti-alloy matrices), this being interpreted from negligible number (less than 10) of fiber breaks away from the fracture location in a multi-ply SCS-6/Ti-25Al-17Nb TMC [26]. A similar absence of GLS was noted in the study of a SCS-6/Ti-1100 TMC [27].

The overall approach in assessing the effect of interfaces on LLS versus GLS behavior involved fabrication of single-ply specimens with different fibers (SCS-0, SCS-6, and Trimarc), and hence different interfaces, in a Ti-6Al-4V matrix. Tensile tests were coupled with acoustic emission monitoring of fiber breaks, and the mechanical test data were compared with single fiber fragmentation tests to evaluate interaction between breaks in adjacent fibers. The tests were also accompanied with observations of macroscopic slip bands on specimen faces, and fiber break locations determined by the ultrasonic SBR technique. The center-to-center fiber spacing was varied from ~ 10 fiber diameters to ~ 1.5 , the latter being representative of 30 vol.% composites. Results showed that LLS behavior occurred in all composites, independent of the interface strength and fiber spacing. However, LLS did not occur in the form of coplanar cracks in adjacent fibers, as is conventionally conceptualized. Rather, LLS occurred through the development of

intense slip bands (at $\sim 45^\circ$ to the fiber axis) from the tips of a broken fiber, their impingement on the adjacent fiber, and subsequent failure of that fiber at that location. The net effect was a criss-cross arrangement of fiber breaks in the center region of the gage length of the sample. Such slip bands are believed to be the manifestation of local plastic instabilities, since they do not occur in the Ti-6Al-4V fiberless "neat" material that is processed identically to the composites. More importantly, the experiments and analyses suggest that matrix plasticity may actually play a more dominant effect on LLS versus GLS behavior than the interface. From an interface development perspective, the conclusion is that the penalty on longitudinal strength in going to stronger interfaces may not be significant, provided that the fiber strength itself is not compromised in achieving a higher bond strength of the interface. Refer to [Publications 1,2,28,29] for additional details.

3.1.1.8 Interface Effects on Fatigue Crack Growth

This investigation was considered important since there has been no systematic study of the influence of interface properties on the fatigue crack growth (FCG) response in MMCs. In particular, the need for stronger transverse strength of interfaces required assessment of how such interface modification might influence damage tolerance in the longitudinal direction, measured in terms of the FCG response, of the composite.

Single-ply multi fiber composite specimens with varying interfaces, uncoated SiC fiber (SCS-0), graded carbon/silicon-rich coated (SCS-6), carbon coated (Trimarc) fiber-reinforced Ti-6Al-4V matrix, were fabricated. A single-edge-notched-tension (SENT) geometry of 25.4 mm width and 2 mm starter notch was utilized in the FCG experiments, where the fibers (with a center-to-center spacing of 1.5 fiber diameters) were aligned along the loading direction and occupied only the central 8 mm of the panel. Thus, the crack growth kinetics could be studied, starting with the crack growing in the pure matrix material, followed by transients as the crack approached the central band of fibers, and finally the slowdown of the crack caused by fiber

bridging and/or elastic shielding depending on the interface and fiber strength characteristics. Experiments showed that as the crack in the matrix approached the central band of fibers, the fatigue crack growth rates for all the three composites were lower than that of the "neat" material. This decrease in the crack growth rate is believed to be due to shielding through elastic mismatch effects, an aspect that has not received sufficient attention to date. It was also very significant that the composite with the largest bond strength (i.e., with SCS-0 fibers) showed the largest slowdown of the crack as the first fiber was approached (conversely Trimarc fibers showed the least slowdown), suggesting that weaker interfaces are less efficient in providing elastic shielding through modulus mismatch. Fiber bridging and arrest of the fatigue crack was observed at moderate applied stress ranges (R-ratio was 0.1) for SCS-6 and Trimarc fibers. For the same stress ranges, SCS-0 fibers exhibited attempts at crack bridging, followed by loss of bridging. However, at a low enough stress level, crack bridging and crack arrest was also observed for SCS-0 fibers. This behavior is significant, since the interface toughness for this system is believed to be similar to the fiber toughness, which would make crack bridging unlikely based on the He and Hutchinson criterion [30].

Micrographs of the polished as well as etched specimens of SCS-6 and Trimarc fibers showed interface damage and debonding ahead of the crack tip. Debonding was also observed for SCS-0 fibers, although the length of debond was extremely small. The normal interface separation criterion, as proposed by Gupta, Argon, and Suo [31], appeared to be consistent with debonding behavior for all the composites. In addition, interface shear failure ahead of the crack tip was proposed for the weak interfaces. Analyses was based on normal interface strength from the cruciform test, interface friction stress from the push-out test, fiber strength data from extracted fibers, and estimates of residual stresses in the composites. Refer to [Publications 32,33] for additional details.

3.1.1.9 Interface Development for the Sapphire/Gamma-TiAl System Using Ductile and Barrier Metallic Layers

This research was an initial attempt at developing interfaces in TMCs. Gamma TiAl was considered as the matrix, since there were early interests at reinforcing the alloy for improved modulus and creep resistance. Because of thermal mismatch problems, sapphire fibers (~125 μm diameter, made by Saphikon) was selected as the reinforcing material.

It was evident at the very beginning of the program that uncoated sapphire would be unusable, since titanium reacts strongly with alumina thereby reducing the strength of sapphire fibers. Hence a coating system had to be developed. The system selected was an initial (0.5 - 1 μm thick) coating of Nb on the fiber, followed by a Y coating (0.5 - 1 μm thick), and then an overcoat of Nb/Ti to protect the inner coatings from oxygen intake and damage during handling. Nb was selected because of its good wetting and compatibility with alumina (epitaxy has been documented for this system) without any significant reaction, and also because it is a soft ductile layer that would prevent cracks in the matrix from propagating into the fiber. Also, the good bonding characteristic between sapphire and Nb would provide good normal interface strength and hence better transverse properties for the MMC. In the presence of a matrix crack under longitudinal loading, normal separation was predicted ahead of the crack tip based on Gupta et al. criterion [31]. Y was selected as a barrier layer, since phase diagrams show extremely little solubility between either Nb and Y or between Y and Ti, at temperatures up to 1300°C. This would ensure no outward diffusion of Nb into the Ti-alloy matrix, or any ingress of Ti that would damage the fiber through reactions. Experiments showed that the coating system was effective in achieving the desired purposes. However, the composite suffered from damaged fibers that were believed to be largely due to kinks in the single crystal fibers that cracked during consolidation. Although additional improvements could be made, the research was discontinued because of lack of interest in gamma TiAl based MMCs. Also, based on our studies of SiC/Ti-alloy systems, a minimum level of elongation (order of 3-5%) is needed for the matrix for realizing the strength potential of fibers. Otherwise, high strains in the matrix surrounding a

broken fiber can set up LLS conditions, and the best utilization of the fiber will be limited to the stress corresponding to the first random fiber break [34]. Overall, the concept of ductile and stable barrier layers is a very important one, and similar approaches are being tried for SiC/Ti-alloy systems with more ductile matrices. Refer to [Publications 35] for additional details.

3.1.2 ORTHORHOMBIC TITANIUM ALUMINIDE MATRIX BEHAVIOR AND DEVELOPMENT

The orthorhombic titanium aluminide alloys cover a wide range of compositions: Ti- (21-29)Al- (15-30)Nb, all in atomic percent, and typically exhibit either (α_2 +O+B2) three-phase or (O+B2) two-phase microstructures depending on the alloy composition, interstitial content and processing. Alloys in this class were selected for investigation as matrix alloys in TMCs because the previous generation Ti-24Al-11Nb (α_2 + β) alloys did not possess the required combination of creep resistance and room temperature ductility, and composites based on the alloys suffered from extremely poor thermal cycling resistance. Among the orthorhombic alloys, the Ti-22Al-23Nb composition has been investigated rather extensively, and thermal cycling tests have shown that the composite is resistant to cracking during thermal cycling. The presence of the orthorhombic (O) phase, based on the Ti_2AlNb composition, provides improved creep resistance due to ternary ordering of Ti and Nb atoms, and this is also accompanied with increased number of slip systems at room temperature, a double benefit. Further, carbon diffusion from the SiC fiber is less effective in forming a B2 depleted low-ductility zone around the fiber, compared with significant β depleted zones in α_2 + β alloys.

In this program, alloys of nominal composition Ti-22Al-23Nb, Ti-25Al-17Nb, and Ti-25Al-17Nb-1Mo, were studied in reasonable detail. Of significance is that quaternary additions of Mo have shown substantial improvements in high temperature strength and creep resistance, and the reasons are still under investigation. Microstructure-property relationships of the different alloys have provided valuable insight into alloying effects, deformation mechanisms, and

texture effects, and have guided processing and heat treatments for optimization of matrix properties. In addition to alloys in the sheet form, fiberless "neat" material and composites with SCS-6 fibers were investigated, and they illustrate that interstitials (carbon and oxygen) can cause significant differences in microstructures (hence properties) of sheet, neat, and composite materials in the same heat treatment condition. The effects of texture on matrix and composite properties have also been investigated. More recently, research was initiated on the two phase (O+B2) alloys, because of some microstructural instabilities observed in the α_2 phase of the three phase alloys. Also, feasibility studies were undertaken for oxidation protection of orthorhombic alloys using a functionally graded layer approach.

3.1.2.1 Effect of Matrix Texture on MMC Processing and Mechanical Properties

The effects of matrix alloy texture on the tensile behavior of a SiC/Ti-24.5Al-17Nb-1Mo composite, processed by the foil-fiber-foil technique, was studied by mechanical testing, microstructural characterization and pole figure analysis. The Ti-24.5Al-17Nb-1Mo unreinforced matrix alloy displayed a pronounced microstructural texture with elongated α_2 grains and (O+ β_o) regions parallel to the rolling (longitudinal) direction of the alloy foils used for consolidation. Crystallographic texture analysis using pole figure measurements revealed that the α_2 phase in the Ti-24.5Al-17Nb-1Mo unreinforced matrix panel is strongly textured ($\sim 11X$ random) with the hexagonal unit cells lying in the plane of the panel with their first order prism planes at $\pm 30^\circ$ with the plane of the panel and their c axis aligned with the transverse direction of the panel. The crystallographic textures of O and β_o phases were less pronounced. The tensile properties of unreinforced Ti-24.5Al-17Nb-1Mo matrix were observed to be anisotropic, with a high ductility in the longitudinal direction and poor ductility in the transverse direction. This anisotropic tensile behavior may be explained on the basis of the texture of the α_2 phase alone. With the aforementioned texture, multiple slip systems of α_2 phase can operate under longitudinal loading and give rise to the ductility observed in this direction. However, there is a

lack of availability of slip systems under transverse loading conditions. This explains the essentially elastic behavior of the alloy in the transverse direction at RT and moderately higher temperatures.

In spite of the high ductility of the alloy in the longitudinal direction, the Ti-24.5Al-17Nb-1Mo/SCS-6 [0]₄ composite specimens exhibited poor properties with low values of strain to failure (< 0.8%) and tensile strength (< 1200 MPa). These poor properties were attributed to damage in the composite following consolidation, arising from matrix anisotropy. As-consolidated composite panels showed radial cracks at the reaction zone and adjoining α_2 grains. These cracks appear to arise from a lack of accommodation of residual hoop stresses following processing which is a consequence of lack of plasticity in the transverse direction. Tensile loading of the [0]₄ composite specimens resulted in crack growth in the matrix between adjacent fiber plies as well as along the bond lines of the foils. Fiber/matrix interfacial debonding stemming from the matrix cracks also contributed to damage at the higher test temperatures. The results demonstrated that both processing and mechanical behavior of this MMC are markedly affected by matrix anisotropy. Refer to [Publications 36-38] for additional details.

3.1.2.2 Optimization of Ti-22Al-23Nb Matrix using Heat Treatments

Research on "O" alloys with (α_2 +O+B2) three-phase microstructures has shown that the creep resistance is improved by increasing the volume fraction of the O phase or by decreasing the volume fraction of the α_2 phase. The role of morphology of the phases requires further investigation. Nevertheless, our heat treatment work on Ti-22Al-23Nb/SCS-6 has shown that improvements in MMC properties are possible through an understanding of the heat treatment response of neat matrix. For example, a sub-transus heat treatment followed by rapid cooling (28°C/min) and aging did not have a significant effect on RT tensile and 65°C creep properties of [0]₄ and [90]₄ MMC specimens. In contrast, a supra-transus heat treatment followed by similar

cooling and aging resulted in markedly improved creep properties of [90]₄ MMC at 650°C, with an order of magnitude improvement in the time to 0.4 % strain and > 2X increase in creep rupture life. The supra-transus heat treatment did not affect the RT tensile properties of [0]₄ and [90]₄ MMC specimens. Similarly, 650°C creep properties of [0]₄ MMC specimens were unaffected. Refer to [Publications 39] for additional details.

3.1.2.3 Role of Carbon Diffusion During Processing of TMCs

In agreement with known diffusivity data, our work has shown that carbon present in the coating of SiC fiber diffuses over a significant distance (relative to fiber diameter) into the Ti alloy matrix during MMC processing. The dissolution of carbon in various Ti alloy matrices was explained on the basis of the peritectoid transformation $\beta + \text{TiC} = \alpha$ arising from differences in the interstitial void radii of the phases. Further, it was demonstrated that significant differences can arise in the heat treatment response of MMC and neat specimens due to the interstitial carbon, and that carbides can form even under certain sub-transus heat treatments. Accordingly, a detailed study of the effects of interstitial carbon on the phase stability, transformation kinetics and mechanical properties of the matrix alloys is currently underway. Refer to [Publications 39] for additional details.

3.1.2.4 Analysis of SCS-6 Fibers by Fourier Transform Infrared (FTIR) Spectroscopy

Previous studies dealing with the analysis of the oxygen content of the SCS-6 SiC fiber reported contradictory results. One of these studies, involving scanning Auger spectroscopy, reported the presence of high levels of oxygen (> 10 at.%) in the bulk of this fiber, presumably in the form of SiO₂. Based on this data, it was suggested that the outward diffusion of oxygen from the fiber into the surrounding titanium may contribute to increased hardness and embrittlement of the titanium alloy matrix and can have deleterious effects on composite properties. A subsequent evaluation of this fiber using Auger spectroscopy and neutron activation analysis (NAA)

disputed these results and the NAA data showed that the bulk oxygen content of the SCS-6 fiber is quite low (~ 0.12 at.%). This latter study concluded that the previously observed high oxygen levels were artifacts probably due to inadequate vacuum and specimen contamination during scanning Auger analysis.

The objective of the present work was to determine the amount of SiO_2 , if any, in the SCS-6 silicon carbide fibers by using the FTIR spectroscopy technique. The SiO_2 absorption at 1090 cm^{-1} and the SiC absorption at 790 cm^{-1} are sufficiently far apart and, therefore, each band area can be measured in the presence of the other. Fiber samples from two different lots produced in 1990 and 1994 were separately analyzed. The infrared spectra were recorded on a FTIR model AQS-20M Analect spectrometer equipped with KBr beam splitter and mercury cadmium telluride detector at a resolution of 4 cm^{-1} with 200 interferograms co-added for each spectrum. The spectral range covered was 4000 to 500 cm^{-1} for KBr pellets and 4000 to 750 cm^{-1} for microscope spectra using an AQM-515 microscope module. The spectral analysis did not provide any evidence for the presence of a significant amount of SiO_2 in the SCS-6 silicon carbide fiber samples. This observation is consistent with the results of previous neutron activation analysis work, which showed that the amount of oxygen present in this fiber is quite small. Refer to [Publications 40] for additional details.

3.1.2.5 Oxidation Resistance and Protection from Environmental Embrittlement

Current ternary as well as second generation orthorhombic alloys are susceptible to interstitial embrittlement at temperatures $< 600^\circ\text{C}$ in air. Thus, there is a need for environmental protection in the range 650°C - 700°C , anticipated in engine applications. Preliminary work was performed to determine the feasibility of protecting the orthorhombic titanium aluminide alloys from environmental attack using functionally graded material (FGM) layers. The fundamental mechanics and chemistry issues will be explored further. In this effort, sheets of a γ -alloy (Ti-48Al-2Nb-2Cr) were vacuum hot pressed on either side of a Ti-22Al-23Nb O-alloy. The

interface between the two materials contained Nb-rich α_2 phase ranging up to about 10 μm in thickness. Finite element analysis indicated a tensile residual stress of about 200 MPa in the γ layer, and this had substantial influence on strain-to-failure of the entire sandwich. Based on the FEM analysis, it is theorized that a spatially varied interlayer of a compliant material and the γ -alloy may have potential in mitigating the environmental protection issue of orthorhombic alloys. Refer to [Publications 41] for additional details.

3.1.2.6 Structure-Property Relationship in Orthorhombic Alloys

The microstructure-property relations and the deformation mechanisms were studied for the nominal Ti-25Al-17Nb and Ti-25Al-17Nb-1Mo alloys. These are three-phase ($\text{O}+\alpha_2+\text{B}_2$) alloys, and the phase volume fractions can be controlled by solutionizing at different temperatures in the two-phase ($\alpha_2+\text{B}_2$) field, followed by aging at different temperatures and times to control volume fraction and size of O-phase precipitates (lenticular morphology). The phase evolution was studied, and it was followed by mechanical tests at room and elevated temperatures to understand the deformation mechanisms in each phase and their combined effects on the bulk mechanical properties. It was shown that the B2 phase has wavy slip characteristics, and is able to blunt micro-cracks. This phase also exhibited dimple failure characteristics. The α_2 phase exhibited planar slip, although it did seem to possess sufficient ductility. Because of the lack of $\langle c+a \rangle$ slip, stress concentrations occur at α_2/α_2 grain boundaries, which was manifested in the form of cracking at those boundaries. The O phase was more crack resistant, although it too exhibited planar slip behavior. Intervening B2 lamellar regions between adjacent O laths played an important role in reducing stress concentrations from such planar slip arrays.

High temperature tensile tests and creep studies showed that the creep resistance of the alloys increase with volume fraction of the O phase and decrease with the volume fraction of the α_2 and B2 phases. However, there is a morphological effect of the phases as well, which was not

studied in sufficient detail in this work. The fatigue crack growth resistance of Ti-25Al-17Nb also increased with the volume fraction of the O laths. The fracture surface was very rough, suggestive of a tortuous crack path. On the other hand, the α_2 +B2 microstructure yielded a flat fracture surface, and its FCG resistance was poorer in spite of slightly higher ductility.

The same heat treatment did not produce identical microstructures in the sheet, neat, and MMC specimens due to different levels of interstitials (carbon and oxygen). Thus, it was determined that careful attention should be focused on this issue when devising heat treatments for microstructural and MMC strength improvements. In particular, carbon pickup from the fiber needs to be reduced. Refer to [Publications 36-38,42-45] for additional details.

3.1.2.7 Phase Evolution and Structure-Property Relations in Ti-25Al-25Nb

The phase evolution, room temperature tension, and elevated temperature creep of the intermetallic alloy, Ti-25Al-25Nb, were studied as a function of processing and heat treatment. Super-transus processed and heat treated microstructures suffered from intergranular attack and exhibited low ductility. Sub-transus processing and heat treatment resulted in the best combination of room and elevated temperature properties. Fully O microstructures suffered from poor RT ductility due to insufficient number of active slip systems. High stress concentration at O/O grain boundaries served as preferential crack nucleation sites, which was similar to α_2/α_2 boundaries in the three-phase alloys. Microstructures containing a significant amount of B2 phase sandwiched between adjacent O grains reduced O/O cracking and yielded excellent elongations and strength. This is believed to be a result of the slip compatibility between the O and B2 phases, and wavy slip characteristics of the B2 phase. At 650°C, the O-phase provided excellent creep resistance. Phase instability in the form of O-phase precipitation in prior B2 regions were observed in the creep samples. However, the kinetics were not significantly different than a sample exposed to 650°C without load, and suggested that phase stabilization was necessary before the alloy could be used. The time required for stabilization at

650°C was estimated to be less than 100 hours. The morphology of the O-phase consisted of both equiaxed primary O grains, and O laths that grew in prior B2 grains. The relative amounts of these two O-phase morphologies could be controlled, and recent tests suggest that lath morphology has better creep resistance than the equiaxed O phase. However, additional tests are in progress to confirm these initial findings. Refer to [Publications 46] for more details.

3.1.3 COMPOSITE PERFORMANCE

Some of the work relating to effects of the constituents on bulk composite properties have already been presented in the previous sections. In this section, three different activities are described. The first relates to the effect of heat treatment on tensile strength and fiber strength utilization in a SCS-6/Ti-25Al-17Nb composite. The second section concerns modification of the ADDA software for local strain measurements in composites. The third section deals with deformation mechanisms and fracture behavior of discontinuous particulate reinforced aluminum alloy composites, usually termed as DRAs.

3.1.3.1 Tensile Behavior of SCS-6/Ti-24.5Al-17Nb and SCS-6/Ti-24.5Al-17Nb-1Mo Composites, and Issues of Fiber Strength Utilization

Tensile testing of this composite at different temperatures in the range 25°C-760°C showed that the strength levels were less than 80% of the values predicted on the basis of rule-of-mixtures. In the as-consolidated condition, the unreinforced Ti-24.5Al-17Nb matrix exhibited limited ductility (< 1.35%) at room temperature. Metallographic sectioning of tensile specimens following testing showed a number of cracks at α_2/α_2 grain boundaries due to stress concentration arising at adjoining α_2 grains. It was suggested that the lower strength of the composite at RT stems from incomplete loading of the fibers as a result of the low ductility of the matrix. Further, the lower strength values of the composite at higher temperatures (593°C-760°C) were explained in terms of surface cracking and interstitial embrittlement of this matrix

alloy. This was also consistent with the results of thermal fatigue and thermomechanical fatigue tests which showed severe cracking of the Ti-24.5Al-17Nb/SCS-6 composite and indicated that this matrix is only marginally better than the Ti-24Al-11Nb matrix in its resistance to interstitial embrittlement and cracking.

Sub-transus heat treatment of the Ti-24.5Al-17Nb neat matrix at 1050°C (which is above the consolidation temperature of 940°C) resulted in the precipitation of β_0 phase at a number of α_2/α_2 grain boundaries. Subsequent aging at 850°C caused the precipitation of orthorhombic phase at α_2/β_0 interfaces. The heat treated neat material exhibited greater than 4% tensile elongation at room temperature. This represents a significant improvement over the as-consolidated matrix which showed elongation values of ~1.3% at RT, and this improvement is believed to be due to elimination of α_2/α_2 boundaries.

SCS-6/Ti-25Al-17Nb specimens that were also heat treated at 1050°C exhibited significant improvements in longitudinal strength, compared with the as-received material. Since the matrix strength was not increased by the heat treatment, it is believed that the higher strength of the heat-treated MMC illustrates the important role of matrix ductility on strength utilization of fibers. Modeling showed that a model based on the fiber stress required to form the first random fiber break provided MMC strength that agreed with the as-received composite. On the other hand, the fiber stress required to form a cluster of two breaks provided MMC strength that agreed with the strength of the heat treated specimens. This second model is contingent on stress concentration effects, and etching away of the entire matrix showed less than 10 random fiber breaks in the sample away from the fracture plane. Thus, even with adequate ductility, local load sharing (LLS) appears to dominate room temperature composite strength, compared with global load sharing (GLS) characteristics. This finding is similar to what was observed in the single-ply SiC/Ti-6Al-4V samples that were studied under the interface activity.

The 90-degree MMC did not provide any significant strength enhancement through heat treatment. A principal reason was the presence of an α_2 enriched zone, likely because of carbon pickup. A Nb coating on the fiber helped to retain the O and B2 phases around the fiber, and this did provide modest improvements in the strength and ductility of the 90-degree MMC. Refer to [Publications 26,36,37] for more details.

3.1.3.2 ADDA Software for Local Strain Measurements in Composites

This automatic digital deformation analysis (ADDA) software was improved to allow local strain measurements in any system. The technique of strain measurement relies on digital images of grids that are deposited on the specimen prior to loading, and the software compares successive digitally recorded images (at different points of loading). The major advantages of the software are: (1) it is automatic, and (2) it has high precision, with the strain resolution being limited by that of the imaging system (e.g., errors in optics, etc.). The analysis is automatic, in that the unit recognizing feature (e.g., intersection between grid lines) has to be initially identified, and the software then determines all other such features and compares the distance between corresponding features in subsequent images. The improved version of the software was successfully used by WL/MLLM for measuring local strains around fibers under transverse loading. Refer to [Publications 47] for more details.

3.1.3.3 Fracture and Deformation Mechanisms in Discontinuously Reinforced Aluminum (DRAs)

This research was initiated in 1995 because of the perceived need to improve the fracture toughness of DRAs, without incurring significant loss of tensile strength. The materials considered were 2xxx and 7xxx series alloys reinforced with SiC particulates, and heat treated to the underaged, peak-aged and over-aged conditions. The emphasis of the research was on the micro mechanisms of damage and fracture, so that routes could be developed for improved toughness-strength combinations based on intrinsic and extrinsic mechanisms of toughening.

Much of the experimental effort of the program has been conducted by A. Panday (visiting scientist at the Materials Directorate), and UES has been involved with fracture mechanics calculations and evaluating and modeling the mechanisms of particle/interface damage and local matrix plasticity.

Results show that although particle fracture is dominant in the peak aged condition, particle fracture and interface debonding damage occur in significant amounts in the other heat treated conditions. Rather, the effect of heat treatment on fracture toughness can best be rationalized in terms of flow localization behavior. Thus, in the peak aged condition, a particle fracture leads to sharp slip bands that impinge on the adjacent particle which then cracks, and so on. The net effect is a series of particles in a narrow band that are connected by a highly plastically deformed matrix, and thereby a low fracture toughness value is obtained. A manifestation of this is that damage in a smooth tensile sample is limited to an extremely small region of the gage length. At the other extreme, in the solution treated condition, although particle fracture and interface debonding lead to local matrix plasticity, those bands are sufficiently diffused by the time they arrive at the adjacent particle. Thus, damage is spread out over a large region ahead of the crack tip, and the resultant greater plastic energy dissipation leads to higher fracture toughness. In a smooth tensile sample, this mechanism manifests as a deformed and damaged region that occupies the entire gage length. Thus, any approach that would prevent sharp slip bands originating from cracked/debonded particles from propagating into the matrix and on to the adjacent particle, would be beneficial for improving the toughness of DRAs. Refer to [Publications 48-50] for additional details.

3.4 SUMMARY OF CURRENT WORK NOT REPORTED

Continued work on interfaces and matrix alloys include the following:

- (1) Developing interface systems which provide improved transverse bond strength, but which do not degrade fiber strength by any appreciable amount.
- (2) Obtaining improved understanding of the effect of interfaces on longitudinal strength and fatigue crack growth resistance. The interfaces that are being investigated include the existing carbon-based interfaces, and those that are synthesized under the current research program.
- (3) Developing improved understanding of the effects of matrix texture on composite response, for orthorhombic Ti-alloy based composites.
- (4) Developing heat treatments and processing routes for orthorhombic alloys for optimized TMC performance.
- (5) Evaluating effects of matrix chemistry, processing route, and heat treatments on room temperature ductility and creep resistance of two-phase (O+B2) alloys.

3.5 PUBLICATIONS

1. I. Roman, S. Krishnamurthy, and D. B. Miracle, "Fiber-Matrix Interfacial Behavior in SiC-Titanium Alloy Composites," in Titanium '92: Science and Technology, Eds., F. H. Froes and I. L. Caplan, TMS, Warrendale, PA, pp. 2545-2551 (1993).
2. P. Karpur, T. E. Matikas, S. Krishnamurthy, and N. Ashbaugh, "Ultrasound for Fiber Fragmentation Size Determination to Characterize Load Transfer Behavior of Matrix-Fiber Interface in Metal Matrix Composites," in Review of Progress in Quantitative Nondestructive Evaluation, 12B, Eds., D. O. Thompson and D. E. Chimenti, Plenum Press, New York, pp. 1507-1513 (1993).
3. D. B. Miracle, B. S. Majumdar, S. Krishnamurthy, and M. Waterbury, "The Influence of Matrix Deformation on Tensile Behavior in Metal Matrix Composites," Proceedings of Ninth International Conference on Composite Materials, ICCM 9, Ed. A. Miravate, 1, pp. 610-624 (1993).

4. G. N. Frantziskonis, P. Karpur, T. E. Matikas, S. Krishnamurthy, and P. D. Jero, "Fiber Matrix Interface - Information from Experiments via Simulation," *Comp. Struct.*, 29(3), 231-247 (1994).
5. M. C. Waterbury, P. Karpur, T. E. Matikas, S. Krishnamurthy, and D. B. Miracle, "In Situ Observation of the Single-Fiber Fragmentation Process in Metal-Matrix Composites by Ultrasonic Imaging," *Composite Science and Technology*, 52, 261-266 (1994).
6. M. C. Waterbury and S. Krishnamurthy, "Evaluation of Interfacial and Fiber Properties in Titanium Matrix Composites by Single Fiber Fragmentation Testing," in the Proceedings of the 10th International Conference on Composite Materials, ICCM-10, VI, Eds., A. Poursartip and K. Street, Woodhead Publishing Limited, pp. 431-438 (1995).
7. P. Karpur, T. E. Matikas, and S. Krishnamurthy, "Ultrasonic Characterization of the Fiber-Matrix Interphase/Interface for Mechanics of Continuous Fiber Reinforced Metal Matrix and Ceramic Matrix Composites," *Composites Engineering*, 5(6), 697-711 (1995).
8. P. Karpur, T. E. Matikas, S. Krishnamurthy, and D. B. Miracle, "Recent Developments in Ultrasonic Methods for Metal Matrix Composites Research," in the Proceedings of the 10th International Conference on Composite Materials, ICCM-10, V, Eds., A. Poursartip and K. Street, Woodhead Publishing Limited, 479-486 (1995).
9. B. S. Majumdar and D. B. Miracle, "Interface Measurements and Applications in Fiber-Reinforced MMCs," *Key Eng. Mater.*, 116-117, 153-172 (1996).
10. B. S. Majumdar and S. G. Warrier, "Fracture Mechanics of the Push-Out Test and Results for Titanium Matrix Composites," presented at the 1996 TMS Fall Symposium on Interfaces at Cincinnati, OH, and two-part papers with D. B. Miracle as co-author to be submitted to *Acta Metall.* (November 1996).
11. S. Krishnamurthy, T. E. Matikas, and P. Karpur, "Role of Matrix Microstructure in the Ultrasonic Characterization of Metal Matrix Composites," *J. Mater. Res.*, 12(3), 754-763 (1996).
12. B. S. Majumdar, T. Matikas, and P. Karpur, "Fiber Fragmentation in Single and Multi-Fiber Composites," *Proceedings of the International Conference on Composites Engineering*, ICCE-3, New Orleans, Ed. D. Hui, p. 557 (1996).
13. M. C. Waterbury, D. Tilly, W. Kralik, and D. B. Gundel, "Evaluation of TMC Interface Properties by the Slice Compression Test, *Proceedings of the ICCM-10*, 2, Eds., A. Poursartip and K. Street, pp. 719-726 (1995).

14. S. Krishnamurthy, T. E. Matikas, P. Karpur, and D. B. Miracle, "Ultrasonic Evaluation of the Processing of Fiber-Reinforced Metal Matrix Composites," *Composites Science and Technology*, 54, pp. 161-168 (1995).
15. S. M. Pickard, D. B. Miracle, B. S. Majumdar, K. Kendig, L. Rothenflue, and D. Coker, "An Experimental Study of Residual Fiber Strains in Ti-15-3 Continuous Fiber Composites," *Acta Metall.*, 43(8), 3105-3112 (1995).
16. T. E. Matikas, P. Karpur, S. Krishnamurthy, and R. E. Dutton, "A Nondestructive Approach to Correlate the Interfacial Defects Induced During Processing of MMCs and CMCs with the Consolidation Parameters," *Appl. Comp. Mater.*, 2, 293-311 (1995).
17. D. B. Gundel, B. S. Majumdar, and D. B. Miracle, "Evaluation of the Intrinsic Transverse Response of Fiber-Reinforced Composites Using a Cross-Shaped Sample Geometry," *Scripta Metall. et Mater.*, 33, 2057 (1995).
18. D. B. Gundel, B. S. Majumdar, and D. B. Miracle, "The Intrinsic Transverse Response of Several SiC/Ti-6Al-4V Composites to Transverse Tension," *Proceedings of the ICCM-10*, 2, Eds., A. Poursartip and K. Street, pp. 703-710 (1995).
19. S. G. Warrier, D. B. Gundel, B. S. Majumdar, and D. B. Miracle, "Stress Distribution in a Transversely Loaded Cross-Shaped Single Fiber SCS-6/Ti-6Al-4V Composite," *Scripta Metall. et Mater.*, 34(2), 293 (1995).
20. S. G. Warrier, D. B. Gundel, B. S. Majumdar, and D. B. Miracle, "Interface Effects on Transversely Loaded Single-Fiber SCS-6/Ti-6Al-4V," *Metall. Trans. A*, 27A, 2035 (1996).
21. D. B. Gundel, S. G. Warrier, and D. B. Miracle, "The Interface Debond Stress in Single and Multiple SiC Fiber/Ti-6Al-4V Composite under Transverse Tension," accept for publication, *Acta Metall.* (1996).
22. D. B. Miracle, D. B. Gundel, and S. G. Warrier, "Interfacial Structure and Properties for the Design of Fiber-Reinforced Metal Matrix Composites," to appear in *Processing and Design Issues in High Temperature Materials*, Eds., N. S. Stoloff and R. H. Jones, TMS, Warrendale, PA (1996).
23. S. G. Warrier, B. S. Majumdar, D. B. Gundel, and D. B. Miracle, "Implications of Tangential Shear Stress Induced Failure During Transverse Loading of SiC/Ti-6Al-4V Composites," in press, *Acta Metall.* (1996).

24. S. G. Warrier, B. S. Majumdar, and D. B. Miracle, "Determination of the Tangential Shear Strength of Interfaces and their Impact on Transverse Properties," to be submitted to *Composites Part B: Engineering* (December 1996).
25. S. G. Warrier, B. S. Majumdar, and D. B. Miracle, "Determination of the Interface Failure Mechanism during Transverse Loading of Single Fiber SiC/Ti-6Al-4V Composites from Torsion Tests," *Acta Metall.*, 45(1), 309-320 (1996).
26. C. Boehlert, B. S. Majumdar, S. Krishnamurthy, and D. B. Miracle, "Role of Matrix Microstructure on RT Tensile Properties and Fiber-Strength Utilization of an Orthorhombic Ti-Alloy Based Composite," *Metall. Trans. A*, 28A, 309-323 (1997).
27. B. S. Majumdar, T. Matikas, and D. B. Miracle, "Experiments and Analysis of Fiber Propagation in Single and Multiple Fiber SiC/Ti-6Al-4V Metal Matrix Composites," *J. Comp. B*, in press (1997).
28. D. B. Gundel, B. S. Majumdar, S. G. Warrier, and M. L. Gambone, "A Comprehensive Approach to Understanding the Impact of the Fiber-Matrix Interface on Properties of SiC/Ti-Alloy Composites," presented at the 1996 CMMC Conference on Composites in San Sebastian, Spain, August 1996, and to be published in *Key Eng. Mater.* (1996).
29. S. G. Warrier, B. S. Majumdar, and D. B. Miracle, "Interface Effects on Fatigue Crack Growth of Titanium Matrix Composites: Part I - Crack Deflection and Fiber Bridging," presented at the 1996 TMS Fall Symposium on Interfaces in Cincinnati, OH, and to be submitted to *Acta Metall.* (1996).
30. S. G. Warrier and B. S. Majumdar, "Interface Effects on Fatigue Crack Growth of Titanium Matrix Composites: Part II - Modeling and Impact on Interface Design," submitted to *Mater. Sci. Eng.* (1997).
31. B. S. Majumdar and D. B. Miracle, "Fiber Coatings for a Sapphire/Gamma-TiAl Composite Utilizing Ductile and Barrier Metallic Layers," *Proceedings of the ICCM-10*, 2, Eds., A. Poursartip and K. Street, Woodhead Publishing Limited, pp. 747-754 (1995).
32. S. Krishnamurthy, P. R. Smith, and D. B. Miracle, "Preliminary Evaluation of a Ti-24.5Al-17Nb/SiC Composite," *Scripta Metall. et Mater.*, 31(6), 653-658 (1994).
33. S. Krishnamurthy, P. R. Smith, and D. B. Miracle, "Microstructure and Properties of 'Neat' and SCS-6 Reinforced Ti-24.5Al-17Nb(1Mo) Composite Materials," in Orthorhombic Titanium Matrix Composites, Ed. by P. R. Smith, USAF Wright Laboratory Technical Report, WL-TR-95-4068, 84-104 (July 1995).

34. S. Krishnamurthy, M. R. James, P. R. Smith, and D. B. Miracle, "The Effects of Matrix Microstructure and Texture on Tensile Behavior of an 'Orthorhombic' Ti-Aluminide/SiC Composite," in the Proceedings of the 10th International Conference on Composite Materials, ICCM-10, 2, Eds., A. Poursartip and K. Street, Woodhead Publishing Limited, pp. 739-746 (1995).
35. S. Krishnamurthy and D. B. Miracle, "Effects of Carbon Diffusion on the Microstructure and Properties of SiC/Ti Matrix Composites," presented at the Symposium on Interstitial and Substitutional Effects in Intermetallics, TMS Fall Meeting, Cleveland, OH (November 1995).
36. S. Krishnamurthy, "Analysis of SCS-6 Silicon Carbide Fibers by Fourier Transform Infrared (FTIR) Spectroscopy," J. Mater. Sci., 12(2), 329-331 (1996).
37. S. G. Warrier, S. Krishnamurthy, M. L. Gambone, and P. R. Smith, "Environmental Protection of Orthorhombic Alloys and Composites using Functionally Graded Gamma TiAl Layers," presented at the 1996 TMS Fall meeting in Cincinnati, and to appear in Deformation and Fracture of Ordered Intermetallic Alloys - III, Eds., W. Soboyejo, T. Srivatsan, and H. Fraser (1996).
38. B. S. Majumdar, C. J. Boehlert, A. K. Rai, and D. B. Miracle, "Structure-Property Relationships and Deformation Mechanisms in an Orthorhombic Based Ti-25Al-17Nb Alloy," in High Temperature Ordered Intermetallic Alloys-VI, MRS Symposium Proceedings, Eds., J. Horton, I. Baker, S. Hanada, R. D. Noebe, and D. S. Schwartz, Pittsburgh, PA, 364, 1259-65 (1995).
39. C. J. Boehlert, B. S. Majumdar, and D. B. Miracle, "Effect of Microstructure on the Tensile, Fatigue Crack Growth, and Creep Behavior of a Ti-25Al-17Nb Orthorhombic Alloy," in Fatigue and Fracture of Ordered Intermetallics II, Eds., W. O. Soboyejo, T. S. Srivatsan, and R. O. Ritchie, TMS, Warrendale, PA, 135-53 (1995).
40. B. S. Majumdar, C. J. Boehlert, and D. B. Miracle, "Deformation Mechanisms and Structure-Property Relations in O-Alloys and MMCs (Ti-25Al-17Nb System)," in Orthorhombic Titanium Matrix Composites, Proceedings of the Orthorhombic Titanium Matrix Composites Workshop, WL-TR-95-4068, Wright-Patterson Air Force Base, OH, 65-83 (1995).
41. C. J. Boehlert, B. S. Majumdar, D. Eylon, and S. M. Russ, "Properties and Damage Mechanisms of Three Classes of Titanium Composite Matrices," presented at the International Conference on Composites, Spain, 1996, and to be published in Key Engineering Materials (1996).

42. C. J. Boehlert, B. S. Majumdar, and V. Seetharaman, "Processing and Heat Treatment Effects on the Phase Evolution, Tensile, and Creep Behavior of an Orthorhombic Ti-25Al-25Nb Alloy," presented at the 1996 TMS Fall Symposium in Cincinnati, OH, and in Deformation and Fracture of Ordered Intermetallic Materials, Eds., W. O. Soboyejo, H. L. Fraser, and T. S. Srivatsan, TMS, Warrendale, PA, pp. 565-582 (1996).
43. B. Maruyama, L. L. Shaw, M. C. Waterbury, and D. B. Miracle, "Automated Deformation Mapping in Metal Matrix Composites," *Mater. Sci. Eng.*, A205, 101-109 (1996).
44. A. B. Pandey, B. S. Majumdar, and D. B. Miracle, "The Fracture Behavior of SiCp/Al-Alloy Composites With and Without Large Aluminum Particles," in Proceedings of MRS Spring Symposium on Laminate Structures, Eds., J. J. Lewandowski and W. J. Hunt, 434, 249-254 (1996).
45. A. B. Pandey, B. S. Majumdar, and D. B. Miracle, "Effects of Thickness and Precracking on the Fracture Toughness of a X7093/SiC/15p Composite," submitted to *Metall. Trans. A* (1997).
46. A. B. Pandey, B. S. Majumdar, and D. B. Miracle, "Processing and Fracture Behavior of SiC/Al Alloy Composites," presented at the 1996 TMS Fall Symposium on Processing and Fabrication of Advanced Materials, Eds., J. J. Moore and T. S. Srivatsan, TMS, Warrendale, PA, pp. 185-198 (1996).

3.6 PRESENTATIONS

1. B. S. Majumdar, "Interface and Fatigue Behavior of Metal Matrix Composites," Invited presentation at the Metallurgy Department Colloquium, Cambridge University, England (November 1994).
2. B. S. Majumdar, G. M. Newaz, B. A. Lerch, and D. B. Miracle, "Inelastic Deformation Mechanisms in Metal Matrix Composites," Invited paper at the 4th International Conference on Plasticity, Baltimore, MD (July 1993).
3. B. S. Majumdar, C. J. Boehlert, and D. B. Miracle, "Structure-Property Relationship in the Orthorhombic Ti-25Al-17Nb System," Orthorhombic Composites Workshop, Cincinnati, OH (July 1994).
4. B. S. Majumdar, "Interfaces in Metal Matrix Composites: Current State of Understanding," Colloquium at the Naval Postgraduate School, Monterey, CA (September 1996).

5. C. J. Boehlert, B. S. Majumdar, and V. Seetharaman, "Processing and Heat Treatment Effects on the Phase Evolution, Tensile, and Creep Behavior of an Orthorhombic Ti-25Al-25Nb Alloy," Invited talk at the 1996 TMS Fall Symposium in Cincinnati, OH, Eds., W. O. Soboyejo, H. L. Fraser, and T. S. Srivatsan, TMS, Warrendale, PA, 565-582 (October 1996).
6. S. G. Warrier, "Effects of the Interface on Fatigue Crack Growth Behavior in Titanium Matrix Composites," invited talk at the University of Cincinnati, OH (October 1996).

3.7 LIST OF BOOK CHAPTERS

1. B. S. Majumdar, "Interfaces in Metal Matrix Composites," chapter in book entitled, Titanium Matrix Composites, Eds., S. Mall and T. Nicholas, in print (1996).

3.8 REFERENCES

1. B. S. Majumdar, "Interfaces in Metal Matrix Composites," chapter in book entitled Titanium Matrix Composites, Eds., S. Mall and T. Nicholas, in print (1997).
2. B. S. Majumdar and D. B. Miracle, "Interface measurements and applications in fiber-reinforced MMCs," Key Eng. Mater., 116-117, 153-172 (1996).
3. B. S. Majumdar and S. G. Warrier, "Fracture mechanics of the push-out test and results for titanium matrix composites," presented at the 1996 TMS Fall Symposium on Interfaces at Cincinnati, and two-part papers with D. B. Miracle as co-author to be submitted to Acta Metall. (November 1996).
4. I. Roman, S. Krishnamurthy, and D. B. Miracle, "Fiber-Matrix Interfacial Behavior in SiC-Titanium Alloy Composites," in Titanium '92: Science and Technology, Eds., F. H. Froes and I. L. Caplan, TMS, Warrendale, PA, 2545-2551 (1993).
5. P. Karpur, T. E. Matikas, S. Krishnamurthy, and N. Ashbaugh, "Ultrasound for Fiber Fragmentation Size Determination to Characterize Load Transfer Behavior of Matrix-Fiber Interface in Metal Matrix Composites," in Review of Progress in Quantitative Nondestructive Evaluation, 12B, Eds., D. O. Thompson and D. E. Chimenti, Plenum Press, New York, pp. 1507-1513 (1993).
6. G. N. Frantziskonis, P. Karpur, T. E. Matikas, S. Krishnamurthy, and P. D. Jero, "Fiber Matrix Interface - Information from Experiments via Simulation," Comp. Struct., 29(3), 231-247 (1994).

7. M. C. Waterbury, P. Karpur, T. E. Matikas, S. Krishnamurthy, and D. B. Miracle, "In Situ Observation of the Single-Fiber Fragmentation Process in Metal-Matrix Composites by Ultrasonic Imaging," *Comp. Sci. Tech.*, 52, 261-266 (1994).
8. M. C. Waterbury and S. Krishnamurthy, "Evaluation of Interfacial and Fiber Properties in Titanium Matrix Composites by Single Fiber Fragmentation Testing," in the Proceedings of the 10th International Conference on Composite Materials, ICCM-10, VI, Eds., A. Poursartip and K. Street, Woodhead Publishing Limited, pp. 431-438 (1995).
9. P. Karpur, T. E. Matikas, and S. Krishnamurthy, "Ultrasonic Characterization of the Fiber-Matrix Interphase/Interface for Mechanics of Continuous Fiber Reinforced Metal Matrix and Ceramic Matrix Composites," *Comp. Eng.*, 5(6), 697-711 (1995).
10. P. Karpur, T. E. Matikas, S. Krishnamurthy, and D. B. Miracle, "Recent Developments in Ultrasonic Methods for Metal Matrix Composites Research," in the Proceedings of the 10th International Conference on Composite Materials, ICCM-10, V, Eds., A. Poursartip and K. Street, Woodhead Publishing Limited, pp. 479-486 (1995).
11. S. Krishnamurthy, T. E. Matikas, and P. Karpur, "Role of Matrix Microstructure in the Ultrasonic Characterization of Metal Matrix Composites," *J. Mater. Res.*, 12(2), 329-331 (1996).
12. B. S. Majumdar, T. Matikas, and P. Karpur, "Fiber Fragmentation in Single and Multi-Fiber Composites," in *Proceedings of International Conference on Composites Engineering, ICCE-3, New Orleans, LA*, Ed. D. Hui, pp. 557 (1996).
13. M. C. Waterbury, D. Tilly, W. Kralik, and D. B. Gundel, "Evaluation of TMC Interface Properties by the Slice Compression Test, *Proceedings of the ICCM-10, 2*, Eds., A. Poursartip and K. Street, pp. 719-726 (1995).
14. S. Krishnamurthy, T. E. Matikas, P. Karpur, and D. B. Miracle, "Ultrasonic Evaluation of the Processing of Fiber-Reinforced Metal Matrix Composites," *Composites Science and Technology*, 54, 161-168 (1995).
15. T. E. Matikas, P. Karpur, S. Krishnamurthy, and R. E. Dutton, "A Nondestructive Approach to Correlate the Interfacial Defects Induced During Processing of MMCs and CMCs with the Consolidation Parameters," *Appl. Comp. Mater.*, 2, 293-311 (1995).
16. D. B. Gundel, B. S. Majumdar, and D. B. Miracle, "Evaluation of the Intrinsic Transverse Response of Fiber-Reinforced Composites Using a Cross-Shaped Sample Geometry," *Scripta Metall. et Mater.*, 33, 2057 (1995).

17. D. B. Gundel, B. S. Majumdar, and D. B. Miracle, "The Intrinsic Transverse Response of Several SiC/Ti-6Al-4V Composites to Transverse Tension," *Proceedings of ICCM-10*, 2, Eds., A. Poursartip and K. Street, 703-710 (1995).
18. S. G. Warrier, D. B. Gundel, B. S. Majumdar, and D. B. Miracle, "Stress Distribution in a Transversely Loaded Cross-Shaped Single Fiber SCS-6/Ti-6Al-4V Composite," *Scripta Metall. et Mater.*, 34(2), 293 (1995).
19. S. G. Warrier, D. B. Gundel, B. S. Majumdar, and D. B. Miracle, "Interface Effects on Transversely Loaded Single-Fiber SCS-6/Ti-6Al-4V," *Metall. Trans.* 27A, 2035 (1996).
20. D. B. Gundel, S. G. Warrier, and D. B. Miracle, "The Interface Debond Stress in Single and Multiple SiC Fiber/Ti-6Al-4V Composite under Transverse Tension," accepted for publication, *Acta Metall.* (1996).
21. D. B. Miracle, D. B. Gundel, and S. G. Warrier, "Interfacial Structure and Properties for the Design of Fiber-Reinforced Metal Matrix Composites," to appear in *Processing and Design Issues in High Temperature Materials*, Eds., N. S. Stoloff and R. H. Jones, TMS, Warrendale, PA (1996).
22. S. G. Warrier, B. S. Majumdar, D. B. Gundel, and D. B. Miracle, "Implications of Tangential Shear Stress Induced Failure During Transverse Loading of SiC/Ti-6Al-4V Composites," in press, *Acta Metall.* (1996).
23. S. G. Warrier, B. S. Majumdar, and D. B. Miracle, "Determination of the Tangential Shear Strength of Interfaces and their Impact on Transverse Properties," to be submitted to *Composites Part B: Engineering* (December 1996).
24. S. G. Warrier, B. S. Majumdar, and D. B. Miracle, "Determination of the Interface Failure Mechanism during Transverse Loading of Single Fiber SiC/Ti-6Al-4V Composites from Torsion Tests," *Acta Metall.*, 45(1), 309-320 (1996).
25. W. A. Curtin, "Theory of Mechanical Properties of Ceramic Matrix Composites," *J. Am. Ceram. Soc.*, 74, 2837 (1991).
26. C. Boehlert, B. S. Majumdar, S. Krishnamurthy, and D. B. Miracle, "Role of Matrix Microstructure on RT Tensile Properties and Fiber-Strength Utilization of an Orthorhombic Ti-Alloy Based Composite," *Metall. Trans. A*, 28A, 309-323 (1997).
27. D. B. Gundel and F. W. Wawner, "Experimental and Theoretical Investigation of the Tensile Strength of SiC/Ti-Alloy Composites," in print, *Compos. Sci. and Tech.* (1996).

28. B. S. Majumdar, T. Matikas, and D. B. Miracle, "Fiber Fragmentation and Local Versus Global Load Sharing Behavior in SiC/Ti-6Al-4V Composites," to be submitted to *Acta Metall.* (November 1996).
29. D. B. Gundel, B. S. Majumdar, S. G. Warrier, and M. L. Gambone, "A Comprehensive Approach to Understanding the Impact of the Fiber-Matrix Interface on Properties of SiC/Ti-Alloy Composites," presented at the 1996 CMMC Conference on Composites in San Sebastian, Spain, August 1996, and to be published in *Key Eng. Mater.* (1996).
30. M. Y. He and J. W. Hutchinson, "Crack Deflection at an Interface Between Dissimilar Elastic Materials," *Int. J. Sol. and Structures*, 25, 1053-1067 (1989).
31. V. Gupta, A. S. Argon, and Z. Suo, "Crack Deflection at an Interface Between Two Orthotropic Media," *J. Appl. Mech.*, 59, S79-S87 (1992).
32. S. G. Warrier, B. S. Majumdar, and D. B. Miracle, "Interface Effects on Fatigue Crack Growth of Titanium Matrix Composites: Part I - Crack Deflection and Fiber Bridging," presented at the 1996 TMS Fall Symposium on Interfaces in Cincinnati, OH, and to be submitted to *Acta Metall.* (1996).
33. S. G. Warrier and B. S. Majumdar, "Interface Effects on Fatigue Crack Growth of Titanium Matrix Composites: Part II - Modeling and Impact on Interface Design," to be submitted to *Acta Metall.* (1996).
34. C. Zweben and B. W. Rosen, "A Statistical Theory of Material Strength with Application to Composite Materials," *J. Mech. Phys. of Solids*, 189-206 (1970).
35. B. S. Majumdar and D. B. Miracle, "Fiber Coatings for a Sapphire/Gamma-TiAl Composite Utilizing Ductile and Barrier Metallic Layers," *Proceedings of the ICCM-10*, 2, Eds., A. Poursartip and K. Street, Woodhead Publishing Limited, pp. 747-754 (1995).
36. S. Krishnamurthy, P. R. Smith, and D. B. Miracle, "Preliminary Evaluation of a Ti-24.5Al-17Nb/SiC Composite," *Scripta Metall. et Mater.*, 31(6), 653-658 (1994).
37. S. Krishnamurthy, P. R. Smith, and D. B. Miracle, "Microstructure and Properties of 'Neat' and SCS-6 Reinforced Ti-24.5Al-17Nb(1Mo) Composite Materials," in Orthorhombic Titanium Matrix Composites, Ed. P. R. Smith, USAF Wright Laboratory Technical Report, WL-TR-95-4068, pp. 84-104 (July 1995).
38. S. Krishnamurthy, M. R. James, P. R. Smith, and D. B. Miracle, "The Effects of Matrix Microstructure and Texture on Tensile Behavior of an 'Orthorhombic' Ti-Aluminide/SiC Composite," in the Proceedings of the 10th International Conference on Composite

Materials, ICCM-10, 2, Eds., A. Poursartip and K. Street, Woodhead Publishing Limited, pp. 739-746 (1995).

39. S. Krishnamurthy and D. B. Miracle, "Effects of Carbon Diffusion on the Microstructure and Properties of SiCf/Ti Matrix Composites," presented at the Symposium on Interstitial and Substitutional Effects in Intermetallics, TMS Fall Meeting, Cleveland, OH, (November 1995).
40. S. Krishnamurthy, "Analysis of SCS-6 Silicon Carbide fibers by Fourier Transform Infrared (FTIR) Spectroscopy," *J. Mater. Res.*, 12(2), 329-331 (1996).
41. S. G. Warrier, S. Krishnamurthy, M. L. Gambone and P. R. Smith, "Environmental Protection of Orthorhombic Alloys and Composites Using Functionally Graded Gamma TiAl Layers," presented at the 1996 TMS Fall meeting in Cincinnati, OH, and to appear in *Deformation and Fracture of Ordered Intermetallic Alloys - III*, Eds., W. Soboyejo, T. Srivatsan, and H. Fraser (1996).
42. B. S. Majumdar, C. J. Boehlert, A. K. Rai, and D. B. Miracle, "Structure-Property Relationships and Deformation Mechanisms in an Orthorhombic Based Ti-25Al-17Nb Alloy," in *High Temperature Ordered Intermetallic Alloys-VI*, MRS Symposium Proceedings, Eds., J. Horton, I. Baker, S. Hanada, R. D. Noebe, and D. S. Schwartz, Pittsburgh, PA, 364, 1259-65 (1995).
43. C. J. Boehlert, B. S. Majumdar, and D. B. Miracle, "Effect of Microstructure on the Tensile, Fatigue Crack Growth, and Creep Behavior of a Ti-25Al-17Nb Orthorhombic Alloy," in *Fatigue and Fracture of Ordered Intermetallics II*, Eds., W. O. Soboyejo, T. S. Srivatsan, and R. O. Ritchie, TMS, Warrendale, PA, pp. 135-53 (1995).
44. B. S. Majumdar, C. J. Boehlert, and D. B. Miracle, "Deformation Mechanisms and Structure-Property Relations in O-Alloys and MMCs (Ti-25Al-17Nb System)," Orthorhombic Titanium Matrix Composites, Proceedings Orthorhombic Titanium Matrix Composites Workshop, WL-TR-95-4068, Wright-Patterson Air Force Base, OH, pp. 65-83 (1995).
45. C. J. Boehlert, B. S. Majumdar, D. Eylon, and S. M. Russ, "Properties and Damage Mechanisms of Three Classes of Titanium Composite Matrices," presented at the International Conference on Composites held in Spain, 1996, and to be published in *Key Engineering Materials* (1996).
46. C. J. Boehlert, B. S. Majumdar, and V. Seetharaman, "Processing and Heat Treatment Effects on the Phase Evolution, Tensile, and Creep Behavior of an Orthorhombic Ti-25Al-25Nb Alloy," presented at the 1996 TMS Fall Symposium in Cincinnati, OH, and

in Deformation and Fracture of Ordered Intermetallic Materials, Eds., W. O. Soboyejo, H. L. Fraser, and T. S. Srivatsan, TMS, Warrendale, PA, 565-582 (1996).

47. B. Maruyama, L. L. Shaw, M. C. Waterbury, and D. B. Miracle, "Automated deformation mapping in metal matrix composites," Mater. Sci. Eng., A205, 101-109 (1996).
48. A. B. Pandey, B. S. Majumdar, and D. B. Miracle, "The Fracture Behavior of SiCp/Al-Alloy Composites With and Without Large Aluminum Particles," in Proceedings of MRS Spring Symposium on Laminate Structures, Eds., J. J. Lewandowski and W. J. Hunt, 434, 249-254 (1996).
49. A. B. Pandey, B. S. Majumdar, and D. B. Miracle, "Processing and Fracture Behavior of SiC/Al Alloy Composites," presented at the 1996 TMS Fall Symposium on Processing and Fabrication of Advanced Materials, Eds., J. J. Moore and T. S. Srivatsan, TMS, Warrendale, PA, pp. 185-198 (1996).
50. A. B. Pandey, B. S. Majumdar, and D. B. Miracle, "Effects of Thickness and Precracking on the Fracture Toughness of a X7093/SiC/15p Composite," submitted to Metall. Trans. A (1997).

SECTION 4.0

TASK III. CERAMIC COMPOSITES

Continuous fiber reinforced ceramic matrix composites (CMC) are beginning to be considered seriously as potential structural materials for use in aircraft engine components. They are significantly superior to monolithic ceramics in damage tolerance. While component insertion of the state-of-the art CMCs in certain applications of current engine design may be viable, a lack of oxidation resistance beyond 1000°C has impaired their use as materials that enable newer engine designs. Thus, further developments in CMC must focus on improving the upper temperature limit of use in oxidizing environment.

The bulk of the research work of the current program involved the identification and evaluation of novel interface concepts that will perform the functions that C and BN could, but will resist degradation under an oxidizing environment at or above a temperature of 1200°C. The other major research work involved the fabrication and testing of CMCs that use those interface concepts that are promising. Throughout the research program the research studies were carried out in such a way as to enhance our basic understanding of the interrelationships between processing, structure, and properties of the ceramic matrix composites.

All the work in this task involved collaboration with Drs. R. J. Kerans, A. P. Katz, R. S. Hay, P. D. Jero, N. J. Pagano, C. A. Folsom, E. H. Moore, R. E. Dutton, and Mr. L. E. Matson, and Mr. L. P. Zawada.

4.1 SUMMARY OF MAJOR FINDINGS

4.1.1 EXPERIMENTAL MECHANICS

4.1.1.1 Roughness Effects During Fiber Push-Out Tests

The effect of interfacial roughness on the sliding resistance, during the fiber push-out test, was studied experimentally using a plexiglas/epoxy model system. Controlled roughness was introduced using a mini-lathe, and the roughness profiles were measured using a mechanical profilometer. Various parameters were defined/used to characterize the roughness and a correlation between the push-out behavior and roughness parameters were studied. The parameter that best characterizes the roughness was found to be the maximum Fourier coefficient of the roughness profile. The simple model that assumes the development of a misfit strain of (A/r) due to roughness of amplitude, A , was found to be adequate. This model could be used to determine upper and lower bounds for the tolerance on the roughness amplitude of fibers. Refer to [Publication 36] for additional details.

4.1.1.2 Roughness Effects During Progressive Debonding

The fiber push-out model for progressive debonding was extended to include the roughness effects. The work was conducted in collaboration with Dr. D. B. Marshall of Rockwell International. Previous analyses of the relation between the force and displacement during fiber sliding (pushing or pulling) were extended to include effects of interfacial roughness. Analytical solutions were obtained for a linear profile over the range of displacements that are smaller than the dominant half-wavelength of the roughness. With the equations expressed in normalized form, a convenient friction parameter, which defines the roles of the friction coefficient and the roughness angle, has been defined. For certain values of the friction parameter, the effect of the roughness negates the Poisson's contraction during fiber pulling, giving solutions

that are very close to the response of a system with a constant frictional stress at the interface. Refer to [Publication 34] for additional details.

4.1.1.3 Anticipated Effects of Roughness on Behavior of CMCs

Potential effects of interfacial roughness in ceramic composites were studied using the above-mentioned model. A parametric approach was used to study interfacial roughness in conjunction with other parameters such as strength, radius, and volume fraction of the fiber. The progressive roughness contribution during initial fiber/matrix sliding causes a high effective coefficient of friction as well as increasing clamping stress leading to rapidly changing friction with increasing debond length. Calculated effects imply a potentially significant contribution to the behavior of real composite systems and the consequent necessity for explicit consideration in the interpretation of experimental data in order to correctly understand composite behavior. In a tension test, the Poisson's contraction of the fiber may negate the effects of roughness, allowing an "effective constant shear stress" approximation. This was evaluated using a piece-wise linear approximation to the progressive roughness model in the analysis by Curtin for composite stress-strain behavior; for the Nicalon/SiC system, the "effective t " was found to be lower than the values that would be obtained from fiber push-out tests and/or matrix crack spacings. Refer to [Publications 2, 16, 17, 35] for additional details.

4.1.2 CMC INTERFACES AND COATINGS

4.1.2.1 Fugitive Coatings

Along with the fugitive carbon coatings for oxide/oxide composites, an investigation into the fugitive interfacial coating concept for non-oxide based ceramic composites was carried out. The fugitive interfacial coatings consist of up to three layers of different coating materials: 1) an oxide coating, 2) a carbon layer, and 3) a second oxide coating. The oxide coatings can be of any

type, as long as they are chemically, thermally, and mechanically stable with the adjacent composite constituents. Either oxide coating may be omitted for some choices of composite constituents. Various fiber coating methods can be used, such as sol-gel or chemical vapor deposition techniques.

The coated ceramic fibers are consolidated with a suitable ceramic matrix into dense composites, using any acceptable process. During subsequent use or during heat treatment at high temperatures in air, the carbon layer exits within the composite as CO_x , leaving porosity in its place. The porosity formed at the interface results in the deflection of matrix cracks, leading to fiber pull-out and sustained composite toughness. The extent of fiber pull-out can be altered by controlling the thickness of the carbon layer, and subsequently the extent of porosity at the interface. The oxide layers provide protection for the composite constituents from oxidation and degradation. Refer to [Publications 25, 27, 33, 47, 52] for additional details.

4.1.2.2 Oxidation of Carbon

Both experimental and theoretical investigations of the oxidation of carbon through an annular pore have been conducted. This work has been useful in determining annealing times for removal of the interfacial carbon layer in the fugitive carbon coated composites. Upon realization of an on-going effort by J. Cawley at Case-Western University on the same subject, the work done under this task was combined with the work of J. Cawley in a collaborative effort. The kinetics of oxidation was found to be limited by the reaction rate at lower temperatures and by gas phase diffusion at higher temperatures ($\geq 1000^\circ\text{C}$) Refer to [Publication 27] for additional details.

4.1.2.3 Ductile /Fugitive Interface Coating

For refractory oxide-oxide composites, substantial residual stresses could be developed at the interface due to CTE mismatches between fibers and matrices and/or anisotropy of single crystal fibers. During this reporting period the ductile/fugitive interface coating concept was explored. If a ductile/fugitive interface coating remains during composite consolidation, the fugitive phase could be removed through a subsequent heat-treatment. The resulting porous ductile interlayer should be compliant, relieving the residual stresses at the interface, and therefore promoting the fiber pull-out necessary for toughness. Pd/Mo was the primary ductile/fugitive coating material studied and Pd/C was also considered as an alternative. The following combinations of composites were studied: YAG/Pd-Mo/Alumina, YAG/Pd-Mo/YAG, Sapphire/Pd-Mo/Alumina, and Sapphire/Pd-Mo/YAG. Based upon the composite consolidation and heat-treatment studies, it was found that Mo was a poor choice for the fugitive phase. It appears that Mo reacted with yttria and/or alumina to form low melting yttrium molybdates or aluminum molybdates. There is also a possibility of forming other volatile phases in the Mo-Y-Al-O system. A preliminary examination of Pd-C coatings showed that carbon appears to be a better fugitive phase. Future work will focus on Pd-C as a ductile/fugitive interface coating on sapphire fibers with YAG as a matrix. Refer to [Publication 30] for additional details.

4.1.2.4 Segregant Induced Weakening

The effects of the dopants, Ca, Sr, Sc, Zn and Ni in the alumina/YAG system were studied using single crystal YAG slugs hot-pressed with doped-alumina powder. Using SIMS and analytical TEM, Ca, Sr and Zn were found to segregate to the alumina/YAG interface. The effect of this segregation on the mechanical strength was determined using indentation tests. Of the dopants that showed enhanced presence at the interfaces, Sr weakened the interface uniformly, while Ca weakened the interface at certain, but not all, locations along the interface.

Based on the promise with regard to interface weakening, additional tests were conducted to verify if the interface weakening was sufficient to deflect cracks. Two types of tests were conducted. In the first, a four-point bend configuration was used to start a crack from a pre-machined notch in such a way that the crack will intersect the YAG/alumina interface. In such tests, significant crack deflection was observed in the doped specimens when compared with undoped specimens. The second type of test involved a similar test with singled crystal YAG fibers in alumina matrix. Only a limited number of tests could be done due to shortage of YAG fibers. The volume fraction of fibers was also low (<0.02). No significant pull-out behavior was seen. Interfacial roughness is believed to be one of the causes for the short debond lengths. Refer to [Publication 48] for additional details.

4.1.3 FIBER COATINGS

4.1.3.1 Cleavable Oxide Interphase for Oxide–Oxide Composites

The concept of an oxidation resistant fiber–matrix interphase that deflects cracks by cleavage is being explored. Sols with the nominal composition $\text{CaAl}_{12}\text{O}_{19}$ were used to coat single-crystal alumina fiber and plates and yttrium-aluminum garnet fiber. Subsequent annealing, or consolidation in a matrix, results in strong texturing of the hibonite coating with basal planes parallel to the interface. Texture development within the hibonite interphase occurs by a complex series of phase transformations and reactions. The alumina fibers and plates seeded the phase transformation of sol-derived transition aluminas to $\alpha\text{-Al}_2\text{O}_3$. $\text{CaAl}_{12}\text{O}_{19}$ and CaAl_4O_7 formed between the seeded $\alpha\text{-Al}_2\text{O}_3$, and CaAl_4O_7 later reacted with the seeded $\alpha\text{-Al}_2\text{O}_3$ to form $\text{CaAl}_{12}\text{O}_{19}$, resulting in a single-phase coating. The textured fiber coating could be retained after hot-pressing in an alumina or YAG matrix, or formed *in situ*, under the right processing conditions. The current temperature of 1400°C required for complete reaction and abnormal grain growth for texturing to occur is too high for commercially available oxide fibers, such as Nextel™ 610 and 720, which are generally limited to a maximum temperature of 1300°C .

Alternate precursors to hibonite or other hexaluminates may allow for the coating, and subsequent processing, of these fibers at lower temperatures.

Model composites containing hibonite-coated fibers were tested and showed evidence of crack deflection within the interphase. The fracture energy of cleavage of a textured polycrystalline hibonite interlayer has been determined to be about 2.2 J/m². Observations of fracture surfaces in model composites indicate crack deflection within the hibonite coating, with subsequent crack propagation occurring by cleavage. These observations indicate that a textured, cleavable oxide interphase should be a viable fiber coating for alumina-based composites. However, the interfacial shear stresses developed after debonding during fiber pull-out are likely to be very high in composites containing a thick interphase, but thinner fiber coatings may lower these stresses to an acceptable range. Refer to [Publication 12, 20, 22] for additional details.

4.1.3.2 Electrostatic Enhanced Sol-Gel Coating of Fibers and Cloths

The successful coating of multifilament tows and cloths requires complete and uniform coverage of fibers without bridging the fibers and tows by the coating. Two methods were investigated for coating NicalonTM cloths with oxides. The first, dip coating, relies strictly on the wetting of the fibers by the oxide sol, while the second, electrostatic coating, relies on the control of a surface charge to encourage heterocoagulation of the particles on the fiber surfaces. While continuous dip coating has been shown to be effective for coating monofilaments and tows, it was not found to be a promising method of coating woven fiber cloths and preforms. The limitations of this technique for coating cloths include the need for relatively high concentration sols to provide adequate coating thicknesses, which also leads to bridging of fibers due to capillarity. Wetting of the fiber by the sols seems to be a problem in obtaining uniform coverage. Wicking of the liquid toward the outer surfaces of the cloth leads to excess coating and fiber bridging near the surfaces. The use of an immiscible liquid to displace excess sol from between fibers and tows is complicated by the tortuosity of the cloth.

One method of overcoming a number of these difficulties is to control the surface charge of the fibers in the cloth and of the particles in the sol. This enables the deposition of the coating while the cloth is fully infiltrated by the sol, which allows for retention of a uniform coating upon dewetting of the cloth. Uniformly coated cloths are produced while minimizing the dependence on the wetting relationship between fiber and sol and while reducing the sol concentration by two orders of magnitude, thereby enhancing excess sol removal from the surface of the cloth. The use of water to displace excess aqueous sol from the cloth surface resulted in minimal bridging with uniform fiber coatings. The use of a polyelectrolyte enabled multiple deposition of coatings onto the fibers in the cloth. Multiple coating steps resulted in completely coated fiber surfaces, which was limited to <50% coverage with a single coating step. However, a poor coating was obtained at points of tow-tow crossover, even with vacuum infiltration of the polyelectrolyte and sol. The time required to completely out-gas the cloth under vacuum suggests that a significant area of fiber remains in contact with air, rather than with the precursor liquid, especially during coating at atmospheric pressure. Refer to [Publications 9, 10] for additional details.

4.1.3.3 TEM Specimen Preparation of Coated Ceramic Fibers

A method of preparing transmission electron microscopy (TEM) specimens of coated ceramic fibers has been developed. This method produces representative thin sections that allow for the detailed characterization of thin coatings, the fiber, and the fiber-matrix interface. Multiple individual fibers or tows are impregnated with a high-temperature epoxy and contained to assure a high fiber-to-epoxy volume ratio. The samples are then sectioned and mechanically thinned either transverse or normal to the fiber axes using a wedge polisher on diamond lapping films to achieve a thickness of less than 5 μm . The thinned sample is then ion-milled to electron transparency in less than 30 min, giving representative specimens of the coating, fiber, and coating-fiber interface. The main advantage of this method over conventional preparation techniques is that large electron transparent areas can be obtained, while minimizing preferential

milling of the different phases present in the specimen. The technique is suitable for any multiphase sample with large differences in hardness between the constituents and can also be used for preparing extremely flat specimens for SEM analysis, as has been illustrated for oxide-coated ceramic fibers. Refer to [Publication 21] for additional details.

4.1.3.4 Hexaluminate Coatings on Commercially Available Polycrystalline Fiber Tows

With the promising performance of model composites prepared using calcium hexaluminate as the fiber-matrix interphase, the next logical step is to produce a full scale composite to truly test the interphase concept. Unfortunately, there are several problems in coating the existing commercially available oxide fibers with our hibonite precursor sol. The precursor used for coating single crystal fibers, boehmite doped with calcium-acetate, results in the start of hibonite formation at about 1150°C, but does not fully convert until >1400°C in reasonable processing times. Complete texture first appears after one hour at 1400°C, whereas the maximum processing temperature of the most refractory fiber available, Nextel™ 720, is 1300°C.

The Ca-doped boehmite sol deposited on sapphire was heat treated at 1300°C for 12 h to assess the degree of texturing that occurs at this temperature. TEM indicated that about 60% of the coating reacted to hibonite. The hibonite grains adjacent to the fiber were oriented with basal planes in the plane of the interface. Grains closer to the matrix side of the coating tended to be rotated so that their basal planes were oriented up to ~60 degrees out of the plane of the interface. The microstructure was clearly in transition.

Coatings of the baseline precursor do not form hibonite on Nextel™ 720 fibers. Problems encountered include, the significant migration of Ca to the grain boundaries of the polycrystalline fibers and/or reaction of CaO with mullite and alumina in the fibers during heat treatment to form a CAS liquid phase. This precursor requires temperatures of 1400°C for at least one hour to

form and texture the hibonite grains. Other precursors have been investigated to see if lower reaction temperatures can be obtained. Substituting other alkaline earths and rare earths for Ca has resulted in higher minimum temperatures for complete reaction.

A number of alternate precursors to hibonite were explored, including forming a sol by the direct reaction of Ca and Al in isopropanol and then by the formation of carboxylatoalumoxanes. While the former sol gave a powder that reacted more completely at 1300°C, the particle size produced during hydrolysis was too large to form a stable sol. In the case of the latter sol, boehmite is broken down with carboxylic acid to form a structure surrounded by carboxylic acid groups. Using Ca-acetylacetonates, one is reportedly able to exchange Ca for Al in the alumoxane structure. XRD of heat treated powders actually resulted in a higher reaction-to-hibonite temperature.

The formation of the intermediate 1:1 or 1:2 phase prior to the magnetoplumbite/beta-alumina phase in all similar systems (CaO, BaO, SrO, La₂O₃, etc.-Al₂O₃) is believed to dictate the subsequent reaction to the 1:6 (magnetoplumbite) phase; unless molecularly mixed precursors are used it seems unlikely that lower reaction temperatures will be obtained. However, even if they are, temperatures of 1400°C are still needed for sufficient grain growth to occur for texturing to take place. Refer to [Publications 12, 20, 22] for additional details.

4.1.3.5 Monazite Fiber Coatings

The motivation of this work is based on the use of weak interfaces in toughening CMC's. A recent micromechanical study showed the monazite-alumina interface to be weak and to meet the criteria of crack deflection and fiber pull-out. Solution- and sol-derived monazite (LaPO₄) were continuously coated on 3M Nextel™ 720 fiber tows with a vertical coater. In the solution derived coating, a modification of an alkyl phosphate method was adopted. This consisted of wetting the fiber tows with a mixture of trimethyl phosphate and lanthanum nitrate in the molar

ratio of 1:1 to 1:3. The coated fibers were cured in line at temperatures of 900, 1000, 1100, 1200 and 1300°C. The sol-derived fiber coating was made with a colloidal monazite sol. The sol was produced from lanthanum nitrate/diammonium hydrogen phosphate and peptized with nitric acid. In some formulations monazite/carbon mixtures were made by adding Duramax B-1043 (a polyelectrolyte) to the monazite sol. The monazite/Duramax B-1043 mixtures convert to monazite/carbon mixtures when cured in argon at 1000°C or more.

The percent coverage of the solution-derived monazite on the fiber filaments was ~95 % and ~100% for LaPO_4 concentrations of 20 g/l and 40-80 g/l, respectively. The percent coverage of the sol-derived monazite fiber coatings depended on the acid content of the sol. The sol-derived monazite coatings done with sols of acid concentrations $< 0.14 \text{ M}$, gave a high coverage ~95-100%. Coatings from sol-derived monazite with acid concentrations in the range of 0.4 - 1.9 M were not continuous (~40-50%).

Monazite coating of different porosity were made by selecting a variety of phosphorous compounds as precursors. The solution-derived coatings (alkyl phosphate method) were found to be more densified than the sol-derived coatings. In the sol-derived coatings, platelet or elongated granular monazite was formed, depending on the curing temperature and the number of passes.

Filament tensile strength degradation was found to be greater in the solution-derived fiber coatings, as compared to the sol-derived fiber coatings. Filament tensile strengths decreased from 1.58 GPa to 1 GPa and from 1.58 GPa to 1.47 GPa in the solution- and sol-derived monazite after fiber coating. For the sol-derived coatings, fibers coated at 1300°C, 1400°C with a $\text{La}:\text{PO}_4$ molar ratio of 1:1 were spoolable. Fibers coated at 1300°C with $\text{La}:\text{PO}_4$ of 1:1 to 1:1.5 solution-derived monazite were not spoolable, while those coated at 1300°C with $\text{La}:\text{PO}_4$ of 1:1.8-1:3.0 were spoolable. Fibers coated at 1200°C and below with 1:1 $\text{La}:\text{PO}_4$ solution-derived monazite were also spoolable. Refer to [Publications 4, 14] for additional details.

4.1.4 NEAR-TERM OXIDE-OXIDE COMPOSITES

4.1.4.1 Nextel™ 550,720/Carbon/MAS, CAS

These various composite systems were used to evaluate the effectiveness of fugitive interfaces for oxide/oxide composites. Initially, Nextel™ 550/Carbon/MAS (magnesium aluminosilicate) composites were fabricated through filament winding and subsequent hot pressing at 950°C/15 min./2000 psi. These samples were machined into dogbone specimens and tensile tested in one of three conditions: 1) as-processed (with the carbon layer intact), 2) oxidized at 650°C/24 h/flowing oxygen, and 3) as-processed (with no carbon interlayer). The tensile test results indicated that the inclusion of the carbon coatings led to non-catastrophic composite behavior, compared to the brittle failures experienced by the samples with no initial carbon coating. This desirable composite behavior was retained even after the removal of the carbon layer by oxidation. These results suggest that fugitive interfacial layers may to be a viable option for increasing the toughness of oxide/oxide composites in high-temperature, oxidizing environments. Refer to [Publications 47, 52] for additional details.

4.1.4.2 Nextel™ Fabric (550 and 720)/Carbon/Mullite

The listed composite systems were studied to assess the feasibility of their usage for near-term turbine engine components. These composites were produced using matrix slurry pressure infiltration into fiber preforms. The green composites were subjected to multiple vacuum impregnations of appropriate sols to increase the matrix content. Commercial vendors were identified for both the preforms and the mullite powder; mullite cloth (Nextel™ 550 and 720) is available from 3M Corporation, while Baikowski International produces submicron, high purity mullite powder. Experiments were carried out to study the effects of fibers (Nextel™ 550 and 720) and matrices (Mullite-SiO₂ and Mullite-Mullite) on the final composite strength. Three

different types of composites were fabricated: 550/C/Mullite-SiO₂, 720/C/Mullite-SiO₂, and 720/C/Mullite-Mullite. The carbon fugitive interface coating was deposited using a pitch/toluene solution. The quality of the carbon coatings was not optimal, due to insufficient filtration at cross-over regions, cementing, and spallation; however, due to the capability of the Materials Directorate, this coating process was used over the more desirable CVD technique.

The Mullite-SiO₂ matrix designation indicates the pressure infiltration of SiO₂-coated mullite powder slurry into a preform, followed by five vacuum impregnation cycles of SiO₂ sol. The Mullite-Mullite term indicates the pressure infiltration of mullite powder slurry into a preform, followed by five vacuum impregnation cycles of mullite sol. The sintering of composites with Mullite-SiO₂ and Mullite-Mullite matrices were carried out for two hours in vacuum at 1050°C and 1150°C, respectively.

Tensile test specimens were machined, tabbed, and tested at room temperature using hydraulic wedge grips. In general, the load-displacement curves exhibited non-linearity from the start and showed a saw tooth type behavior before reaching maximum load. The SEM fractographs of the failed composites showed minimal fiber pull-outs, although the degree of fiber pull-outs varied with the sintering temperatures (longer pull-out lengths for lower sintering temperatures). The strength of the composites also varied from 50 MPa-160 MPa, depending upon the composite systems.

The average tensile strengths of composites containing Nextel™ 720 fabric were higher than those with Nextel™ 550 fabric, due to the better strength retention of 720 fiber after the high temperature sintering. The average tensile strengths of the Nextel™ 720 fabric-reinforced composites with the Mullite-SiO₂ matrix were higher than those with the Mullite-Mullite matrix, due to the lower sintering temperature required for the Mullite-SiO₂ composites. It was also observed that the variations in the measured strengths of the composites, partially stemmed from

artifacts (misalignment and warpage) of the tensile test specimens. Refer to [Publications 38, 52] for additional details.

4.1.4.3 The Mean Tensile Strength and the Weibull Modulus of Ceramic Filaments

Mean strengths and Weibull moduli for alumina/yttrium aluminum garnet (YAG) eutectic filaments and for Si-C-O (NicalonTM) filaments were calculated using actual and average filament diameters. The mean strengths agreed closely. The mean strength calculated from the average filament diameter could be used as an excellent approximation of the mean strength using the actual filament diameters. The Weibull modulus from an average filament diameter approximates the Weibull modulus obtained using the actual filament diameters. Refer to [Publication 5] for additional details.

4.1.4.4 The Effect of Thermal Exposure on the Strengths of NextelTM 550 and 720 Filaments

The effect of thermal exposure on the strengths of NextelTM 550 and 720 filaments was determined by the uniaxial tensile testing of single filaments extracted from tows that had been exposed to different heat treatments. The results facilitate choosing the maximum processing temperature that can be used for the tows.

For NextelTM 550 filaments, a 28% drop in strength occurred after a heat treatment of 1100°C in air. After a heat treatment of 1300°C a strength degradation of over 47% resulted.

For NextelTM 720 filaments, exposure at 1100°C in air revealed less than 9% strength loss with less than 21% at 1300°C. Refer to [Publication 6] for additional details.

4.1.4.5 ARPA- Salt Water Effect on BN/Nicalon™

This work was undertaken to study the mechanisms responsible for fatigue loss of certain Nicalon™-Reinforced composites when exposed to intermittent salt fog. The contribution of loss in fiber strength was explored as a plausible mechanism. The results are detailed below.

When either uncoated or BN-coated Nicalon™ fibers are exposed to water saturated with NaCl and then annealed in air at 1000°C, a structural degradation of the fiber occurs. The fiber surface oxidizes to tridymite instead of vitreous silica; further the crystallites of SiC in Nicalon™ begin to grow rapidly in size. These findings suggest that prior exposure to salt water may cause appreciable debit in the mechanical strength of Nicalon™ fibers with time at 1000°C in air. Refer to [Publication 26] for additional details.

The contribution of fiber strength degradation to the environmental instability of Nicalon™ fiber-reinforced ceramic matrix composites was investigated. The effect of anneal in air at 1000°C (2 h) and the effect of exposure to salt (NaCl) water (0.05, 0.5, and 5 wt.%) prior to the anneal were studied using uncoated and BN-coated Nicalon™ fibers. The results imply that both Nicalon and BN-coated fibers degrade in strength, during a 1000°C air anneal, with the BN-coating showing higher strength loss. The degradation is significantly enhanced if the fibers are exposed to salt water prior to the air anneal and if the concentration of the salt water is more than 0.5 wt.%. For the BN-coated Nicalon™ fibers, the effects were further investigated as a function of temperature down to 800°C. The degradation in strength due to salt water exposure was more at 800°C than that at 900°C or 1000°C. Refer to [Publication 1] for additional details.

4.1.5 YTTRIUM ALUMINATES

4.1.5.1 Fracture Toughness of YAG Single Crystal

The fracture toughness of single crystal YAG has been measured from room temperature to 1600°C in air and in vacuum using the SENB method. The measured K_{IC} is 2.2 MPa√m at room temperature and it increases with temperature above 1200°C, reaching a value of 4.5 MPa√m at 1600°C in air. The toughness increases further if the partial pressure is reduced, reaching a value of 5.5 MPa√m in a vacuum of 10⁻⁵ torr at 1600°C. Previously reported values of 6.9 MPa√m in vacuum at 1600°C are probably overestimates, due to a reaction of the specimen with the HfB₂ jig used. Refer to [Publication 42] for additional details.

4.1.5.2 Y₄Al₂O₉-Y₂O₃ Eutectic

The eutectic composition between Y₄Al₂O₉ and Y₂O₃ was determined using electron probe microanalysis (EPMA) on directionally solidified specimens with hypo- and hyper-eutectic compositions. The microstructures of the specimens as a function of composition differ considerably with small deviation from the eutectic composition (70.5 mol% Y₂O₃ and 29.5 mol% Al₂O₃). Based on the current results and other published data, the pseudobinary system between Al₂O₃ and Y₂O₃ was revised. Refer to [Publication 58] for additional details.

4.1.5.3 Oxide/Intermetallic Composites

Solid state reactions were evaluated between intermetallic alloys in the Ni-Al and Ti-Al systems and oxides in the Al₂O₃-Y₂O₃ system. Refer to [Publication 45] for additional details.

4.1.5.4 High Temperature Environmental Stability of Yttrium Aluminates

Heat treatments in several environments were performed on a series of compounds in the Al_2O_3 and Y_2O_3 system: Al_2O_3 - $\text{Y}_3\text{Al}_5\text{O}_{12}$ eutectic, $\text{Y}_3\text{Al}_5\text{O}_{12}$, YAlO_3 , $\text{Y}_4\text{Al}_2\text{O}_9$, and Y_2O_3 . The yttrium aluminates were found to be stable at high temperatures in vacuum and air. However, when heat treated in vacuum in proximity to SiC, degradation was observed. This was found to be primarily a result of carbothermal reduction. In a similarly reducing environment without Si, the yttrium aluminates, and Al_2O_3 and Y_2O_3 , all exhibited degradation by carbothermal reduction. Based upon the experimental results, a degradation mechanism for yttrium aluminates was proposed. Refer to [Publication 46] for additional details.

4.1.5.5 YAG Powder Synthesis

The primary activities in this area have been the establishment of processing conditions to produce the desired stoichiometry, morphologies, sizes and distributions of YAG powder. Mixed alkoxide processing yielded a mixture of alumina, YAG, YAP, and YAM. Through NMR analysis, the formation of yttrium aluminum double alkoxide $[\text{Y}\{\text{Al}(\text{OPri})_4\}_3]$ in the mixed alkoxide was verified. Molecular modification of yttrium isopropoxide was carried out through the substitution of one of the iso-propyl group with a bulky EAA (acetoacetic ethyl ester) group. The modification was confirmed by using IR spectroscopy. Through the molecular modification, single phase YAG powder was obtained.

4.1.5.6 Residual Stress Measurement

The alumina/YAG eutectic and later Sapphire/YAG composites were studied under X-ray diffraction for residual stress measurements. Initially polycrystal YAG (fabricated from Ceralox powder) was tried as a standard for YAG; but it was found that the reproducibility was not sufficient for stress measurement. It is believed that the hot-pressed YAG will have residual

stresses from processing. The Ceralox powder was then tried, and found to be very good in obtaining reproducible peak positions, but the peaks are weak and needed very slow scans ($0.02^\circ/\text{min}$). The Sumitomo powder was used as a standard for alumina peak positions.

For the case of the eutectic, three sides (X, Y, and Z) were studied for shifts in YAG peaks. The Z is the direction of solidification. It was not possible to ensure that the same grain of eutectic was studied in all three orientations. The strain perpendicular to the X-orientation was -2.5×10^{-4} (~ -75 MPa), that perpendicular to the Y-orientation was 2.1×10^{-4} (~ 62 MPa), and that perpendicular to the solidification direction was 2.7×10^{-4} (~ 81 MPa). The X-rays penetrate about $25 \mu\text{m}$ into the material and the YAG phase is $\sim 5 \mu\text{m} \times 30 \mu\text{m}$ in dimensions. Thus, measurements will capture some stresses normal to the surface, in addition to the Poisson strain, from the in-plane stresses. NDSANDS gives a stress of ~ 200 MPa for the radial and tangential stresses and ~ 370 MPa for the axial stress for a-sapphire/YAG (50%) composite. The Poisson strain corresponds to -3.4×10^{-4} , and the axial strain is 12×10^{-4} . Clearly the strains measured are smaller but they are of the order of the strain measured. In addition to these experiments, gamma scans were also conducted to see if YAG or sapphire were continuous, and the results reinforce the previous conclusions that the sapphire is continuous and YAG is discontinuous, but with pronounced texture (or specific orientation relationship to sapphire).

In the case of the c-sapphire/YAG composite, the measurements are more reliable due to the geometry. The sapphire was oriented with its c-axis perpendicular to the surface. The X-rays penetrate only a fraction of the diameter of the fiber ($125 \mu\text{m}$) and thus, most of the strain measured must come from Poisson strain. The strain measured along the c-axis was 4.5×10^{-4} (~ 180 MPa). The NDSANDS calculation gives a compressive radial/tangential stress of 50 MPa which yields a Poisson strain along the fiber axis of 2.5×10^{-4} . The difference between this and the measured strain may come from sintering stresses (matrix shrinking around the fiber).

4.1.6 MISCELLANEOUS

4.1.6.1 SiC-Whisker Reinforced Mullite/Zirconia

The high temperature deformation of a mullite-25 vol.% zirconia composite was studied in both unreinforced and in a SiC-whisker reinforced condition. The work was presented at the annual meeting of the Ceramic Society in Cincinnati, OH, 1994. The unreinforced composite was found to be inferior to pure mullite and this deterioration appears to come from changes in grain morphology, more than due to the presence of the weaker zirconia phase, although this explanation may be incomplete. The addition of whiskers increased the creep resistance at low stresses or at strain rates close to those of engineering interest. For example, at 1583 K, the creep rate decreased by an order of magnitude to $\sim 10^{-6}/s$ at 88 MPa and continued to decrease significantly with decreasing stress, with an apparent threshold stress for creep at ~ 45 MPa. At high strain rates ($>10^{-4}/s$), no significant strengthening occurred. This behavior could be rationalized by suggesting a threshold stress for creep, which has its physical origin in the back stress developed from a network of whiskers, as proposed by Porter et al. However, the strong temperature dependence of this threshold stress leaves the model incomplete. The presence of glassy phases at the whisker/matrix interfaces may explain the steep drop in the threshold stress with increased temperature. The decreased viscosity of the glassy phases with increased temperature might affect load transfer to whiskers, thereby decreasing back stress from the whisker network. Refer to [Publication 19] for additional details.

4.1.6.2 Yttria-Stabilized Cubic Zirconia

Heuer and co-workers have opened up the possibility of strengthening zirconia through solid solution and precipitation hardening. In particular, they have found that the flow stress of Y_2O_3 stabilized cubic zirconia can be increased significantly by increasing the content of Y_2O_3 in solid solution. The flow stress at 1400°C at a strain rate of $1.3 \times 10^{-5}/s$ has been reported to

increase from 150 MPa at 9.4 mol% yttria to nearly 350 MPa at 21 mol% yttria. These are promising results since they make zirconia a potential high temperature material as well. In particular its high thermal expansivity (~ 10 ppm) compares favorably with many intermetallic materials making ZrO_2 a potential fiber for reinforcement of intermetallic matrices. In the present work, the creep behavior of yttria-stabilized cubic zirconia was studied at strain rates closer to engineering design requirement of $10^{-8}/\text{s}$.

Solid solution strengthening for creep was examined in yttria-zirconia system by comparing 9.4 mol% and 21 mol% Y- ZrO_2 . At 1673K, strengthening decreased with decreasing strain rate, with nearly no relative strengthening at $\sim 10^{-7}/\text{s}$. At 1573K a similar trend with strain rate was observed, but still significant strengthening was observed even at lower strain rates. At 1473K fracture preceded flow for the 21 mol% alloy. The creep behavior of the 9.4 mol% Y- ZrO_2 could be rationalized using measured stress dependencies of dislocation density and dislocation velocity. The differences between the 9.4 mol% and 21 mol% alloy could be rationalized based on the solute drag model, which predicts the size mismatch to play a significant role in solid solution strengthening of these alloys. Refer to [Publication 3] for additional details.

4.1.6.3 Freeze Forming of Ceramics

Sol-gel processing of ceramic monoliths is limited by the shrinkage that occurs, due to the evaporation of liquid during drying. Freeze forming alleviates this shrinkage problem by eliminating the liquid through solidification followed by sublimation of the solvent. The result is a 3-D structure that exhibits virtually no shrinkage or cracking. The work presented here focused on the freeze forming of aqueous alumina sols filled with alumina powder.

The filled, aqueous-based alumina sol was cooled, forcing the crystallization of ice. During crystallization, the sol and filler powder particles were pushed into interdendritic regions

between the ice crystals. After sublimation, the freeze-dried samples were infiltrated with epoxy for characterization. This microstructural characterization revealed that the ice grew in a dendritic fashion, with the basal plane parallel to the heat flow direction. The epoxy-filled voids left by the sublimated ice crystals generally had one flat side and one undulated side. The flat side was presumably formed by the basal plane of the ice crystals, while the undulated side represented limited growth along the c-axis. This growth morphology has been demonstrated in the free growth of ice dendrites into supercooled water.¹

The primary dendrite spacings for the freeze dried monoliths were measured at various heights within the samples, which corresponded to different cooling rates. The primary dendrite spacings were then correlated with the sample cooling rate, which is given by the following common metallic solidification relation:

$$l = A[(dT/dx)(dx/dt)]^n$$

where l is the primary dendrite spacing, $[(dT/dx)(dx/dt)]$ is the cooling rate and A , n are constants. It was found that the dendritic spacing of the ice crystals could be directly correlated with the freezing rate. This information will allow for more control over the microstructural features of a ceramic monolith or composite. Refer to [Publication 24] for additional details.

¹Y. Furukawa and W. Shimada, "Three-Dimensional Pattern Formation During Growth of Ice Dendrites - Its Relation to Universal Law of Dendritic Growth," *Journal of Crystal Growth*, 128, 234-239 (1990).

4.2 SUMMARY OF CURRENT WORK NOT REPORTED

4.2.1 FIBER COATINGS

4.2.1.1 Stability of Hexaluminates with SiC in Air

With the scarcity of refractory oxide fibers on the market, the use of a cleavable oxide on SiC fibers is being considered. However, it is known that SiC and alumina are not compatible in air at elevated temperatures. Based on phase diagrams of the relevant systems, one can assume that all hexaluminates will behave similarly and will also behave similarly to alumina, in the stabilizing-cation-deficient side of the alumina-silica-MO phase diagram. Hibonite was chosen as the prototype for thermodynamic calculations since it is the only hexaluminate for which standard heats of formation could be obtained. Calculations confirm the phase diagram and predict that hibonite and silica (the oxidation product of SiC) are not phase compatible and that the most likely products are mullite, anorthite, and corundum, or cristobalite, depending on the hibonite:silica ratio.

Diffusion couples were prepared to examine the reaction kinetics. Three hot-pressed hibonite-hot-pressed 4 wt. % Al_2O_3 -doped SiC couples have been heated to 1200, 1300, or 1400°C in air for 100 h each, while one couple was heated to 1400°C in argon for 100 h. The couple heated in argon did not show evidence of reaction, and hence we can conclude that hibonite and SiC are compatible. However, those couples heated in air did react. The reacted surfaces of the SiC halves produced peaks attributable to cristobalite and SiC, while the 1300 and 1400°C samples contained weak mullite peaks as well. At 1200°C the outer SiC surfaces were unchanged to the naked eye, while at 1300 and 1400°C the surfaces were clearly covered by a smooth oxide layer that was liquid at those temperatures. The hibonite surfaces contained, at 1200 and 1300°C mainly hibonite and anorthite with some alumina, and at 1400°C mainly

alumina and mullite with traces of anorthite and hibonite. Even at only 1200°C the extent of reaction is not tolerable for a 0.5 μm -thick fiber coating.

The use of a reaction barrier in the form of a coating of anorthite on the fiber prior to the hibonite coating may prevent reactions since anorthite is phase compatible with hibonite, calcium dialuminate, alumina, mullite, and, silica. This work is still in progress.

4.2.1.2 Microcomposites of Sapphire-Hibonite-Alumina

A new method of preparing single fiber composites was developed. An alumina colloidal slurry that was modified from its original use in tape casting was used to coat the hibonite-coated fibers. After heat treating the hibonite-coated sapphire fibers, they were passed through a syringe needle filled with the alumina colloid to aid in controlling thickness of the matrix. Relatively uniform coatings were applied, where thickness can be controlled by rate of drawing of the fiber through the needle (a la dip coating). Sintering at 1450°C for two hours results in an incompletely sintered coating, that is nevertheless crack free and adheres well to the fiber. Also produced were microcomposites without matrix at the ends to test the influence of matrix in slippage of the epoxy grips during testing. These composites are currently being used for evaluation of mechanical behavior.

4.2.1.3 Porous Oxide Coating

Porous oxides are among the plausible interface materials for toughening ceramic-fiber composites (CMC's). Porous oxide coatings were made from homogeneous oxide-carbon mixtures. After incorporating the coated fiber into a matrix, the carbon is burned off leaving a porous oxide coating. The modulus and fracture energy of porous oxides decreases exponentially as the porosity is increased. Therefore, the fracture energy of the coating can be tailored to low values, by increasing the carbon content of the carbon-oxide mixtures. A variety of hydrocarbon-

oxide sol were made and used to coat Nextel™ 720 fiber tows. Among the hydrocarbons used are sugar and the polyelectrolytes: Darvan 821 A, Darvan C, Duramax B-1043 and Glascol C-5. Porous alumina and mullite were studied. Homogeneity of the oxide carbon mixtures were found to depend on the degree of association of the carbon precursor and the oxide. Due to the absence of electrostatic interactions, coatings of alumina-sugar and aluminum nitrate-Darvan C mixtures were found to be inhomogeneous. Coatings of alumina-Duramax B-1043, alumina-Darvan C, alumina-Darvan 821 were found to be homogeneous. Coatings of alumina-Glasscol C-5, and Mullite-Darvan 821 A have not been evaluated for homogeneity. Refer to [Publication 13, 14] for additional details.

4.2.2 NEAR-TERM OXIDE-OXIDE COMPOSITES

4.2.2.1 Nextel™ 550,720/Carbon/MAS, CAS

Due to the high-temperature strength degradation of the Nextel™ 550 fiber, further composites were fabricated using the more stable Nextel™ 720 fiber. The matrix was changed to CAS (calcium aluminosilicate), due to the large coefficient of thermal expansion mismatch between the Nextel™ 720 fiber and MAS. These composites were fabricated in the same manner, with a slightly higher hot-pressing temperature of 1050°C/15 min./2000 psi. After machining, samples were tensile tested in the as-processed condition (with carbon intact), after oxidization at 650°C/24 h/flowing oxygen, and after a long-term, high-temperature heat treatment at 1000°C/100 h/air. As expected, the addition of the carbon interlayer, greatly enhanced the mechanical behavior of the composites. This behavior was retained after the long-term, high temperature heat treatment, which established the stability of the gap produced by the carbon oxidation. The results discussed here demonstrate that the addition of a fugitive carbon interlayer significantly improves the failure behavior of oxide/oxide composites.

Aside from aiding the toughness, the carbon removal also decreases the dielectric constant of the composite material. This fact was confirmed through dielectric testing of as-processed and oxidized Nextel™ 550/C/MAS composites. With the carbon intact, the dielectric constant was ~20. After the carbon oxidation, the dielectric constant fell to ~5, which conforms the value (<10) needed for low observable applications.

4.2.2.2 Nextel™ Fabric (550 and 720)/Carbon/Mullite

This is an on-going project and within the next contract program, we will study the Nextel™ 720/C/Mullite-Mullite composites further to improve the following: (1) alignment, warp and fill direction, of fabric lay-ups, (2) minimize warpage of green composite, (3) infiltration of mullite matrix and mullite sol impregnation to increase matrix density, (4) determine the optimum condition for partial sintering of the matrix, and (5) better specimen machining with respect to the fiber direction and tab attachments.

A collaborative effort with Oak Ridge National Laboratories for CVD carbon coating on 2-D preform is in progress. These CVD carbon coated preforms will be used during the next contract to fabricate composites and tensile tests of the composites will be carried out before and after the long-term heat-treatment (~1200°C) in air.

4.2.3 YTTRIUM ALUMINATES

4.2.3.1 Effect of Yttria Doping on Creep of Alumina

Doping polycrystalline alumina with yttria has recently been reported by a group from Lehigh University, to have beneficial effects with regard to creep resistance,. This is particularly valuable since polycrystalline alumina fibers are most likely to be used for oxidation resistant ceramic composites and creep is the limiting factor. Studies were undertaken to verify this effect.

Alumina and yttria-doped alumina were processed in identical methods to obtain fully dense polycrystalline materials. Even with identical methods, the resulting materials were found to have differing grain sizes. The yttria-doping resulted in finer grain sizes. The creep behavior of the yttria-doped alumina was slightly inferior to that of undoped alumina; however when adjusted for the grain size effect, the yttria-doped alumina was superior (Fig. 4-1). However the beneficial effect was limited to lowering of creep rates by a factor of five times at the most, in contrast to an order of magnitude or more claimed by the Lehigh work. Grain size effects are thought to be responsible for the discrepancy.

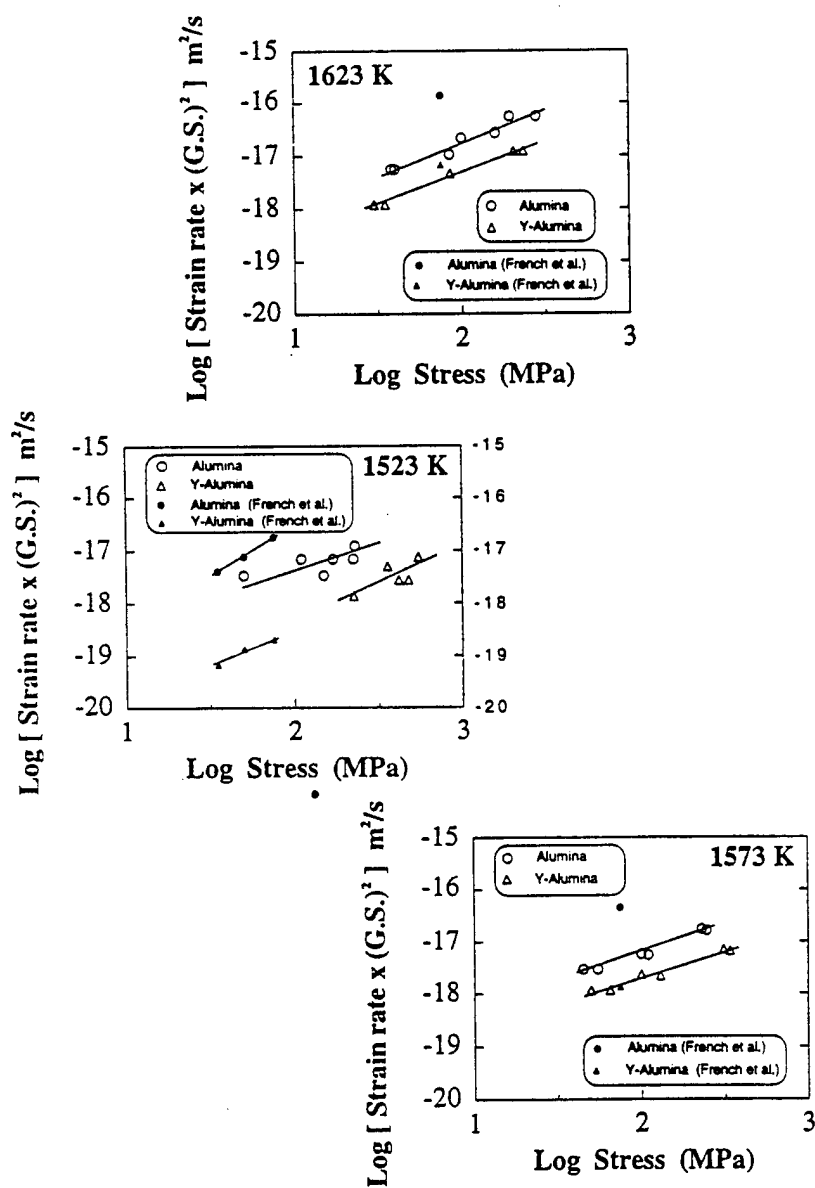


Figure 4-1. The Creep Data Obtained on Undoped and Ytria-Doped Alumina are Shown Compared After Normalizing the Data for Grain Size. The data of French et al. are also included.

4.3 PUBLICATIONS

1. T. A. Parthasarathy, C. A. Folsom, and L. P. Zawada, "Combined Effects of Exposure to Salt (NaCl) Water and Oxidation on The Strength of Uncoated and BN-Coated Nicalon Fibers," submitted, Amer. Ceram. Soc. (1996).
2. T. A. Parthasarathy and R. J. Kerans, "Predicted Effects of Interfacial Roughness on the Behavior of Selected Ceramic Composites," in press, Amer. Ceram. Soc. (1996)
3. T. A. Parthasarathy and R. S. Hay, "Effect of Yttria Concentration on the Low Strain Rate Flow Stress of Cubic Zirconia Single Crystals," *Acta Mater.*, **44**, 12 (1996).
4. E. Boakye, R. S. Hay, and M. D. Petry, "Sol- and Solution-Derived Lanthanum Phosphate Fiber Coatings" in preparation (1996).
5. M. D. Petry and T. Mah, "The Mean Tensile Strength and the Weibull Modulus of Ceramic Filaments: Comparison Based on Actual and Average Filament Diameters," submitted, Amer. Ceram. Soc. (1996).
6. M. D. Petry and T. Mah, "The Effect of Thermal Exposure on the Strength of Nextel™ 550 and 720 Filaments," submitted, Amer. Ceram. Soc. (1996).
7. T. Mah and T. A. Parthasarathy, "Effects of Temperature, Environment and Orientation on the Fracture Toughness of Single Crystal YAG," submitted, Amer. Ceram. Soc. (1996)
8. K. A. Keller, G. M. Mehrotra, and R. J. Kerans, "Freeze Forming of Alumina Monoliths," in TMS Proceedings, Processing and Fabrication of Advanced Materials V, Eds., T. S. Srivatsan and J. J. Moore, TMS, Warrendale, PA, 1996.
9. M. K. Cinibulk, "Sol-Gel Coating of Nicalon™ Fiber Cloths," *Ceram. Eng. Sci. Proc.*, **4**, 241-249 (1996).
10. M. K. Cinibulk, "Deposition of Oxide Coatings on Fiber Cloths by Electrostatic Attraction," *Amer. Ceram. Soc.*, **80**(2), 453-460 (1997).
11. M. K. Cinibulk and H.-J. Kleebe, "Grain-Boundary Films in a Silicon Nitride Ceramic at High Temperatures," in Ceramic Microstructures '96: Control at the Atomic Level, Eds., A. P. Tomsia and A. Glaeser, Plenum Press, in press.
12. M. K. Cinibulk, R. S. Hay, and R. E. Dutton, "Textured Calcium Hexaluminate Fiber-Matrix Interphase for Ceramic-Matrix Composites," in Ceramic Microstructures '96: Control at the Atomic Level, Eds., A. P. Tomsia and A. Glaeser, Plenum Press, in press (1996).

13. E. Boakye, R. S. Hay, and M. D. Petry, "Mixed Oxide Carbon Coatings from Aqueous Sols and Solutions," in press, MRS Symposium Proceedings (1996).
14. E. Boakye, M. D. Petry, and R. S. Hay, "Porous Aluminum Oxide and Lanthanum Phosphate Fiber Coatings" *Ceram Eng. Sci. Proc.*, 4, 53-60 (1996).
15. R. S. Hay, M. D. Petry, and E. Boakye, "Fiber Strength with Coatings from Sols and Solutions," *Ceram. Eng. Sci. Proc.*, 4, 43-52 (1996).
16. R. J. Kerans and T. A. Parthasarathy, "Debond Crack Roughness, Interface Properties and Fiber Coating Design in Ceramic Composites," Proceedings of the International Conference on Ceramic Composites, San Sebastian, Spain, 1996.
17. R. J. Kerans and T. A. Parthasarathy, "Fiber Coating Design Parameters for Ceramic Composites as Implied by Considerations of Debond Crack Roughness," Proceedings of the Conference on Ceramic Microstructures, Berkeley, CA, 1996.
18. T. A. Parthasarathy and D. M. Dimiduk, "Atomistic Simulation of the PPV Lock in L12 Alloys," *Acta Mater.*, 44(6), 2237-2247 (1996).
19. T. A. Parthasarathy, R. S. Hay, and R. Ruh, "High Temperature Deformation Behavior of SiC-Whisker Reinforced MgO-PSZ/Mullite Composites," *Amer. Ceram. Soc.*, 79(2), 475-83 (1996).
20. M. K. Cinibulk and R. S. Hay, "Textured Magnetoplumbite Fiber-Matrix Interphase Derived from Sol-Gel Fiber Coatings," *Amer. Ceram. Soc.*, 79(5), 1233-1246 (1996).
21. M. K. Cinibulk, J. . Welch, and R. S. Hay, "Preparation of Thin Sections of Coated Fibers for Characterization by Transmission Electron Microscopy," *Amer. Ceram. Soc.*, 79(9), 2481-2484 (1996).
22. M. K. Cinibulk, "Microstructure and Mechanical Behavior of an Hibonite Interphase in Alumina-Based Composites," *Ceram. Eng. Sci. Proc.*, 16(5), 633-41 (1995).
23. R. S. Hay, M. D. Petry, K. A. Keller, M. K. Cinibulk, and J. R. Welch, "Carbon and Oxide Coatings on Continuous Ceramic Fibers," MRS Symposium Proceedings, 365, 377-382 (1995).
24. K. A. Keller, "Freeze Forming of Alumina Monoliths," M.S. Thesis, Wright State University, Dayton, OH, 1995.

25. R. S. Hay, M. D. Petry, K. A. Keller, M. K. Cinibulk, and J. R. Welch, "Carbon and Oxide Coatings on Continuous Ceramic Fibers Ceramic Matrix Composites-Advanced High-Temperature Structural Materials," MRS Symposium Proceedings, 365, Eds., R. A. Lowder, M. K. Ferber, J. R. Hellmann, K. K. Chawla, and S. G. DiPietro, 377-382, (1995).
26. T. A. Parthasarathy, T. Mah, A. P. Katz, and C. A. Folsom, "Microstructural Stability of Nicalon Fibers at 1000°C in Air After Salt (NaCl) Exposure," Amer. Ceram. Soc., 78(7), 1992-96 (1995).
27. A. J. Eckel, J. D. Cawley, and T. A. Parthasarathy, "Oxidation Kinetics of a Continuous Carbon Phase in a Non-Reactive Matrix," Amer. Ceram. Soc., 78(4), 972-980 (1995).
28. P. R. Subramanian, T. A. Parthasarathy, M. G. Mendiratta, and D. M. Dimiduk, "Compressive Creep Behavior of Nb₅Si₃," Scripta Metall. et Mater., 32(8), 1227-1232 (1995).
29. D. M. Dimiduk and T. A. Parthasarathy, "Implications From Prestraining Experiments On Emerging Superkink Models For Anomalous Flow in L12 Alloys," Phil. Mag. Letts., 71(1), 21-31 (1995).
30. R. S. Hay, T. Mah, and C. Cooke, "Molybdenum-Palladium Fiber-Matrix Interlayers for Ceramic Composites," Ceram. Eng. Sci. Proc., 15(5) 760-768 (1994).
31. T. Mah, E. E. Hermes, and K. S. Mazdiasni, "Multicomponent Ceramic Powders," in Chemical Processing of Ceramics, Eds., B. I. Lee and E. J. A. Pope, pp. 75-103, Marcel Dekker, Inc., New York, NY (1994).
32. R. S. Hay, T. A. Parthasarathy, and J. R. Welch, "Creep and Stability of Pollucite," in Advanced Ceramics, Low-Expansion Materials, Amer. Ceram. Soc., 89-103 (1994).
33. J. D. Cawley, A. J. Eckel, T. A. Parthasarathy, "Oxidation of Carbon in Fiber-Reinforced Ceramic Matrix Composites," Ceram. Eng. Sci. Proc., 15(5), 967-976 (1994).
34. T. A. Parthasarathy, D. B. Marshall, R. J. Kerans, "Analysis of the Effect of Interfacial Roughness on Fiber Debonding and Sliding in Brittle Matrix Composites," Acta Metall. et Mater., 42(11), 3773-3784 (1994).
35. R. J. Kerans, P. D. Jero, and T. A. Parthasarathy, "Issues in the Control of Fiber/Matrix Interfaces in Ceramic Composites," Comp. Sci. Tech., 51, 291-296 (1994).

36. T. A. Parthasarathy, D. Barlage, P. D. Jero, and R. J. Kerans, "Effects of Interfacial Roughness Parameters on Fiber Push-Out Behavior of a Model Composite," Amer. Ceram. Soc., 77(12), 3232-3236 (1994).
37. P. D. Jero, T. A. Parthasarathy, and R. J. Kerans, "Interface Evaluation in Ceramic Composites," NATO Workshop on Integrated Airframe Design Technology, April 21-22, 1993, Turkey - AGARD Report 795: Introduction of Ceramics into Aerospace Structural Composites.
38. E. H. Moore, T. Mah, and K. Keller, "3-D Composite Fabrication through Matrix Slurry Pressure Infiltration," Ceram. Eng. Sci. Proc., 15(4), 113-120 (1994).
39. P. N. Kumta, T. Mah, P. D. Jero, and R. J. Kerans, "Processing of 3-D Interconnected Porous Aluminum Nitride Composites for Electronic Packaging," Mater. Letts., 21, 329 (1994).
40. R. J. Kerans, T. A. Parthasarathy, P. D. Jero, A. Chatterjee, and N. J. Pagano, "Fracture and Sliding in the Fiber/Matrix Interface and Failure Processes in Ceramic Composites," Br. Ceram. Trans., 92(5), 181-196 (1993).
41. P. D. Jero, T. A. Parthasarathy, and R. J. Kerans, "Interface Properties and their Measurement with Fiber Push-out Tests," in High Temperature Ceramic Matrix Composites, Eds., R. Naslain, J. Lamon, and D. Doumeingts, Woodhead Publishers, Ltd., Cambridge, England, pp. 401-412 (1993).
42. T. Mah and T. A. Parthasarathy, "Fracture Toughness of Single Crystal YAG," Scripta Metall. et Mater., 28, 1383-1385 (1993).
43. P. D. Jero, T. A. Parthasarathy, and R. J. Kerans, "A Comparison of Single and Multi-Fiber Push-out Techniques," Ceram. Eng. Sci. Proc., 14(7-8), 147-155 (1993).
44. T. Mah, T. A. Parthasarathy, D. Petry, and L. E. Matson, "Processing, Structure and Properties of Alumina-YAG Eutectic Fibers," Ceram. Eng. Sci. Proc., 14(7-8), 622-638 (1993).
45. T. Mah, P. R. Subramanian, and L. E. Matson, "Solid State Reactions Between Selected Intermetallics and Oxides in the Al-Y-O System," Scripta Metall. et Mater., 28, 961-963 (1993).
46. T. Mah, K. A. Keller, S. Sambassivan, and R. J. Kerans, "High-Temperature Environmental Stability of the Compounds in the Al₂O₃-Y₂O₃ System," Amer. Ceram Soc., in press.

47. K. Keller, T. Mah, T. A. Parthasarathy, and C. Cooke, "Fugitive Interfacial Carbon Coatings for Oxide/Oxide Composites," *Ceram. Eng. Sci. Proc.*, 14(7-8), 878-879 (1993).
48. S. Sambasivan, T. A. Parthasarathy, F. J. Scheltens, and R. J. Kerans, "Tailoring of Interfacial Properties in Ceramic Matrix Composites Using Segregants," *Ceram. Sci. Eng. Sci. Proc.*, 14(7-8), 873-877 (1993).
49. T. A. Parthasarathy, S. Rao, and D. M. Dimiduk, "Molecular Statics Simulations of Cores and Motion of Dislocations in NiAl," *Phil. Mag. A*, 67(3), 643-662 (1993).
50. R. J. Kerans, P. D. Jero, T. A. Parthasarathy, and A. Chatterjee, "Fracture and Sliding In the Fiber-Matrix Interface in Ceramic Composites," 6th Japan-US Conference on Composite Materials, Technomic Publishing Co., Lancaster, PA.
51. T. A. Parthasarathy, T. Mah, and L. E. Matson, "Deformation Behavior of an $\text{Al}_2\text{O}_3\text{-Y}_3\text{Al}_5\text{O}_{12}$ Eutectic Composite in Comparison with Sapphire and YAG," *Amer. Ceram. Soc.*, 76(1), 29-32 (1993).
52. K. A. Keller, T. Mah, T. A. Parthasarathy, and C. Cooke, "Fugitive Interfacial Carbon Coatings for Oxide/Oxide Composites" (Extended Abstract), *Ceram. Eng. Sci. Proc.*, 14(9-10), 878-879 (1993).
53. T. A. Parthasarathy, D. M. Dimiduk, and G. Saada, "Molecular Statics Simulations of Single Kinks in NiAl," *MRS Symposium Proceedings, in High Temperature Ordered Intermetallic Alloys V*, 288, pp. 311-316 (1992).
54. J. Wolfenstine and T. A. Parthasarathy, "Elevated Temperature Deformation of a Fine-grained $\text{Y}_3\text{Al}_5\text{O}_{12}\text{-YAlO}_3$ (20 vol.%) Material," *Scripta Metall. et Mater.*, 26, 1649-1653 (1992).
55. P. D. Jero, T. A. Parthasarathy, and R. J. Kerans, "Interfacial Roughness in Ceramic Matrix Composites," *Ceram. Eng. Sci. Proc.*, 13(7,8), 64-69 (1992).
56. P. D. Jero, T. A. Parthasarathy, and R. J. Kerans, "Measurement of Interface Properties from Push-out Tests," *Ceram. Eng. Sci. Proc.*, 13(7,8), 54-63 (1992).
57. T. A. Parthasarathy, T. Mah, and K. Keller, "Creep Mechanism of Polycrystalline Yttrium Aluminum Garnet," *Amer. Ceram. Soc.*, 75(7), 1756-1759 (1992).
58. T. Mah and M. D. Petry, "Eutectic Composition in the Pseudobinary of $\text{Y}_4\text{Al}_2\text{O}_9$ and Y_2O_3 ," *Amer. Ceram. Soc.*, 75(7), 2006-2009 (1992).

59. D. M. Dimiduk, S. Rao, T. A. Parthasarathy, and C. Woodward, "Solute- Dislocation Interactions and Solid Solution Strengthening Mechanisms," in Ordered Alloys, in Ordered Intermetallics-Physical Metallurgy and Mechanical Behavior, Eds., C. T. Liu et al, 237-256 (1992).

4.4 PATENT

1. M. K. Cinibulk and R. S. Hay, "Tubular Polycrystalline or Single-Crystal Inclusions in Single-Crystal Alumina," Air Force Invention AFD 00081. U.S. Patent application in progress.

4.5 DISCLOSURE AND RECORD OF INVENTION

1. E. Boakye, M. D. Petry, and R. S. Hay, "Lanthanum Phosphate (Monazite) Fiber Coatings and Thin Films from $\text{La}(\text{NO}_3)_3:(\text{NH}_4)_2\text{HPO}_4$ Derived Aqueous Particulate Sols" March 1996.

SECTION 5.0

TASK V. SUPPORT AND MAINTENANCE

The following are the major equipment and facilities within the Materials Directorate (WL/MLLM) which have been maintained, serviced and upgraded by the pool of UES core technicians: heat-treatment laboratory facilities, room and high temperature universal test machines (MTS, Instron, etc.), creep testing machines, hot-presses, XRD, machine shop equipment, HIP, ACP fiber-puller, Crystallox, UHV PVD, etc.

Throughout the period of the contract program, the core technicians were cross-trained on certain equipment to provide back-up operation for the laboratory. On various occasions, some core technicians attended training classes offered by the manufacturer.

New equipment was purchased through the Air Force and many of the existing apparatuses were upgraded with state-of-the-art measurement and sensing devices. Most of the testing apparatus are currently computer controlled and many of the processing equipment were automated or in the process of automation (e.g., hot-press).

Throughout the contract program, the UES core technicians worked toward maintaining and upgrading the Materials Directorate (WL/MLLM) laboratory facilities to the world-class level, and also supported engineers and scientists in performing their research projects.